# UNDERSTANDING AND PREDICTING CANCER CELL AGGRESSIVENESS FROM THEIR MIGRATORY PHENOTYPES

By

Bin Sheng Wong

A dissertation submitted to the Johns Hopkins University in conformity with the requirements for the degree of Doctor of Philosophy

Baltimore, Maryland

April 2019

# Abstract

Cell migration is an integral process for diverse physiological and pathological processes, including embryonic and tissue development, wound healing, immune response, chronic inflammation and cancer metastasis. Cancer metastasis, a coordinated and complex multistep process by which tumor cells disseminate from primary tumors to secondary sites, is responsible for up to 90% of all cancer-related death. During metastasis, tumor cells must interact, migrate and navigate through considerably different microenvironments including tissues at the local and distal sites, as well as within the circulatory system. As such, enhanced cell motility has been widely associated with increased cancer aggressiveness and metastatic potential, and overall poor patient outcome. A thorough understanding of the biochemical and physicomechanical driving forces underlying cell motility can therefore provide critical insights for the development of novel and effective diagnostic, preventative, therapeutic and prognostic strategies against cancer.

We start by first examining the role of podocalyxin on the migratory behavior of pancreatic cancer cells. The sialoglycoprotein podocalyxin is absent in normal pancreas but is overexpressed in pancreatic cancer and is associated with poor clinical outcome. Here we investigate the role of podocalyxin in migration and metastasis of pancreatic adenocarcinomas using SW1990 and Pa03c as cell models. Although ezrin is regarded as a cytoplasmic binding partner of podocalyxin that regulates actin polymerization via Rac1 or RhoA, we did not detect podocalyxin-ezrin association in pancreatic cancer cells. Moreover, depletion of podocalyxin did not alter actin dynamics or modulate Rac1 and RhoA activity in pancreatic cancer cells. Using mass spectrometry, bioinformatics analysis, co-immunoprecipitation, and pulldown assays, we discovered a novel, direct binding interaction between the cytoplasmic tail of podocalyxin and

the large GTPase dynamin-2 at its GTPase, middle, and pleckstrin homology domains. This podocalyxin-dynamin-2 interaction regulated microtubule growth rate, which in turn modulated focal adhesion dynamics and ultimately promoted efficient pancreatic cancer cell migration via microtubule- and Src-dependent pathways. Depletion of podocalyxin in a hemispleen mouse model of pancreatic cancer diminished liver metastasis without altering primary tumor size.

We next apply our knowledge of cell migration to develop a device for glioblastoma prognosis. Glioblastoma is the most aggressive form of brain cancer, characterized by high recurrence and dismal prognosis. Presently, there is no effective *in vitro* platform that can rapidly measure complex cellular phenotypic traits and accurately predict patient-specific clinical outcomes. Here, we employed a proprietary *in vitro* testing platform, Microfluidic Invasion Network Device (MIND), and screened a panel of 22 patient-derived primary glioblastoma specimens in a blind manner. We evaluated the ability of glioblastoma cells to navigate and squeeze through confined microenvironments that mimic *in vivo* tight perivascular conduits and white matter tracts in the brain parenchyma, as well as the proliferative capacity of highly motile subpopulations. By combining migratory- and proliferative-based indices, MIND predicts progression-free survival ($p=0.008$) and time to recurrence ($p=0.006$) retrospectively with high sensitivity (85%), specificity (89%), and accuracy (86%). In a pilot prospective study, MIND classified all patients accurately based on their survival outcomes.

Overall, this dissertation illustrates the importance of studying cell migration, both at the basic science as well as the translational levels, to better understand the mechanisms of cancer aggressiveness and develop potentially useful clinical applications.

## Thesis Committee

Professor Konstantinos Konstantopoulos (Advisor)

Department of Chemical and Biomolecular Engineering

Professor Denis Wirtz

Department of Chemical and Biomolecular Engineering

Associate Professor Stavroula Sofou

Department of Chemical and Biomolecular Engineering

Associate Professor Lei Zheng (Chair)

Department of Oncology

Assistant Professor Luo Gu

Department of Materials Science and Engineering

## Acknowledgements

First and foremost, I would like to express my deepest gratitude to my Ph.D. advisor Dr. Konstantinos Konstantopoulos for his leadership, mentorship and guidance. It has been an honor working in his laboratory and learning what it takes to become a great scientist. Throughout my time here, he has created and maintained a conducive, collaborative and financially supportive work environment for me to explore interesting scientific questions and acquired various important skills, both scientifically and professionally, that are crucial for my future career. More importantly, I am continuously inspired by his unwavering integrity and passion for science, which has been a major driving force that has kept me motivated and not discouraged when experiments were not working out as expected.

Next, I would like to thank all the members, both past and present, of the Konstantopoulos laboratory, whom I have had the pleasure to work with on a daily basis: Dr. Kimberly Stroka, Dr. Zhizhan Gu, Dr. Wei-Chien Hung, Dr. Colin Paul, Dr. Daniel Shea, Dr. Panagiotis Mistriotis, Dr. Alexandros Afthinos, Dr. Christopher Yankaskas, Emily Wisniewski, Robert Law, Runchen Zhao, Soontorn Tuntithavornwat, Yuqi Zhang, Kaustav Bera, Se Jong Lee, Christina Hum, Avery Tran, Elizabeth Orth, Tian Zhu, Nianchao Wang, Pranav Mehta, Siqi Cui, Yao Wang. In addition, I would also like to thank the undergraduate and high school students whom I have had the opportunity to mentor over the years, and have assisted me in various ways: Alec Greenberg, Yuan Hao Wong, Jake Bieber, Deborah Chin and Amber Fang.

Among my colleagues, I would like to extend my gratitude specifically to Panos who has introduced and taught me, as well as the entire lab, many important molecular biology techniques

that have entirely transformed how the Konstantopoulos lab approaches complex cell biology problems. His positive energy and enthusiasm for science are always infectious and stimulating. A special thank you to Dan whom I have worked with closely on all the pancreatic cancer related projects. Your efficient and meticulous work ethic has helped pushed our projects forward significantly. I would also like to acknowledge Chris, for not only being a responsible laboratory captain whom I can always rely on and go to if there is anything wrong with the laboratory, but also for his insightful contribution to the glioblastoma prognosis project. Lastly, I would like to thank Soontorn for being such a loyal friend whom has not only been tremendously helpful especially for the *in vivo* mice work, but also someone whom I look forward to having lunch everyday and confide in with my deepest personable troubles (as well as appointments, don't worry he will understand what I meant by appointments if he reads this).

While the members of the Konstantopoulos lab are all amazing and talented individuals, I will not be able to complete my projects without the constant and enormous support from my collaborators. Thank you to Dr. Lei Zheng for his expertise in pancreatic cancer mice models and for training me to perform sophisticated mice surgeries. Thank you to Dr. Joy Yang who has guided me on the molecular cloning of recombinant podocalyxin probes. Thank you to Dr. Alfredo Quiñones-Hinojosa and Dr. Sagar Shah for providing valuable primary glioblastoma patient samples and the analysis of clinical outcomes of these patients.

Outside of work and laboratory, I am lucky to have met many wonderful friends who have immensely enriched my life. I would like to first thank David Raciti for being my first roommate and the first friend I made in the United States. Though only a month older than me, David has

always been like a big brother to me, teaching me many important life skills including riding a bicycle, swimming and driving a car. His dedication to his research and work has also been an inspiration to me. Next, I would like to express my deepest appreciation for Nash Rochman and Scott Albert, whom I have lived with for the past 4-5 years. They have not only been excellent roommates but also my best friends and family here. Over the years, we have shared many memorable *(meˈm(ə)rəb(ə)l)* moments together, including the road trip down to South Carolina, weekly dinner at the Dizz, yearly corn maze and various musical adventures. They are always there for me when I need help or just someone to talk to, and I truly treasure the close friendships that we have built together. Last but certainly not least, I have to thank Mathew Kempske for everything that he has done for me. I will not be the man I am today without him. He is the impetus that made me more open and accepting of myself and my sexuality, which had been a silent battle and constant struggle for years before our encounter. I am also a more caring and better individual because of him. Thank you for tolerating my quirks, occasional nonsense and fervent love of musicals. I really cherish all the good (as well as sometimes the not so good) times that we have had together.

Finally, I will not be here today without the loving support from my family. None of this will be possible without them. Specifically to my parents, Foo Meng Wong and Ie Ling Teo, who have sacrificed so hard and worked tirelessly their entire life to ensure that I have a good education. Thank you also to my younger sisters Yi Wen and Yi Hui Wong for being there to take care of mum and dad while I am far away from home. Lastly to Yi Ting Wong, my second younger sister whom I unfortunately did not have the chance to say goodbye, I just want to tell you that Ah Ya loves you and hopes that you are as free as a bird, whenever you are, wherever you are.

# Table of Content

# List of Tables

# List of Figures

# Chapter 1 - Introduction

## 1.1 Cancer

Cancer refers to a group of diseases in which normal cells acquire the ability to proliferate uncontrollably and develop the capacity to locally invade nearby healthy tissues and spread systemically to distant body parts (1). Despite the tremendous efforts that have been devoted to the research and management of cancer over the past several decades, cancer still remains a major and global public health issue. In fact, with a projection of 1,735,350 new cancer diagnoses (equivalent to more than 4,700 new diagnoses per day) and 609,640 cancer-related deaths (equivalent to about 1,700 deaths per day) in 2018, cancer is the second leading cause of death in the United States, trailing only behind cardiovascular disease (2). While the incidence and death rate of cancer in general have both declined steadily over the years as a result of improved cancer prevention, screening, detection and management, these improvements are mostly restricted to the more commonly observed cancers affecting the prostate (specifically in men), breast (specifically in women), lung and colorectum (2). This is in stark contract to some of the other less common but yet aggressive cancer types, such as pancreatic and brain cancers, which continue to suffer from increasing mortality and poor patient outcome (2). There is therefore a dire need to better understand the pathology and progression of these highly lethal cancers in order to devise more specific and effective preventative, diagnostic, therapeutic and prognostic strategies.

### 1.1.1 Pancreatic cancer

Pancreatic cancer is an extremely lethal malignancy, with mortality almost paralleling its incidence (3). In 2018, the number of new cases and deaths of pancreatic cancer are projected to be 55,440 and 44,330 respectively in the United States, and 458,918 and 432,242 respectively worldwide (2,4). Despite a continuous 26% decline in death rate of all cancer types combined from 1991 to 2015, pancreatic cancer still remains as the most deadly cancer with a tremendously low 5-year relative survival rate of only 8% for all stages combined, making it the 4$^{th}$ leading cause of cancer-related death in both men and women (2). The mortality of pancreatic cancer in men has also risen by 0.3% per year during 2011 through 2015 (2). In fact, pancreatic cancer is predicted to become the 2$^{nd}$ leading cause of cancer-related death by 2030 if there is no further improvement to its clinical management and outcome (5).

The main reason for the poor prognosis of pancreatic cancer is delayed diagnosis due to lack of specific and noticeable symptoms during the early stages of the disease (6). In addition, prevention or early diagnosis is difficult because there are no reliable, specific and sensitive biomarkers, and effective imaging modalities for early staged pancreatic cancer (7). The overall low lifetime risk of developing pancreatic cancer (about 1.3% before age 70) also precludes widespread implementation of population-based screening of unselected population (6,8). As such, most patients remain asymptotic until they are diagnosed at an advanced stage where distant metastases, typically to the liver and peritoneum, have already developed (2,6). Although surgical resection is the only curative treatment option that has proven to prolong pancreatic cancer patient survival, only less than 20% of patients are eligible for surgical resection at the time of diagnosis due to vascular involvement and/or widespread metastasis (6). Even for these

small subpopulations of patients with surgically resectable disease, approximately 80% relapse after curative resection and adjuvant therapy, eventually dying from the disease with a 5-year survival rate of just 25% (3,6). For patient diagnosed with locally advanced or metastatic disease ineligible for surgery, the 5-year survival rate dropped even further to only 3-10%, where the average life expectancies after diagnosis are merely 6-9 months and 3 months for locally advanced and metastatic disease respectively (4).

Pancreatic ductal adenocarcinoma is the most common type of pancreatic malignancy and originates from incipient premalignant lesion in the pancreas known as pancreatic intraepithelial neoplasia after successful accumulation of multiple mutations over time (3,9). Molecular profiling has identified four key driver genes that are widely associated with the pathogenesis and progression of pancreatic cancer. Specifically, more than 90% of pancreatic tumors exhibit activating oncogenic KRAS mutation, and about 50-90% of pancreatic cancers develop inactivating mutation of tumor suppressor genes including CDKN2A (encoding p16), TP53, SMAD4, through either genetic or epigenetic alterations (3,10,11). Located on chromosome 12, RAS is a small GTPases that relay growth factor receptor signaling (e.g. EGF) into enhanced cellular growth, differentiation and survival. Ras is point mutated to its oncogenic constitutively active GTP-bound form KRAS is more than 90% of pancreatic tumors and even the lowest grade of pancreatic intraepithelial neoplasia, suggesting that it is one of the earliest and most critical genetic alterations that initiate pancreatic cancer pathogenesis (12,13). The tumor suppressor gene CDKN2A, which encodes the cell cycle regulator p16, is inactivated in almost 90% of pancreatic carcinomas (12). TP53, a well-known tumor suppressor gene responsible for sensing cellular stress response and inducing DNA repair and apoptosis, is inactivated in 50-75% of

pancreatic ductal adenocarcinoma, leading to loss of proper cell cycle checkpoint function (12). Lastly, SMAD4 (also known as gene deleted in pancreatic carcinoma, locus 4 DPC4), which mediates downstream growth inhibitory signaling exerted by TGF-β, is frequently deleted and inactivated in 55% of pancreatic cancer. Coupled with aberrant and overactive signaling resulting from external growth factors (e.g. EGF, IGF1, FGF, HGF, TGF-β) and tyrosine kinase receptors (e.g. EGFR, Her2, Her3, IGF1R, FGFR, HGFR), all these cumulative mutational changes serve to activate and amplify a diverse array of intracellular signaling pathways (e.g. Ras/Raf/MEF/ERK, PI3K/Akt/mTOR, NF-κB, STAT3, Wnt, Hedgehog, Notch), ultimately increasing proliferation, enhancing migration, and promoting apoptosis resistance and survival of pancreatic cancer cells (14).

Currently, the only treatment option capable of significantly extending the survival of pancreatic cancer patients is surgical resection (3). However, as mentioned earlier, only about 20% of patients are diagnosed with surgically resectable disease (6). For the other 80%, chemotherapy aiming for symptomatic relief and, unfortunately in many instances, palliative care remains the only other viable option to improve the quality of life of patients afflicted with this deadly disease (15). Gemcitabine, a nucleotide analog, is routinely prescribed as the first line chemotherapeutic agent against pancreatic cancer (3,6). Other agents that have been investigated clinically thus far, either as monotherapy or in combination with gemcitabine, have failed to significantly improve patient survival or demonstrated greater activity over gemcitabine monotherapy (15). These include EGFR inhibitors (e.g. erlotinib, cetuximab) which are only minimally effective as they act mechanistically upstream of KRAS, which are typically overactive in most pancreatic cancer (16). Anti-angiogenic agents such as VEGF inhibitors (e.g.

bevacizumab, aflibercept) and multikinase inhibitors with anti-angiogenic activity (e.g. sunitinib, sorafenib, axitinib, semaxanib) have also proven to be futile due to the inherent hypovascular stroma surrounding pancreatic cancer cells (10,16). Despite these challenges, many other targeted chemotherapeutics are still being actively investigated in the clinic. They include JAK/STAT inhibitors (e.g. ruxolitinib and momelotinib), BTK inhibitor (e.g. ibrutinib), IGF1R inhibitor (e.g. MM 141), CDK4/6 inhibitor (e,g, palbociclib) (6). Immunotherapy has also garnered increasing interest as a potential therapeutic option for pancreatic cancer. Blocking immune checkpoint and activating T cell function by inhibiting proteins involved in T cell checkpoints such as cytotoxic T-lymphocyte protein 4 with ipilimumab and programmed cell death protein with nivolumab and pembrolizumab have demonstrated promising results (16).

Overall, pancreatic cancer represents one of the, if not, deadliest cancer. The low survival and high mortality of pancreatic cancer stem from the inability for early detection, which often lead to advanced systemic metastatic disease that is difficult to eradicate. While there have been some significant progress in elucidating the molecular mechanism of the disease, there is still unfortunately a lack of specific and effective treatment options for pancreatic cancer once it reaches the metastatic state. As such, a continued and more in depth understanding of the underlying molecular pathology of pancreatic cancer holds the key to potentially identify novel molecular targets, which may subsequently aid in the development of diagnostic strategies to detect premalignant curable pancreatic lesion, and more effective targeted therapies.

### 1.1.2 Brain cancer

Malignant brain tumors represent one of the most lethal and feared cancer types, not only for their dismal prognosis, but also for their devastating effects on patient overall quality of life and cognitive function (17). In 2018, there are about 23,889 new cases and 16,830 deaths associated with cancers affecting the brain and nervous system in the United States (2). Globally, brain and nervous system cancers account for 296,851 new cases and 241,037 deaths in 2018 (4). The death rate of cancers of the brain and nervous system had been increasing in both men and women (18). While brain cancers are most prevalent in the elderly population, specifically in the sixth to eighth decades of life, they are extremely deadly in younger individuals. In fact, brain and other nervous system tumors are the top leading cause of cancer–related death in men before 40 and women before 20 years old (2).

Glioblastoma (GBM) is the most common form and highest grade (grade IV astrocytoma) of primary brain malignancy in adults (19). There are approximately 50,000 patients with GBMs with 10,000 new cases being diagnosed each year in the United States (20). With dismal 1- and 5-year survival rates of 35.7 and 4.7 % respectively, GBM is responsible for more than 13,000 deaths annually in the United States (21,22). The aggressiveness of GBMs primarily stem from their pronounced ability to proliferate and infiltrate. GBMs rapidly diffuse into surrounding brain parenchyma, and frequently spread to the contralateral hemisphere through the corpus callosum, thus confounding local therapy and rendering gross total resection nearly impossible (23-25). Interestingly, while GBM is highly invasive, the spread of GBM is mostly confined within the central nervous system and systemic metastasis is extremely rare (17). Nevertheless, even aggressive radical surgical resection coupled with concurrent chemo- and radiotherapy, GBM

remains incurable and frequently recur (26). The median patient survival of GBM is only 14.6 months with less than 5% of patients surviving past 5 years (19,25).

GBM either develops de novo (primary) or as a result of malignant progression from lower grade astrocytoma (secondary) (17). The cells isolated from a single primary GBM tumor are often pleomorphic (exhibiting varying size and morphology), along with extensive molecular and cellular heterogeneities (27,28). Despite the highly varied intra- and intertumoral molecular profiles of GBMs, molecular expression analyses have revealed three core signaling pathways that are repeatedly altered and implicated in GBMs. They are namely receptor tyrosine kinase/RAS/PI3K signaling which is altered in 88% of GBMs, TP53 signaling which is altered in 87% of GBMs, and RB signaling which is altered in 78% of GBMs (29). Based on a genome wide expression study with unsupervised hierarchical clustering, GBMs can be further classified into 4 different transcriptional subtypes based on their molecular neuropathology (30). The classical subtype exhibit the most common genetic aberrations of GBM and is characterized by EGFR amplification and/or activating point mutation to EGFRvIII, focal homozygous deletion of CDK2NA, chromosome 7 amplification paired with chromosome 10 deletion and the lack of TP53 mutation (30). The mesenchymal subtype is enriched for mutation/deletion of NF1, TP53 and CDKN2A, and expression of mesenchymal markers such as CHI3L1 and MET, and increased expression of genes involved in TNF and NF-κB pathways (30). The proneural subtype display frequent alteration of PDGFRA and point mutations in IDH1, loss of heterozygosity and inactivating mutation of TP53, shared gene expression features associated with oligodendrocytic developmental gene (e.g. PDGFRA, NKX2-2 and OLIC2) and proneural developmental gene (e.g.

SOX, DCX, DLL3, ASCL1, TCF4) (30). Lastly, the neural subtype is the least clearly defined and is typified by the expression of neuronal markers like NEFL, GABRA1, SYT1 and SLC12A5 (30).

Neurosurgery is typically indicated for cytoreduction to relieve mass effect, as well as to obtain biopsy tissue samples for histologic and molecular characterizations (17). Further eradication of tumor mass is achieved with intensity modulated radiotherapy and a DNA alkylating agent, temozolomide (17). Currently, the gold standard of care for GBM includes a triple combination of surgical resection, radiotherapy and adjuvant chemotherapy with temozolomide, but the overall survival of GBM remains unsatisfactory. The median survival of patients receiving such triple therapy is only between 15-18 months, with only less than 10% of patients going to survive past 5 years (25,31). Bevacizumab, an anti-angiogenic monoclonal antibody targeting VEGF, is an emerging drug option for recurrent GBM (32,33). While initial studies on the use of bevacizumab for recurrent GBM have demonstrated slight clinical improvement and longer time to progression, no overall survival benefits were observed (34). In fact the primary use of anti-angiogenic is mostly to increase vascular permeability for symptomatic relief of neurologic symptoms associated with brain edema (17). A biodegradable polymer with alkylating carmustin is also used for implantation into tumor bed after surgery with yet only modest survival benefits (35). Other physical and molecular-targeted therapies have been investigated but none have demonstrated significant improvement over conventional management strategies. These include tumor treatment fields with alternative electrical current (36), EGFR inhibitors (e.g. erlotinib, gefitinib) (37) and immunotherapy with checkpoint PD-1 inhibitor (e,g, nivolumab, pembrolizumab ipilimumab) (38) or chimeric antigen receptor T cell therapies (39).

While the prognosis for GBM is generally poor, there are still several patient specific factors that correlate with improved outcomes and better survival. The commonly used prognostic factors for long-term GBM survival include age at presentation, Karnofsky performance score, tumor size and location, tumor histology and aggressiveness of treatment modality, but they are often confounded by patient comorbidities, and thus rarely affect GBM treatment decisions (40). While increasing evidence that clinically relevant distinct molecular subtypes of GBM exist, these molecular subtypes also play limited roles in guiding clinical decisions. Aggressive therapy seems to be able to delay mortality in the classical and mesenchymal subtypes, while patients with the neural and proneural subtypes generally survive longer (41). Importantly, patients with the neural or proneural subtypes are also often associated with younger age, confounding the true utility of using molecular subtypes as independent prognostic marker for GBM survival (30).

Recent advances in proteomics and genomics have revealed novel molecular markers as independent predictors of GBM survival. One of the most notable molecular predictor of GBM is the methylation status of $O^6$-methylguanine-DNA methytransferase (MGMT) promoter, an enzyme responsible for DNA repair (42). MGMT promoter methylation is associated with longer survival and enhanced chemosensitivity to temozolamide, as reduction in DNA repair capacity arising from MGMT silencing generates more unrepaired DNA lesions that can subsequently induce more effective cytotoxic killing in response to temozolamide (43). Importantly the overall survival of patients with methylated MGMT promoter is almost doubled from 12.7 months to 21.7 months, along with a marked increase in 2-year survival rate from 14% to 46% (43). Despite being an independent and favorable predictive factor to temozolamide responsiveness and GBM survival, MGMT promoter methylation status has yet to attain broad clinical

applicability. This is primarily attributed to the lack of standardized and reliable methods to accurately classify a patient's MGMT methylation status, which in itself also suffer from significant intratumoral heterogeneity (44,45).

Another popular and emerging molecular predictor for GBM survival is the mutation status of isocitrate dehydrogenase (IDH) (46). IDH1 and IDH2 are enzymes that catalyze oxidative decarboxylation of isocitrate to alpha ketoglutarate, while in the process also reduce NADP+ to NADPH (47). The most common IDH mutation is a replacement of arginine with histidine residues at position 132 of IDH1 (R132H), which causes the enzyme to instead reduces alpha ketoglutarate to 2-hydroxyglutarate while converting NADPH to NADP+ (48). 2-hydroxyglutarate is an oncometabolite that may contribute to tumorigenesis (48). Decreased formation of alpha ketoglutarate also leads to increased level of HIF-1 alpha that can promote cell growth and angiogenesis (49). Mutation in IDH genes constitute one of the earliest and possibly also initiating mutational events in gliomas, as it is most commonly observed in lower grade II and III gliomas and secondary GBMs (80%) but rare in primary GBMs (5%) (46,50). Since secondary gliomas are more often observed in younger patients, IDH1 mutation, which happens to be more dominant and prevalent in progressive secondary gliomas, is therefore associated with better prognosis and longer survival (46,50). The prognostic value of IDH1 in primary GBM, however, remains to be elucidated.

Similar to pancreatic cancer, GBM is another form of highly aggressive and deadly cancer with dismal patient prognosis. While great strives have been taken to understand the molecular pathology of GBM, the inherently complex and intricate heterogeneities of GBM present

significant challenges for scientists and clinicians to fully grasp the mechanism underscoring the their aggressiveness and come up with effective therapeutic strategies. In view of the extremely short average lifespan of GBM patients and the rapid decline in their quality of life, there is therefore also a need to devise a better way to predict patient survival, and potentially also response to therapy, that can supplement currently available prognostic markers for the ultimate goal of personalized GBM care.

### 1.2 Cell migration and cancer metastasis

Cancer pathogenesis is a complicated and orchestrated multi-step process in which normal cells acquire multiple activating mutations that enable them to proliferate uncontrollably and invade surrounding tissues (1). In order for normal cells to transform into cancerous cells and form a primary tumor, they need to acquire certain key characteristics or hallmarks. These key characteristics include the ability to sustain proliferative signaling, evade growth suppressors, resist cell death, enable replicative immortality, induce angiogenesis, reprogram energy metabolism and evade immune destruction (1). Once a primary tumor is formed and successfully colonizes the initial site, the cancer cells will then start to detach from its original location, enter the circulatory system and migrate to distant organs to establish secondary colonies in a process known as metastasis (51).

Cancer metastasis is a highly coordinated process by which tumor cells disseminate from a primary tumor to secondary sites (51). Most of the cancer-related deaths are caused by metastasis. In fact, owing to the ability to effectively contain and eradicate primary tumors, the 5-year survival rates of most cancer types exceed 90% if the patients are diagnosed with

localized tumors (2). In contrast, the survival rates of patients suffering from distant metastatic diseases reduce considerably to less than 20% (2). The metastatic cascade is a multistep process, in which cancer cells have to first degrade surrounding extracellular matrixes, migrate away from the primary tumor, squeeze through and enter the circulatory system via intravasation, resist hydrodynamic shear stress, roll and arrest on endothelial wall before eventually extravasating and finally migrating into and colonizing a distal organ to eventually form a secondary tumor (52). Throughout this process, tumor cells must interact, migrate and navigate considerably different microenvironments including tissue at the primary and distal sites as well as within the circulatory system (6). Interestingly, there are some cancers such as GBMs that rarely metastasize out of the primary sites (i.e. central nervous system) (17). However these cancerous cells still exhibit enhanced mobility within the brain itself, and can invade locally and infiltrate across the corpus collosum to the other brain hemisphere (23-25). Cell migration is therefore pivotal not just for distant metastasis but also for local invasion, and is hence a crucial determinant for the aggressiveness of cancer and more importantly patient clinical outcome.

In this dissertation, we aim to understand and predict the aggressiveness of cancer cells by focusing on their ability to migrate and metastasize. We first start by providing a comprehensive review of the intricate, complex and plastic mechanisms in which cancer cells utilize to move in both unconfined and confined microenvironments that the cancer cells typically experience *in vivo* (**Chapter 2**). Next, by using pancreatic cancer as a case study, we characterize and delineate the role of an oncogenic membranous protein, podocalyxin, on the migratory behavior and metastatic potential of cancer cells (**Chapter 3**). We then attempt to make use of the knowledge we know about cell migration for useful clinical application. Specifically, we describe the

development of a novel microfluidic-based device, that can rapidly and unbiasedly assess the migratory and proliferative phenotypes of patient-derived GBM specimens, to be used as a prognostic tool for GBM patient survival (**Chapter 4**). Finally, we conclude by discussing potential future directions for each of the different projects centering on cell migration (**Chapter 5 and 6**). In sum, this dissertation reviews and illustrates how cell migration can be used to both understand the molecular basis underpinning cancer aggressiveness with basic science, as well as to predict relevant clinical outcomes in a translational manner.

# Chapter 2 - Exposing Cell-itary Confinement: Understanding The Mechanisms Of Confined Single Cell Migration

## 2.1 Abstract

Cells *in vivo* migrate in a complex microenvironment and are subjected to varying degrees of physical confinement provided by neighboring cells, tissues and extracellular matrix. The molecular machinery that cells utilize to migrate through confining pores or microtracks shares both similarities and differences with that used in unconfined 2D migration. Depending on the exact properties of the local microenvironment and cell contractile state, cells can adopt distinct phenotypes and employ a wide array of mechanisms to migrate efficiently in confined spaces. Remarkably, these various migration modes are also interconvertible and interconnected, highlighting the plasticity and inherent complexity underlying confined cell migration. In this chapter, an overview of the different molecular mechanisms utilized by cells to migrate in confinement is presented, with special emphasis on the extrinsic environmental and intrinsic molecular determinants that control the transformation from one mechanism to the other.

## 2.2 Introduction

Cell migration is an integral process for diverse normal physiological and homeostatic functions, including embryogenesis, tissue morphogenesis, wound healing and immune response, as well as pathological processes, such as chronic inflammatory diseases and cancer metastasis (53). There is thus a dire and important need to understand the biochemical and physicomechanical driving forces underlying cell motility, as it can provide critical insights to inform the development of novel and effective therapeutic strategies to ensure proper physiological cellular functions or

abate diseases. However, cell migration is an intricate and well-orchestrated biological phenomenon that is modulated by multiple intrinsic (i.e., cell type, actomyosin contractility, integrin-mediated adhesion, cellular and nuclear deformability etc.) and extrinsic factors (extracellular matrix (ECM) composition and stiffness, porosity, adhesiveness, elastic behavior etc.) (54,55). Much of what we currently know about the mechanisms of cell migration stems from *in vitro* experiments performed on 2D planar surfaces. Although 2D migration is relevant to certain physiological processes like wound healing and neutrophil trafficking on inflamed endothelium, 2D *in vitro* migration models fail to recapitulate the complex topographical cues presented by the tissue microenvironment that cells experience *in vivo (56)*.

Cells *in vivo* are typically embedded in and migrate within 3D dense fibrillar ECM with narrow pores. Many of times, the pores present in the ECM network are smaller than the average cell diameter, ranging from 1μm to 20μm (57). In such instances, cells have to either rely on matrix metalloproteinase (MMP)-dependent pericellular proteolysis to degrade surrounding ECM to generate tracks large enough for cells to migrate into (58), or MMP-independent alternative modes of migration where cells rearrange cytoskeleton and increase actomyosin contractility to facilitate cellular and nuclear deformation and translocation through tight pores (59-61). In addition to tracks generated *de novo* by migrating cells with MMP, there also exist pre-formed 3D longitudinal ECM-free channels that provide paths of least resistance in which cells can exploit to migrate efficiently. These *in vivo* 3D longitudinal channels can manifest themselves in many forms and are widely prevalent in the human body. Many of these 3D channels form between the connective tissue and the basement membrane of nerve, muscle and epithelium (54), and in fibrillar interstitial tissues between adjacent bundles of collagen fibers (62). Microtracks

are also present along and within blood (63,64) and lymphatic vessels (65), as well as in white matter tracks and perivascular spaces within the brain (66). Additionally, follower cancer cells can also migrate in 3D longitudinal tracks remodeled by leader fibroblasts or surrounding stromal cells (67,68). These 3D channels vary considerably in cross sectional area, ranging from 10 to 1000 $\mu m^2$ (57). As such, cells *in vivo* have to navigate through tight spaces, be it pores in ECM or tunnel-like tracks, and experience different degrees of physical confinement. Numerous recent studies have provided mounting evidence highlighting the differences between unconfined 2D migration and confined migration in terms of cellular morphology, intracellular signaling and molecular mechanisms (69). Indeed, many of the hallmarks of conventional 2D migration model are found to be dispensable in confined microenvironments, suggesting a specific and critical role that physical confinement plays in modulating cellular responses.

In this chapter, we focus on the behaviors and mechanisms by which single cells migrate in confinement. Specifically, confined single cell migration is defined as the phenomenon in which a single cell (not tethered or attached to neighboring cells) migrates in an environment where at least one of the three dimensions is about or below cell-size; in such a case, the cell has to form additional non-basal contact with the surrounding matrix and deform its cytoplasm and/or nucleus in order to move forward. Recent advances in bioengineering and microfabrication techniques have enabled us to engineer *in vitro* models to study confined single cell migration at precisely controlled experimental conditions mimicking aspects of the *in vivo* microenvironment. These models include polydimethylsiloxane (PDMS) microfluidic devices, microcontact printed patterns of prescribed geometries, micro/nanogrooves substrates, vertical confinement devices and 3D patterned hydrogels. A detailed description of the various techniques and systems to

simulate physiologically-relevant confined conditions can be found in a recent comprehensive review (70). Nevertheless, these experimental models are vital, as they have provided us with a rapid and high-throughput platform to study the mechanisms of confined single cell migration, which are discuss below.

### 2.3 Conventional paradigm of 2D cell motility cycle

Most of our existing understanding of cell migration originates from initial observations showing how metazoan cells adhere and crawl on 2D flat surfaces (71,72). Since then, a plethora of studies have been carried out to decipher the various steps involved in this highly orchestrated process termed as cell motility cycle. The detailed step-by-step mechanisms of 2D cell motility cycle have been extensively reviewed elsewhere (72-75), but they can be briefly summarized into four sequential steps, namely protrusion, adhesion, contraction and retraction. At first, a stationary cell receives motogenic signals, either biochemically with growth factors (76,77) or cytokines (78) or physicomechanically via physical confinement, differential substrate rigidity (79) or electrical current (80), and becomes polarized, developing distinct leading and trailing edges. This polarized cell state is achieved primarily by internal polarization of microtubule and secretory apparatus (81) that direct the vesicular transport of lipids (e.g. phosphatidylinositol (3,4,5)-trisphosphate, $PIP_3$) (82) and proteins (e.g. small Rho GTPases such as Rac1 and Cdc42 (83,84) to localize polarized signals. Accumulation of these polarized signals at the leading edge facilitates Arp2/3-dependent polymerization of branched actin filaments (F-actin), initiating the formation of wide, fan-like membrane protrusions known as lamellipodia (85). Adhesion molecules such as integrins present on the lamellipodial protrusions then bind to matrix ligand, forming new small nascent adhesions underneath the leading edge (86). RhoA and formin family

of actin nucleators such as mDia1 and mDia2 subsequently assemble actin stress fibers to connect with adhesions sites (87-89). Actomyosin contraction of the stress fibers pulls and exerts tension on nascent adhesions, enlarging and maturing them into focal adhesions (FAs) (90). At the same time, actomyosin contractility also enhances the contractile tension between the leading and trailing edge of the cell. The overall increase in cellular contractility, coupled with localized increase in myosin II activity towards the back of the cell, signals the disassembly of rear adhesions, releasing the rear of the cells from the 2D surfaces in a process known as trailing edge retraction, consequently leading to directed cell movement (91). As the cycle progresses, retrograde F-actin flow helps to push membrane and lipids rearward and position the nucleus towards the back of the cells, resetting the cell to respond to the next round of motogenic signal (92).

While it is widely believed that most epithelium-derived cells migrate in similar cyclic manner on 2D environments (53), the story becomes increasingly more complicated and less predictable as cells transition to the more physiologically relevant 3D environments where they are now confined within dense fibrillar matrix or preexisting migration tracks. Some of the hallmarks of the conventional 2D cell motility cycles, such as substrate adhesions and actomyosin contractility, are sometimes even dispensable in cells migrating in complex *in vivo* 3D environment. In fact, numerous studies conducted over the past decade have demonstrated that cells are extremely plastic and are able to adopt a multitude of different migration mechanisms in response to their surrounding environment to enable efficient locomotion. A schematic of the various confined cell migration mechanisms and their key characteristics can be found in **Figure 2.1**.

## 2.4 Pseudopodial-based mesenchymal confined migration

### 2.4.1 Comparison to 2D mesenchymal migration

In 3D artificial hydrogel networks *in vitro* and ECM tissues *in vivo*, cells can migrate with an elongated morphology with protrusions driven by actin polymerization, which we broadly term as pseudopodia and includes actin-rich structures such as lamellipodia, filopodia and invadopodia, similar to classical 2D mesenchymal migration (59,93,94). This mode of migration is also evident in pre-formed tunnel like conduit *in vivo,* in collagen/polyacrylamide-based patterned microtracks (79,95,96) and in PDMS microfluidic microchannel devices (97-99). Cells cultured on 1D lines created by microphotopatterning or microcontact printing, in which cells are laterally confined due to limitation of adhesion sites, also exhibit similar elongated morphology as they do on oriented 3D fibrillar ECM *in vivo*, where a strong correlation between migration speed and movement persistence is noted (94,100).

During confined 1D or 3D (1D/3D) mesenchymal migration, cells employ similar polarized signals of Rho-GTPases and $PIP_3$ to form actin-based pseudopodia protrusions at the leading edge like they do on 2D surfaces, form adhesions with the substrate via integrins and activate actomyosin contractility to subsequently detach cell rear (93,101). Though both 2D and 1D/3D confined mesenchymal migration appear to be rather analogous, there still exist some fundamental differences between the two in terms of cytoskeletal and adhesion dynamics, dependence on actomyosin contractility and force generation. First, 1D or 3D confinement induces drastic cytoskeletal remodeling accompanied by fewer F-actin stress fibers (97,102). In confined cells, actin is primarily localized at the cortex and/or concentrated on the leading edge

as actin-rich wedge-like slab (96,103). Second, the role of adhesion is reduced (but not necessarily eliminated) in confinement compared to 2D migration, with FAs demonstrating a smaller size and more diffuse cytoplasmic distribution rather than distinct locations around the cell periphery underneath the pseudopods on 2D surfaces (97,102). Third, while actomyosin contractility is indispensable for 2D migration, under specific conditions for example within rigid PDMS-based confined microchannels, cells are able to migrate efficiently even if actomyosin contractility is disrupted (97,104). However, the role of actomyosin contractility in confinement can also be cell-line dependent, and in certain instances are key for efficient confined migration (98,105). Fourth, the traction forces exerted by cells in confinement (either in microchannels or on 1D printed lines) are significantly lower than those on 2D flat surfaces, and are typically directed towards microchannel walls instead of to the center of the cell on 2D surfaces (102,106). In fact, phosphorylated myosin light chain (pMLC) dependent traction generation is not required for migration in microtracks (96). All these salient differences suggest that cells are able to modulate intracellular signaling, thereby optimizing their mobility in response to varying degree of confinement. In order to fully understand the mechanisms of confined mesenchymal migration, we have to dissect each of these factors individually and methodically.

### 2.4.2 Molecular determinants of confined mesenchymal migration

Pericellular proteolysis is essential for maintaining the mesenchymal phenotypes of tumor cells in 3D matrices. In 3D fibrillar collagen gels, HT1080 and MDA-MD-231 cells display a mesenchymal morphology during migration through proteolytically-generated tube-like tracks with β1 integrin co-clustering with MT1-MMP at interaction sites with collagen fibers; MT1-

MMP is a membrane-associated surface protease whose activity is needed for focalized ECM degradation (59). This mode of mesenchymal 3D migration can also be observed *in vivo* for HT1080 cells migrating in the mouse dermis as imaged with intravital multiphoton microscopy. Interestingly, inhibition of collagenolysis with MMP inhibitors converts mesenchymally migrating cells into a more spherical amoeboidal phenotype (discussed in section 4) that is phenotypically and mechanistically distinct from pseudopodial migration without negatively affecting migration speed. In the presence of pre-existing microtracks, either generated *in vitro* with laser ablation or micromolding in 3D hydrogel matrices or *in vivo* by surrounding or leader cancer-associated stromal cells, cells can still assume a mesenchymal migratory phenotype even when MMP functions are compromised or absent (95,96). ECM-free microtracks enable rapid and persistent migration of non-invasive MCF10a breast epithelial cells and MMP-depleted MDA-MD-231, which are unable to invade otherwise in 3D collagen matrices (95). Microtracks provide a clear unimpeded path of low resistance for migrating cells, reducing the requirement for cell-matrix mechanocoupling, traction force generation and matrix remodeling required for efficient migration, thereby lowering the mechanistic threshold for local tissue invasion.

Matrix adhesion is needed for pseudopodial migration on 2D but its role in confinement is markedly diminished. On 2D surfaces or in wide microchannels emulating a 2D microenvironment, FAs (as visualized with phospho-paxilin and phospho-FAK) are localized alongside at the periphery of pseudopod protrusions as distinct complexes. In contrast, FAs are significantly reduced in size in cells migrating inside narrow microchannels (<20μm), and display a uniform distribution along the cell's migratory axis (97). On 1D lines, similar long linear localization of adhesion components such as α5 integrin, β1 integrin, FAK, vinculin and

paxillin are also observed spanning the entire length of the cell axis (94). As a result of the diminished role of substrate adhesion in confinement, blocking β1 integrin has little or no appreciable effect on migration speed in narrow channels or cell-scale collagen microtracks despite completely abrogating planar 2D migration or reducing speed in 3D collagen matrices (96,97). 1D migration speed is also resistant to varying ECM ligand density, as migration speed exhibit a saturating relationship as ligand density increases rather than a classical biphasic phenomenon observed on 2D surfaces (94). It is however worth noting that while β1 integrin is not required for the maintenance of migration speed in microtracks, they are needed to promote the elongated morphology of the migrating cells. Instead of a stable elongated morphology with pseudopodial protrusion, β1-depleted cells undergo rapid dynamic oscillation between elongated (mesenchymal) and spherical (amoeboidal) morphologies (96).

The effect of actomyosin modulation on confined pseudopodial migration is more variable and dependent on the cell type and matrix dimensions. Inhibiting myosin II activity with blebbistatin impairs migration of fibroblasts and human epithelial keratinocytes on 1D lines and in 3D ECM (94). In 3D collagen gels, ROCK inhibition with Y27632 significantly diminishes human foreskin fibroblast lamellipodial-based migration, as for other epithelial cells (107). However, blebbistatin treatment on human foreskin fibroblasts migrating on top of 2D cell-derived matrix is unaffected, consistent with effect of blebbistatin on 2D fibroblast migration (108). On the other hand, confined migration of various cancer cells, such as MDA-MD-231 breast cancer cells and S180 murine sarcoma cells, is resistant to inhibition of actomyosin contractility. Whilst inhibiting the Rho/ROCK/myosin II signaling cascade with CT04/Y27632/blebbistatin-ML7 suppresses migration on 2D unconfined substrates, these pharmacological interventions have no

appreciable effect on confined cell migration through 3μm narrow microchannels (97,99). Along these lines, modulation of actomyosin contractility via the use of blebbistatin (inactivation) or calyculin A (activation) does not alter the traction forces exerted by NIH-3T3 or HOS human osteosarcoma migrating in narrow channels (106).

Microtubules play a key role in regulating the velocity, directionality and persistence of cell migration in confinement. On 1D microprinted lines, the centrosome (pericentrin) is located behind of nucleus (versus in front of nucleus on 2D) (94,109) while stabilized microtubules (i.e., detyrosinated glu tubulin) are localized as polarized parallel bundle arrays anterior to nucleus, extending into lamellipodia (94,96). Confinement induces alpha-tubulin localization and microtubule growth towards the leading edge, as opposed to the rather isotropic microtubule polymerization from microtubule-organizing center on 2D surfaces. Interfering with microtubule dynamics with either taxol (which prevents depolymerization) or colchicine (which promotes disassembly) significantly decreases cell velocity and directionality in 3μm narrow channels, indicating a critical role of microtubule in establishing migratory persistence in confinement (97). Similarly, inhibiting microtubule polymerization with nocodazole or microtubule depolymerization with taxol causes rounded cell morphology with uncontrolled protrusions in all directions, decreases motile fraction and reduces migration speed along 1D lines, microtracks and in 3D ECM, suggesting that MT is important in maintaining uniaxial morphology and alignment in 1D and 3D migration (94,96).

## 2.5 Bleb-based amoeboidal migration

### 2.5.1 General morphological and molecular features of amoeboidal migration

When actomyosin contractility is elevated and/or cellular adhesions are diminished, cells typically transform from an elongated, spindle-like mesenchymal morphology that is dependent on adhesion and actin-based pseudopodial protrusion into a rounded amoeboidal morphology resembling that of *Dictyostelium* amoeba and migrating leukocytes. This process is termed as mesenchyme-to-amoeboid transition (MAT), and has been observed both *in vitro* and *in vivo* in mouse xenograft models (61,110). Amoeboidal migration is associated with rounded cell morphology with spherical membrane protrusions that are devoid of filamentous actin known as blebs, limited and diffuse distribution of cellular adhesion (e.g. β1, paxillin) and higher actomyosin contractility (61). Moreover, amoeboid cells also exert lower traction forces and exhibit higher cortical tension than mesenchymally-migrating cells. Traction forces exerted by Walker 256 carcinosarcoma when they are undergoing non-adherent blebbing motion are several orders of magnitude lower than those exerted during integrin-based FA-dependent mesenchymal motility (111). Furthermore, the forces are directed outwards from the cell body to expand rather than contract the substrate in order to generate sufficient friction to drive migration. Lateral expansion of cells are also able to generate enough traction by extending inter-digitating with the surrounding discontinuous confined matrices to provide traction in the absence of adhesion (110).

Cell mechanics represents one of the key determinants of MAT. Whether or not a cell prefers to form blebs or lamellipodia depends on a delicate balance between actin protrusivity, as controlled primarily Rac1 and Arp2/3 complex, and cellular contractility, as dictated by the

RhoA/ROCK/myosin signaling axis. The transition between these two phenotypes can be achieved even locally at the cell leading edge without any global change in cell shapes, polarity and adhesion (111). Activating Rac1, which recruits and activates downstream Arp2/3 to facilitate nucleation of actin filaments, switches blebs to lamellipodia, increases cell cross-sectional area and decreases cortical tension. This lamellipodia-promoting role of Rac1 is intimately linked with Arp2/3 activity, whose inhibition via the pharmacological agent CK666 or via siRNA decreases lamellipodial formation in Walker 256 carcinosarcoma (111). Conversely, Rho/ROCK/myosin signaling promotes rounded bleb-associated mode of motility. Inhibiting actomyosin contractility with RhoA inhibitor C3 transferase, ROCK inhibitor Y27632 or myosin II inhibitor blebbistatin decreases bleb formation while promoting lamellipodia protrusion in Walker 256 Carcinosarcoma (111) as well as A375m2 melanoma and LS174T colon carcinoma cells (61). On the other hand, increasing cell contractility via the use of constitutively active ROCK or overexpression of Rho enhances cell blebbing.

Cells prefer to switch to an amoeboidal mode of migration when cell-ECM adhesion is diminished or eliminated. This can be achieved by either downregulating integrins or decreasing substrate adhesiveness (112,113). Typically, amoeboidal migration occurs without FAs, and can proceed efficiently even if components of the adhesion machinery such as integrin $\alpha_1\beta_2$ or talin are knocked down or adhesion is completely prevented in non-adhesive PDMS microchannels or in the presence of EDTA which chelates divalent ions needed to establish integrin binding (112,113). This is in stark contrast to elongated mesenchymal migration where motility ceases when adhesion is eliminated. The effect of migration phenotypes exerted by changing substrate adhesiveness is also rapid and reversible, as cells (suspension subline of Walker 256

carcinosarcoma) plated on micropatterned surface with alternating adhesive and non-adhesive areas form lamellipodia immediate upon contacting adhesive region which then quickly disappear and resumed blebbing when they move on to non-adhesive region (111). In HT1080, MAT is associated with decreased surface coverage of $\alpha_2\beta_1$ integrin heterodimers, diminished integrin-mediated adhesion and downstream signaling via p-FAK (113). Consequently, inhibition of calpain2 and Src kinase, which participate in FA turnover, suppressed mesenchymal invasion drastically but exerted little or no effect on amoeboid migration where the role of adhesion is already diminished. Interestingly, Rho/ROCK inhibition is able to restore integrin function and calpain2 sensitivity, and reverses MAT, indicating that Rho/ROCK signaling also contributes to integrin modulation in addition to enhancing actomyosin contractility to promote amoeboid migration.

Besides altering cellular contractility and adhesion, inhibiting matrix metalloproteinase (MMP) can also induce MAT. HT1080 and MDA-MB-231 transform from an elongated mesenchymal into a spherical amoeboidal morphology that still move at the same speed upon MMP inhibition *in vitro* in 3D collagen gels as well as *in vivo* (59). Similar phenotypic conversion is also observed for BE and WM266.4 melanoma cells during invasion through 3D matrigels (61). This protease-independent amoeboidal migration occurs without any matrix remodeling and generation of any migration tracks, suggesting that the cells have to now squeeze through the tight collagen fiber network in order to maintain efficient migration. Indeed, during MAT, the cells lose their β1 integrin clusters and surface localization of MT1-MMP, and develop diffuse cortical actin rims and narrow region of constriction rings to aid in deforming the cells through narrow pores.

It is noteworthy that MMP inhibition is certainly not a prerequisite for amoeboidal migration. To the contrary, a paradoxical elevated secretion of MMPs, specifically MMP9, was observed in melanoma cells that are already prone to migrate amoeboidally as compared to their elongated mesenchymal counterparts (114). MMP9 promotes amoeboidal migration through activating actomyosin contractility by binding to CD44 receptor in a non-catalytic, paracrine and autocrine manner. In turn, the increase in actomyosin contractility activates ROCK/JAK/STAT3 cascade, forming a positive feedback loop that upregulates MMP9 gene expression. Indeed, MMP9 expression was shown to increase over the course of melanoma progression and is highly enriched in invasive lesion front, which incidentally also display more rounded amoeboidal morphology positive for p-STAT3.

The roles of MMP on MAT are hence variable and cell-line dependent. Nevertheless, the ability for the tumor cells to sustain efficient 3D motility via a protease-independent mechanism and the non-catalytic role of MMPs in promoting amoeboidal migration could explain the many failures of MMP inhibitors in human clinical trials despite demonstrating promising potentials in halting migration *in vitro* and *in vivo* (115,116).

### 2.5.2 Bleb-based migration in physical confinement

Fascinatingly, physical confinement triggers MAT. Using a sandwich system consisting of two surfaces of tunable surface adhesion characteristics, normal human dermal fibroblasts have been shown to retract and adopt a more compact phenotype with fewer lamellipodia but more elongated pseudopodia when confined to a low ceiling of 3-5μm (117). Under high confinement

(i.e., 3μm) and low adhesion, most normal human dermal fibroblasts become immobile with very rounded morphology characterized by continuous uncoordinated blebbing activity. A portion of these confined cells, however, display a round cell body with small leading edge local protrusion and are able to move with an amoeboidal mode of migration, termed as A1 blebbing mode. This subpopulation of cells exhibiting the A1 blebbing mode migrates faster than the remaining spread cells that display a partial mesenchymal morphology when being vertically confined (117). Similarly, a suspension subline of Walker 256 carcinosarcoma that typically form non-adherent blebs migrate limitedly on 2D surface, but efficiently when being confined vertically between glass and agarose and within 3D gels with directional persistence (111,112). Confinement in this case is essential for cell motility as it enables force transmission in the absence or near absence of adhesions to substrate.

Indeed, computational modeling suggests that cell matrix adhesion is dispensable for cell migration in discontinuous confined environments where blebbing predominates (110). On an unconfined 2D surface, cells migrate with an elongated morphology with actin-driven protrusion, and highest velocity is predicted at intermediate cell-ECM adhesion. This biphasic migration speed behavior to substrate adhesiveness has been verified experimentally with multiple cell lines on 2D platforms (98). While on discontinuous confined environment, such as those represented by dense fiber mesh network, blebbing mode of migration mechanism dominates and maximum cell velocity scale inversely with adhesion. The modeling prediction is verified *in vitro* where $\beta_1$ integrin or talin depletion reduces migration on 2D surfaces but increases amoeboidal migration speed in confined environments.

Under high confinement and low adhesion, numerous cell types, including normal or transformed cells of either epithelial or mesenchymal origins, are able to adopt an additional mode of stable bleb-based migration, termed as A2 blebbing, characterized by an elongated ellipsoidal morphology with a large rear uropod and a smooth rounded leading edge, reminiscent of migrating neutrophils (117). Cells displaying the A2 blebbing morphology typically migrate faster than their A1 blebbing counterparts. The proportions of cells that display the A2 blebbing morphology for each cell type though vary considerably across the group depending on their basal cellular contractility. In general, cell lines that display higher intrinsic cortical contractility also have a higher proportion of cells that migrates via the A2 mode. Similar fast and directionally persistently A2 mode of bleb-based migration is also evident in zebrafish embryonic progenitor cells both *in vitro* under vertical confinement between two planar glass slides though these cells are immobile on 2D surfaces, and *in vivo* during early development, for instance at sites of local wounding site where there exist higher actomyosin contractility (118).

Mechanistically, A1 and A2 blebbing differ in their requirement for actomyosin contractility. Increasing contractility via calyculin A treatment or knocking down MYPT1, the PP1 partner targeting myosin II, results in an increased frequency of A2 blebbing cells. The converse is accordingly true upon cell treatment with the ROCK inhibitor Y27632 or myosin II inhibitor blebbistatin where more cells exhibit the A1 rather than A2 mode of migration (117). Additionally, treating zebrafish embryonic progenitor cells with serum or lysophosphatidic acid, a serum phospholipid capable of activating cortical contractility via the Rho/ROCK pathway, also transforms cells reversibly into the A2 stable bleb morphology, thereby providing further evidence that A2 blebbing depends on high myosin-based contractility (118).

The organization and role of actin are also different between the A1 and A2 blebbing migration modes although they both lack FAs and organized actin stress fibers. In A1 cells, fast retrograde flow of actin is localized at the small protruding leading edge. In A2 cells, however, actin and myosin II are absent from the cell front but instead concentrated around the cell cortex where the uropods are. Both actin and myosin II exhibit fast and global cortical retrograde flow around the central region of the A2 cells, with little to no flow towards the rear, suggesting that the uropod is a dragged passive body (117). Similar rearward gradient of contractility, cortical actomyosin enrichment and retrograde flow are also evident in non-adherent blebbing Walker 256 carcinosarcoma (112). Relaxing cortical contractility at the rear of the cells but not the front by cortex ablation decreases migration velocity. Via computational modeling, it was revealed that rearward contractility gradient is able to drive adhesion-independent amoeboidal migration via two complementary mechanisms. First, frictional forces from counteracting retrograde cortical flow generate propulsive force. Second, when the friction becomes sufficiently large enough to hold cell body in place, rearward contractility of myosin results in leading edge expansion, leading to net cell movement. Interestingly, the model predicts that cell migration velocity correlates not with amplitude of stress exerted by the cells but rather velocity of the actomyosin flow, highlighting the importance of cortical actomyosin flow in facilitating amoeboidal A2 migration. In summary, cells could fall into two different contractility regimes when they are undergoing MAT following vertical confinement. Under a high contractility regime, global cortical actin retrograde flow results in myosin-dependent mechanical instability of cortex, leading to formation of A2 stable blebs. When contractility is inhibited, the cortex become more stable, allowing for more protrusive activity, ultimately leading to an A1 blebbing phenotype.

### 2.5.3 Establishing polarity in blebbing cells

Amoeboid migration is responsive to chemotractant cues and is not a form of random motility (61). In mesenchymal cells, specific spatial localization of Rac1, Cdc42 and $PIP_3$ are needed to establish polarization and direction of migration, but such differential spatial enrichment is absent in amoeboid cells (93). So then how are amoeboidal cells able to achieve similar polarization? Localization of ezrin/moesin/radixin (ERM) protein family, which are linkers between the plasma membrane and actin cytoskeleton, appears to be involved in this process. Asymmetry contractility is positively related with asymmetry in cortex-membrane linkage (110). ROCK is able to phosphorylate ERM, and ezrin localization is also dependent on Rho activity. In fact, colocalization of contractile machinery (pMLC) and pERM promotes blebbing and favors migration in confinement (119). This is achieved by the STRIPAK components, MST3/4 kinases that locally coordinate phosphorylation of ERM and inhibit dephosphorylating of MLC, leading to increased phosphorylation and cortical colocalization of MLC and ERM, resulting in enhanced cortex-membrane linkage and more frequent membrane blebbing. Indeed, increasing actomyosin-membrane linkage with MST3/4 overexpression is associated with increased *In vivo* metastasis from mammary fat pad to lymph node. Colocalization of actomyosin contractile function and ERM proteins promotes more efficient pulling of contractile cytoskeleton on the plasma membrane, exerting more force on the plasma membrane instead of being coupled to integrins via FAs, thereby producing more blebbing.

A recent study on zebrafish embryonic progenitor cells, however, suggests that that polarization in A2 migrating cells is initiated by stochastic contractility that is driven by cortical network

instabilities and subsequently maintained by a positive cortical feedback loop (118). Specifically, addition of lysophosphatidic acid causes rapid redistribution of myosin II to the cell cortex, upregulating cortical contractility and increasing bleb expansion. Interestingly, similar increases in myosin II accumulation, bleb formation and cortical contractility are also observed in serum-free confined condition, indicating that confinement in itself is able to trigger an increase in cell contractility independent of external biochemical cues, possibly via a yet to be discovered mechanism involving cell and/or nuclear deformation. Nevertheless, these local fluctuations in cortical contractility at the cell periphery disrupt cell symmetry, leading to initial polarization. Polarization is then further enhanced and stabilized by a positive feedback between continuous cortical actin and myosin flow towards cell rear and formation of cortical contractility gradient that reinforces the flow, resulting in the formation and maintenance of stable blebs. Unlike conventional 2D migrating cells where polarization hinges on $PIP_3$ is impaired with PI3K inhibition, polarization in A2 blebbing mode is resistant to PI3K inhibition. Instead it is dependent on proper actin turnover as inhibition of actin turnover by latrunculin A or jasplakinolide resulted in disappearance of stable blebs (118).

### 2.5.4 Mechanotransduction pathway to optimize contractility in confinement

Cells are able to identify, integrate and respond to external environmental cues and physical stimuli in a process known as mechanotransduction. However, the exact mechanotransduction mechanisms by which cells sense physical confinement and translate this signal into elevated cortical contractility is still underexplored. Prior work suggested that the existence of an intricate cross talk between Rac1 and RhoA/myosin II signaling (98) that serves to optimize actomyosin contractility in order to facilitate efficient migration in confined microchannels. Specifically,

Rac1 activity is enhanced in cells migrating on 2D surfaces or inside wide microchannels (≥ 20μm) to facilitate the formation of lamellipodia protrusions. Conversely, RhoA/myosin II signaling is amplified when cells are migrating inside narrow microchannels (≤ 10μm), resulting in higher actomyosin contractility and a migration mode with amoeboidal characteristics (98). These distinct signaling strategies employed by cells in response to physical confinement are modulated by mechanosensors, which can be broadly classified into three major classes: stretch-activated ion channels (120), cytoskeletal and nuclear elements (121) and integrins (122).

We recently discovered that the membrane-bound stretch-activated cation channel PIEZO1 is responsible for the intracellular calcium increase observed as cells transition from an unconfined 2D environment into confined microchannels (105). In particular, elevated membrane tension induced by physical confinement activates PIEZO1, leading to increased intracellular calcium levels, which in turn mediate suppression of protein kinase A (PKA) via a phosphodiesterase type 1 (PDE-1) dependent pathway. Interestingly, confinement-induced inhibition of PKA activity is only negated when both PIEZO1 and myosin II are blocked (but not when either one is individually inhibited), implying that myosin II can also sense physical confinement and suppress PKA directly and independently of PIEZO1. Indeed, external physical forces have been reported to induce assembly of myosin II bipolar filaments and actomyosin bundles (123,124). Moreover, myosin II has also been implicated in sensing surface topographical cues in fibroblasts (125) and tumor cells (99). In relation to mechanosensing of physical confinement, it has been hypothesized that myosin II decreases PKA activity indirectly via downregulation of Rac1 activity, due to the negative crosstalk between Rac and Rho/myosin, that subsequently reduces recruitment of A-kinase anchoring proteins (AKAPs) to the cell leading edge that is

capable of activating PKA. Together, these two independent yet interconnected mechanosensing mechanisms serve to suppress PKA and amplify actomyosin contractility in confinement. Of note, components of adhesion complexes, such as α4 and α5 integrins, do not appear to be essential for cell to sense physical confinement. Rather, they primarily serve to amplify the differential response of contractility increase induced by confinement.

### 2.6 Lobopodial migration in linearly elastic matrices

Cells are able to sense the mechanical and rheological properties of extracellular matrices and adopt distinct migration mechanisms in different 3D microenvironments. While most migration studies using 3D matrices, such as polyacrylamide or collagen gels, have focused on the ability of the cells to respond to substrate stiffness and pore sizes, limited attention has been devoted to the elastic behavior of the matrix material like strain stiffening (101). Strain stiffening refers to the ability of a material to resist deformation and handle applied stress. In general, materials can be classified broadly as nonlinearly elastic where they undergo strain stiffening (i.e. the stiffness of the material increases with increasing force application), and linearly elastic where strain stiffening is not observed (i.e. the stiffness of the material is independent of the magnitude of force applied to it).

Fibroblasts are able to recognize the differences in the elastic behaviors of 3D matrices and migrate via two distinct mechanisms (101). In 3D collagen gels, which are non-linearly elastic and softer, fibroblasts migrate via the classical flat lamellipodial protrusions, similarly to how they would migrate on unconfined planar 2D surfaces. In highly cross-linked, stiffer and linearly elastic materials such as dermal tissue explant or cell-derived matrix (CDM), however,

fibroblasts switch to a diametrically opposed morphology, where blunt cylindrical protrusions termed as the lobopodia and small lateral blebs are observed (93). Notably, the lobopodial mode of migration only occurs when the cells are being confined within the 3D mesh-like structure of CDM but not on top of 2D CDM, indicating that lobopodia-based migration is a unique mechanism that cells can use inside linearly elastic matrices. Unlike lamellipodia where $PIP_3$, Rac1 and Cdc42 are polarized to the leading edge of the cells, lobopodia are devoid of these polarized signals as well as of other lamellipodial markers such as cortactin, VASP and F-actin. Instead, the lobopodial protrusions are mainly driven by high intracellular pressure that is highly dependent on RhoA/ROCK/myosin contractility. Fibroblasts continue to migrate using lobopodia after depletion of Rac1, Cdc42 or formin mDia1 with slight variation in velocity in certain instances. In contrast, inhibiting contractility by knocking down RhoA or inhibiting ROCK causes the fibroblasts to switch from a lobopodial to lamellipodial mode without affecting migration velocity. Interestingly, while myosin inhibition also results in the same lobopodial-to-lamellipodial transition, cell migration was significantly impaired, presumably due to inefficient nuclear migration.

Indeed, further studies revealed that the nucleus play a pivotal role in pressurizing the anterior cytoplasm at the cell leading edge by acting as a piston to generate lobopodia (126). There exists a high intracellular hydrostatic pressure differential between the front and back, as separated by the nucleus, of a lobopodially migrating cells in 3D linearly elastic matrices. The nucleus is being connected to the anterior cell membrane via a myosin II-vimentin-nesprin complex and is being pulled forward coordinately as cells traverse through the confined pores of linearly elastic matrices (127). Knocking down nesprin3 reverses the lobopodial phenotype back to

lamellipodia, equalizes intracellular pressure and reduces the velocity of migrating fibroblasts independent of affecting Rho-mediated contractility, indicating the importance structural role of nesprin3 as a nucleoskeleton-cytoskeleton linker in lobopodial-based migration. Unlike the critical role of microtubules in ensuring directionality and polarization of migrating cells displaying a lamellipodial morphology, microtubules do not seem to be involved in promoting the coordinated nucleus movement observed in lobopodial cells. The effect of microtubule inhibition on the velocity and persistence of lobopodial cells, however, remains to be further investigated. Despite the differences in morphology, polarized signals and motility mechanism, lamellipodia- and lobopodia-based migration do share a similar requirement for adhesions. Both types of protrusion possess paxillin and vinculin-based FAs. Blocking integrins also significantly impairs lobopodial migration speed and directionality in fibroblasts.

The discovery of this non-polarized, contractility-dependent and intracellular pressure-driven lobopodial-based migration in normal fibroblasts naturally begs the question: can other cell types such as cancer cells also use a lobopodia-based mode of migration in 3D linearly elastic matrices? While initial studies suggested that HT1080 fibrosarcoma cells do not undergo lobopodial migration but instead migrate via either an amoeboidal (i.e., large blebs with no adhesions) or mesenchymal (lamellipodia with actin stress fibers and adhesions) mode, recent work shows that fibrosarcoma cells (i.e. HT1080 and SW684) are able to activate lobopodia upon protease inhibition in 3D CDM (60). In general, MMPs are needed for matrix degradation and generation of migration tracks through which cells move using primarily a pseudopodial mode of migration. Upon inhibition of protease activity, cells switch to a bleb-based amoeboidal migration mechanism (59,61). It is worth noting that these observations were made using non-

linearly elastic materials such as collagen gels. In linearly elastic 3D CDM, however, MMP inhibition triggers the activation of nuclear piston mechanism in fibrosarcoma cells without switching to an amoeboid phenotype, possibly as a result of difficulty of efficient nuclear and cell translocation through low porosity confined 3D microenvironments. Similar to fibroblasts, lobopodial migration in tumor cells still depends on integrin adhesion, actomyosin contractility and nesprin3-vimentin connection.

While it is intriguing that fibroblasts and fibrosarcomas are able to migrate with a lobopodial mode that is completely distinct from the conventional lamellipodial one, it is still unknown how the cells are able to sense the differences of the elastic behaviors of the surrounding 3D microenvironment and trigger the switch of migration mode. Furthermore, it is still unclear how MMP inhibition triggers the switch from lamellipodial to lobopodial migration in fibrosarcomas. More studies are also warranted to determine if the lobopodial migration mode is also applicable in other cancer cell types that are not fibroblast-like, and also to elucidate the *in vivo* functional significance of lobopodial migration.

**2.7 The osmotic engine model**

Up to this point, all of the confined migration mechanisms that we have discussed so far require intact actin and myosin contractility functions. For instance, actin polymerization is critical for the formation of lamellipodial protrusions; Rho/ROCK/myosin contractility is needed for nucleus to pressurize lobopodial cells; actomyosin contractility and retrograde actin flows are essential to generate blebs and maintain amoeboidal migration. Actin polymerization and myosin contractility are indispensable for cell migration on 2D and 3D microenvironments.

It was fascinating to observe that several tumor cell lines, such as S180 sarcoma and MDA-MB-231 breast carcinoma, are able to migrate through stiff, narrow ($W$=3 μm and $H$=10 μm) PDMS-based microchannels even when actin polymerization is completely disrupted by high doses of latrunculin A (97). Also, efficient migration through narrow channels occurs upon inhibition of β1 integrin function or actomyosin contractility (97). We proposed the "osmotic engine model" of confined cell migration, which depends on the fluxes of water and ions in and out of the cells through the cell membrane (104). In this model, cells expand by taking up water at their leading edge and shrink by expelling water at the trailing edge, thereby leading to cell locomotion. Mathematical modeling predicts that the velocity of cell motility is independent of parameters that are influenced by actin polymerization or actomyosin contractility but instead depends on the number and localization of water channels, ion channels and pumps along the longitudinal cell axis (104). Indeed, the $Na^+/H^+$ exchanger-1, NHE-1, is polarized at the cell leading edge during confined migration. Knocking down NHE-1 or aquaporin-5 markedly suppress confined migration (104).

The osmotic engine model operates based on the principles of cell volume regulation as a result of differential osmotic and hydrostatic pressure across the cell membrane of leading and trailing edges. Therefore, any perturbation to the osmolarity of the fluid at either the cell leading or trailing edge has an immediate and pronounced effect on the flow of ions or water across the cell membrane, thereby affecting migration directionality and velocity. Indeed, application of a hypotonic osmotic shock to the cell leading edge or a hypertonic osmotic shock to the trailing edge reverses the direction of cell migration in narrow channels. It is worth noting that though

actin is dispensable in maintaining directionally persistent confined migration in these cells once the initial polarization of aquaporins and ion transporters has been established after channel entry, actin is pivotal for the cells to respond to osmotic shock and reverse direction by facilitating NHE1 repolarization (104). This is in contrast to the role of microtubule in confined migration, where microtubule disruption with nocodazole drastically impairs the persistence and velocity of cells pre-shocked, but only has minor effect post osmotic shock without affecting NHE1 repolarization.

The osmotic engine model relies on the polarization of key molecules, such as aquaporins, ion channels and pumps, aided by the actin cytoskeleton and the geometry of confined channels, which induce cells into a longitudinal pill-shaped morphology. Moreover, mathematical modeling predicts that the water permeation mechanism is key to migration inside stiff, narrow microchannels in which cells experience high hydraulic resistance, which is related to the extracellular pressure on the cell (unpublished data). Thus, it remains to be established whether the osmotic engine model operates *in vivo* where tissues and extracellular matrices are soft, porous and permeable to water in all directions. In light of the plasticity of the different migration mechanisms, it is still unclear how the osmotic engine model of confined migration is related or convertible to other migration mechanisms discussed in previous sections, or whether it represents an auxiliary mechanism. It is noteworthy that ROCK1, which phosphorylates myosin light chain, has been reported to be an upstream activator of NHE1, and could potentially serve as a functional switch between actomyosin-mediated migration and the osmotic engine model (128).

The osmotic engine model of migration may be relevant to cancerous cells which typically overexpress aquaporins, ion channels and pumps (129-131), and can thus uptake and/or expel water more effectively than their normal counterparts. If cells cannot uptake water, then they need to push against a column of water during migration in stiff, confined microchannels. This so called barotaxis mechanism was demonstrated for differentiated HL60 neutrophil-like cells (132) as evidenced by the fact that the bulk velocity of the moving fluid anterior to the cell is identical to that of moving cells. When HL60 cells encounter an asymmetric bifurcation of different hydraulic resistances, cells tend to follow the path of lower resistance. The leading edge of HL60 cells protruding into the lower resistance channel extends at significantly faster rate than the other competing edge, eventually causing the losing edge to retract, thereby precipitating the final cell decision to the lower resistance channel. This directional bias becomes more evident as the hydraulic resistance difference increases to the point that almost no HL60 cells are able to enter a dead-end branch where it presents infinite hydraulic resistance. In marked contrast, about 20% of MDA-MB-231 breast cancer cells, which employ the osmotic engine model, enter the dead-end branch channel (unpublished data). Taken together, cells, and in particular cancerous cells, may both push and take up water concurrently when moving in stiff, confined channels, and thus the two mechanisms are not mutually exclusive. Cells may use hydraulic resistance to probe the path of least resistance in order to determine the most efficient path of migration, and directed flow of water from the osmotic engine model could serve as additional “fuel” to facilitate cell translocation.

## 2.8 Conclusion

Cell migration is a complex process which necessitates the interplay of various intrinsic and extrinsic factors. Confinement further contributes to the complexity of cell migration mechanisms by providing a physical cue that cells have to integrate and alter intracellular signaling to ensure optimized and efficient cell migration. Recent breakthroughs in bioengineering and microfabrication techniques have provided researchers with various useful tools to orthogonally control biochemical and physical inputs and recapitulate physiologically relevant microenvironments encountered *in vivo* in order to systematically investigate the effects of physical confinement on cell signaling and motility. These studies have provided us with invaluable insights on how confined cell migration occurs. Several intrinsic cellular factors, such as actomyosin contractility, integrin expression, MMP activity, actin and microtubules, as well as extrinsic characteristics of surrounding matrix, such as adhesiveness, porosity, stiffness, elastic property and osmolarity, contribute to this intricate network that controls the mechanism of confined migration. Cells choose their preferred mode of migration depending on the physicochemical properties of the local microenvironment and the cellular contractile state. Cells display high plasticity and are capable of switching from one migration mode to another with ease. Understanding the mechanisms of confined cell migration thus offers promise for the development of novel therapeutic strategies, that can target the different facets of cell motility, for diseases arising from dysregulated cell migration like cancer metastasis.

## 2.9 Figures and tables

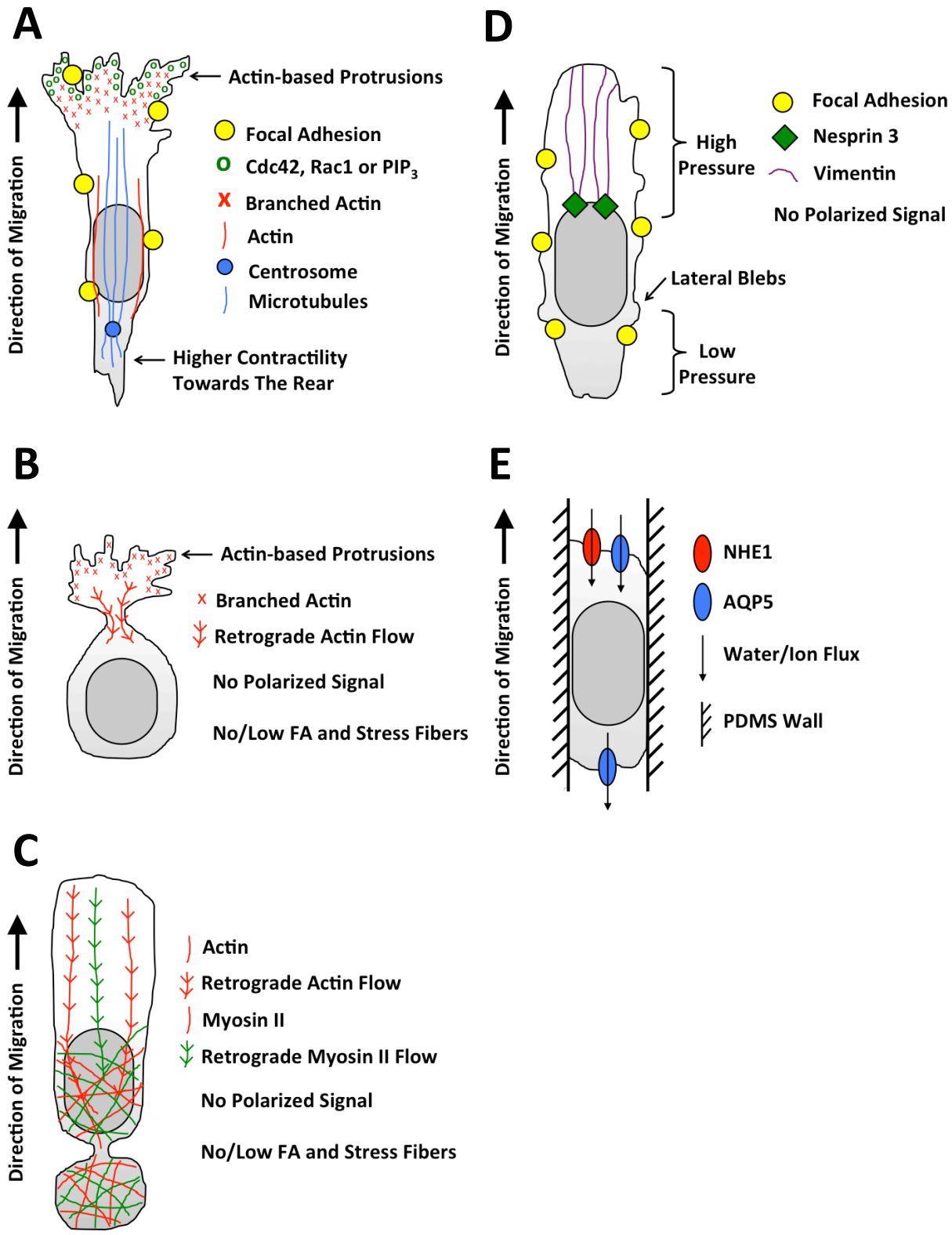

**Figure 2.1 Schematics of the various confined cell migration modes**

**(A)** Pseudopodial cell migrates with an elongated morphology and actin-based protrusions initiated by polarized Cdc42, Rac1 and $PIP_3$ localized at the cell's leading edge. Focal adhesions are distributed in a diffused pattern along the elongated cell. Actomyosin contractility is concentrated towards the trailing edge to aid in rear retraction. Actin are organized around the cell cortex and at the cell's leading and trailing edges. Centrosome is located behind the nucleus while microtubules are concentrated anterior to the nucleus as parallel bundles. **(B)** A1 blebbing cell has a round cell body with small actin-based protrusions at the leading edge. Fast retrograde actin flow is localized at the protruding leading edge. A1 blebbing cells also lack polarized signals, focal adhesions and actin stress fibers. **(C)** A2 blebbing cell has en elongated ellipsoidal morphology with a rear uropod and a rounded leading edge. Actin and myosin II are concentrated around the cell cortex and the uropods, and demonstrates fast and global retrograde flow towards the cell rear. A1 blebbing cells also lack polarized signals, focal adhesions and actin stress fibers. **(D)** Lobopodial cell possess blunt cylindrical protrusions and small lateral blebs around the cell body. Focal adhesions are required for lobopodial migration. Lobopodial cell is separated into a high-pressure compartment anterior to the nucleus and a low-pressure compartment posterior to the nucleus. The nucleus is connected to the anterior cell membrane via a vimentin and nespri3. Polarized signals are absent in lobopodial cell. High cellular contractility and a linearly elastic matrix are necessary for cell to migrate using lobopodia. **(E)** Osmotic engine is activated when cells are being confined into a pill shape within rigid channels. Ion and water channels such as NHE1 and AQP5 are polarized to the cell leading edge to facilitate water and ion flux that serve to propel the cells forward. Focal adhesion, contractility and actin polymerization are dispensable in cells migrating using the osmotic engine.

**Table 2.1 Comparison between unconfined 2D versus confined 1D or 3D mesenchymal migration**

| | 2D | 1D or 3D |
|---|---|---|
| ***Occurrence*** | | |
| *In vitro* | - Flat 2D substrates<br>- Wide PDMS channels | - Microcontact printed 1D line<br>- 3D hydrogel network<br>- Hydrogel patterned microtracks<br>- Narrow PDMS channels |
| *In vivo* | - Wound healing<br>- Neutrophil trafficking on inflamed endothelium | - Along oriented ECM fibers<br>- Within dense fibrillar tissues<br>- Pre-formed ECM-free tunnels |
| ***Structural and Phenotypic Properties*** | | |
| Actin | - Organized and elongated stress fibers | - Suppression of stress fibers<br>- Actin organized in cortex or concentrated on the leading/trailing edge |
| Microtubules | - Centrosome in front of nucleus<br>- Nearly isotropic microtubule polymerization from MTOC | - Centrosome behind the nucleus<br>- Stabilized microtubules as parallel bundles in front of nucleus<br>- Alpha tubulin and microtubule growth towards leading edge |
| Focal adhesion | - Large distinct mature focal adhesions around cell periphery | - Smaller in size<br>- Diffuse and homogenous distribution of focal adhesion proteins |
| Nuclear shape | - Rounded | - Elongated |
| Traction force | - Larger<br>- Directed to the cell center | - Significantly lower<br>- Directed towards channel wall |
| ***Roles of different molecular determinants*** | | |
| MMPs | - Not critical | - Essential in 3D ECM to generate migration tracks<br>- Not required if tracks are already pre-formed |
| Matrix adhesion | - Migration stops when adhesion is blocked | - Migration persists even when adhesion is blocked, especially in stiff PDMS-based channels |
| Actomyosin contractility | - Indispensable | - Effect is cell-type dependent<br>- Can be dispensable for cells in rigid microchannels |
| Microtubule | - Required for signal polarization | - Needed to maintain persistence and directionality |

## Table 2.2 Summary of confined single cell migration mechanisms

| | Matrix adhesion | Actomyosin contractility | MMPs | Physical micro-environment | Polarization | Other structural requirements | Note |
|---|---|---|---|---|---|---|---|
| ***Pseudopodial*** | - Required | - Cell-type dependent<br>- Can occur with both low and high contractility | - Needed in 3D ECM<br>- Inhibition leads to amoeboidal phenotype<br>- Dispensable if there are pre-exiting tracks | - Adhesive matrix<br>- Non-linearly elastic matrix<br>- ECM-free tracks/channels | - Polarized $PIP_3$, Rac1 and Cdc42 at the cell leading edge | - Microtubule needed for directional persistence and uniaxial morphology | |
| ***A1 Blebbing*** | - Low adhesion | - Low contractility<br>- Activation of contractility converts A1 to A2 | - Not relevant | - Vertical confinement | - Unknown | - Localized actin retrograde flow at small leading edge protrusions | - Faster than pseudopodial |
| ***A2 Blebbing*** | - Low adhesion | - High contractility<br>- Inhibition of contractility converts A2 to A1 | - Not relevant | - Vertical confinement | - Colocalization of contractile machinery and ERM protein family<br>- Stochastic contractility driven by cortical network instabilities | - Global actin and myosin II retrograde flow towards cell rear | - Faster than pseudopodial and A1 blebbing |
| ***Lopobodial*** | - Required | - High contractility needed<br>- Inhibition of contractility converts lobopodial to pseudopodial | - MMP inhibition activates lopobodial mode in fibrosarcoma cells | - Adhesive matrix<br>- 3D linearly elastic matrix (dermal tissue explants or cell-derived matrix) | - Non-polarized $PIP_3$, Rac1, Cdc42, cortactin, VASP and F-actin | - Myosin II-Vimentin-Nesprin3 nucleus-membrane connection<br>- Independent of Rac1, Cdc42 and mDia1 | - Observed in only fibroblasts and fibrosarcomas<br>- High intracellular pressure separated by nucleus |
| ***Osmotic Engine*** | - Dispensable | - Dispensable | - Not relevant | - Full confinement by rigid PDMS | - Polarized aquaporins, ion channels and pumps at the cell leading edge | - Overexpression of aquaporins, ion channels and pumps | - Actin polymerization is dispensable for movement once polarization is achieved but needed for repolarization post osmotic shock |

# Chapter 3 - A Direct Podocalyxin-Dynamin-2 Interaction Regulates Cytoskeletal Dynamics to Promote Migration and Metastasis in Pancreatic Cancer Cells

## 3.1 Abstract

The sialoglycoprotein podocalyxin is absent in normal pancreas but is overexpressed in pancreatic cancer and is associated with poor clinical outcome. Here we investigate the role of podocalyxin in migration and metastasis of pancreatic adenocarcinomas using SW1990 and Pa03c as cell models. Although ezrin is regarded as a cytoplasmic binding partner of podocalyxin that regulates actin polymerization via Rac1 or RhoA, we did not detect podocalyxin-ezrin association in pancreatic cancer cells. Moreover, depletion of podocalyxin did not alter actin dynamics or modulate Rac1 and RhoA activity in pancreatic cancer cells. Using mass spectrometry, bioinformatics analysis, co-immunoprecipitation, and pulldown assays, we discovered a novel, direct binding interaction between the cytoplasmic tail of podocalyxin and the large GTPase dynamin-2 at its GTPase, middle, and pleckstrin homology domains. This podocalyxin-dynamin-2 interaction regulated microtubule growth rate, which in turn modulated focal adhesion dynamics and ultimately promoted efficient pancreatic cancer cell migration via microtubule- and Src-dependent pathways. Depletion of podocalyxin in a hemispleen mouse model of pancreatic cancer diminished liver metastasis without altering primary tumor size. Collectively, these findings reveal a novel mechanism by which podocalyxin facilitates pancreatic cancer cell migration and metastasis.

### 3.2 Introduction

Podocalyxin (PODXL) is a type 1 transmembrane sialomucin glycoprotein belonging to the CD34 protein subfamily that is endogenously expressed by kidney podocytes (133), hematopoietic progenitor stem cells (134) and vascular endothelium (135). First discovered in adult kidney, the negatively charged ectodomain of PODXL is instrumental for the maintenance of glomerular filtration slits via an anti-adhesive charge repulsion effect (133). In contrast, PODXL expressed on high endothelial venules is instead pro-adhesive, capable of mediating binding to L-selectin on lymphocytes, thereby facilitating lymphocytes tethering, rolling and recruitment to secondary lymphoid organs during inflammation (135).

PODXL plays a pivotal role in regulating cell adhesion, a fundamental aspect of many (patho)physiological processes, including embryonic development, inflammatory and immune responses and cancer metastasis. Importantly, PODXL is also overexpressed by cancer cells, including lung (136), breast (137), ovarian (138), bladder (139), renal (140), colorectal (141) and pancreatic cancers (142). Overexpression of PODXL in cancer cells is associated with aggressive clinicopathological characteristics and poor clinical outcomes (136-142). Both the anti- and pro-adhesive roles of the PODXL ectodomain have been implicated in cancer dissemination. For instance, PODXL has been reported to disrupt cell-cell contact and induce tumor shedding from monolayers of ovarian carcinoma (138), and breast cancer cells (137). Conversely, PODXL, expressed on colon carcinoma (143) and pancreatic cancer cells (144), binds to E- and L-selectin, thereby facilitating circulating cancer cell rolling on vascular endothelium and subsequent extravasation to secondary tumor sites. The structure of PODXL consists of an N-terminal extracellular domain with extensive N- and O-glycosylation and sialylation, and a cytoplasmic

intracellular tail with a C-terminal DTHL consensus sequence capable of interacting with PDZ binding domain (145). The cytoplasmic tail of PODXL, despite its small size has been reported to interact with proteins such as ezrin (140,146) and Na(+)/H(+) exchange regulatory cofactor (NHERF) 1 or 2 (147,148) to activate downstream intracellular signaling, primarily via the PI3K (149), RhoA (147) and Rac1 (140) pathways, leading to epithelial-mesenchymal transition (150), migration (151) and invasion (152).

While typically absent in normal pancreas and non-malignant pancreatic epithelial cells, approximately 30-69% of pancreatic ductal adenocarcinomas express PODXL, with the strongest expression exhibited by the invasive front of primary tumors (144,153,154). Moreover, high PODXL expression is associated with poor clinicopathological characteristics and the development of distant metastasis (155,156). PODXL has also been shown to be an independent predictor of poor prognosis and is linked to higher risk of death and reduced survival (142,154-156). These effects are hypothesized to be at least partially due to the ability of PODXL to regulate cell migration and invasion (154,156). Although ezrin is regarded as the main intracellular binding partner of PODXL, our data reveal the lack of any association between PODXL and ezrin in pancreatic cancer cells. Consequently, the mechanism by which PODXL exerts its downstream effects to promote pancreatic cancer cell migration remains unknown. Furthermore, the functional significance of PODXL in promoting pancreatic cancer cell metastasis *in vivo* has yet to be delineated.

In this study, we examined the roles of PODXL in migration and metastasis of pancreatic cancer cells *in vitro* and *in vivo*, using two metastatic pancreatic cancer cell lines, SW1990 and Pa03c.

To identify the cytoplasmic binding partner of PODXL in pancreatic cancer cells, we immunoprecipitated PODXL from SW1990 cells, and subjected the specimens to tandem mass spectrometry. Bioinformatics analysis identified dynamin-2 as a potential binding partner of PODXL. Reciprocal co-immunoprecipitation (co-IP) verified the association of PODXL and dynamin-2. This direct binding interaction was further confirmed by *in vitro* His-tag binding assays, which identified the GTPase, middle and pleckstrin homology domains of dynamin-2 as critical for binding to PODXL. Of note, co-IP assays failed to demonstrate any PODXL-ezrin association. The novel PODXL-dynamin-2 interaction modulates microtubule dynamics, which in turn modulates focal adhesion (FA) assembly/disassembly. Dynamin-2 also regulates FA turnover via Src kinase-dependent pathway. As a result, inhibition or downregulation of dynamin-2, microtubule or Src kinase reverses the pro-migratory phenotype of PODXL in both two-dimensional (2D) and microchannel migration assays. Along these lines, knockdown of PODXL significantly impairs unconfined and confined migration by decreasing microtubule dynamics and increasing FA density. The functional role of PODXL in promoting metastasis is demonstrated using a preclinical murine hepatic metastasis model via a hemispleen injection technique (157).

## 3.3 Materials and methods

### 3.3.1 Cell culture and drug treatment

SW1990 pancreatic cancer cells and MDA-MB-231 breast cancer cells were purchased from the American Type Culture Collection (Manassas, VA), while Pa03c pancreatic cancer cells were obtained as previously described (158). All cell lines were cultured in standard Dulbecco's Modified Eagle Medium (DMEM, Gibco) supplemented with 10% heat-inactivated fetal bovine

serum (FBS, Gibco) and 1% penicillin/streptomycin (Gibco). All cell lines were used for 10 passages after thawing from the frozen vials and were tested routinely for mycoplasma via quantitative polymerase chain reaction. The cell lines were not further authenticated. In select experiments involving drug treatments, cells were incubated with culture media containing 40 μM dynasore (Sigma-Aldrich), 1.2 μM taxol (Sigma-Aldrich), 10 nM dasatinib (Cell Signaling), 10 μM PP2 (EMD Millipore), or the corresponding vehicle control.

### 3.3.2 Generation of stable knockdown cell lines

Stable cell lines of scramble control and PODXL-KD SW1990 were generated with short hairpin RNA (shRNA) as previously described (144). Additional PODXL-KD cell lines with Pa03c and MDA-MB-231 were generated using two different lentiviral shRNA sequences. PODXL-KD1, which is identical to the original PODXL-KD sequence used for SW1990 cells (144), targets the 3' untranslated region, whereas PODXL-KD2 targets the coding region of the PODXL mRNA. The shRNA target sequences are (5' to 3' sense strand), Scramble: GCACTACCAGAGCTAACTCAGATAGTAC. PODXL-KD1: GAGCCAGGATGAGAACAAA. PODXL-KD2: CCTAACACCACAAGCAGCCAGAATGGAGC. The shRNA sequences were cloned into pLVTHM (Addgene, plasmid # 12247) lentivector expressing shRNA with a GFP selection marker via Mlul and Clal restriction sites or pLKO.1 puro (Addgene, plasmid # 8453) lentivector with a puromycin antibiotic selection marker via BshT1 and EcoR1 restriction sites with standard molecular cloning techniques. The viruses were produced in HEK293T cells. Pa03c PODXL-KD cell lines were generated using the pLVTHM lentivector while MDA-MB-231 PODXL-KD cell lines were generated using the pLKO.1 puro lentivector. Successfully

transduced cells were sorted using Sony Biotechnology SH800 Cell Sorter for GFP expression or selected with puromycin accordingly.

Stable cell lines of scramble control and NHERF2-KD SW1990 were generated using a lentiviral approach. The shRNA target sequences for knocking down NHERF2 are (5' to 3' sense strand), NHERF2-KD1: AACAGGAAGCGTGAAATCTTCAGCAACTT. NHERF2-KD2: CGAGACAGATGAACACTTCAA. NHERF2-KD3: GAAGCGTGAAATCTTCAGCAA. NHERF2-KD4: GTCCTGCCATTGCCCAGAAAT. The NHERF2 shRNA sequences were cloned into pLKO.1 puro lentivector.

### 3.3.3 siRNA knockdown

Transient dynamin-2 knockdown was established by transfecting cells with Dynamin-2 siRNA (Santa Cruz Biotechnology, sc-35236) using Lipofectamine RNAiMAX (Invitrogen) following the manufacturer's protocol. As a control, cells were transfected with scramble control siRNA (Santa Cruz Biotechnology, sc-35236). Cells were incubated with the lipid complex for 72 h before they were used for subsequent experiments.

### 3.3.4 Western blot and antibodies

Standard western blot techniques were performed as previously described (159) using NuPAGE 4-12% Bis-Tris Protein Minigels (Invitrogen). The antibodies used are listed below. Primary antibodies: 1) Podocalyxin-like 1 (3D3) mouse monoclonal antibody (Santa Cruz Biotechnology, sc-23904, 1:500). 2) PODXL (EPR9518) rabbit monoclonal antibody (Abcam, ab150358,

1:1000). 3) Dynamin-2 (DYN2-11) mouse monoclonal antibody (Sigma Aldrich, SAB4200661, 1:500). 4) Dynamin-2 rabbit polyclonal antibody (Abcam, ab3457, 1:1000). 5) Ezrin (3C12) mouse monoclonal antibody (Abcam, ab4069, 1:500). 6) NHERF2 (D3A5) rabbit monoclonal antibody (Cell Signaling, 9568, 1:1000). 7) GST (26H1) mouse monoclonal antibody (Cell Signaling, 2624, 1:2000) 8) 6x-His tag (4E3D10H2/E3) mouse monoclonal antibody (ThermoFisher Scientific, MA1-135, 1:2000). 9) RhoA (7F1.E5) mouse monoclonal antibody (Cytoskeleton, ARH04, 1:500). 10) Rac1 mouse monoclonal antibody (Cytoskeleton, ARC03, 1:500). 11) Actin (C4) mouse monoclonal antibody (BD Transduction, 612656, 1:10000). Secondary antibodies: 1) Anti-mouse IgG, HRP-linked antibody (Cell Signaling, 7076S, 1:2000). 2) Anti-rabbit IgG, HRP-linked antibody (Cell Signaling, 7074S, 1:2000).

### 3.3.5 Random 2D migration assay

22mm×22mm square glass coverslips glued to the bottom a 6-well plate were coated for 1 h with 20 μg/ml of rat tail type I collagen (Gibco). $5\times10^4$ cells were seeded onto the coverslips with 2 ml of culture media. The cells were imaged via a 10x Ph1 objective every 10 min for 10 h using stage automation on a Nikon Inverted microscope with a stage top incubator (Tokai Hit Co., Shizuoka, Japan) maintained at 37°C with 5% $CO_2$ and humidity. At least 5 individual migrating single cells from 5 different locations per sample were analyzed using ImageJ (National Institutes of Health, Bethesda, MD). The cell outlines were tracked at every time point to record their spatial position and morphology parameters including projected area, circularity and solidity as previously described (160). A rose plot with the cell migration trajectories and their average mean square displacement were also calculated as described in (160).

### 3.3.6 Polydimethylsiloxane (PDMS)-based microchannel migration assay

PDMS-based microchannels devices were fabricated using a photolithography and standard replica molding technique as previously described (77,97). Each device comprises a series of parallel 200 μm-long and 10 μm-high microchannels of prescribed widths varying from 6, 10, 20 to 50μm arrayed perpendicularly between a cell and chemoattractant inlet lines. The microchannels devices were coated with 20 μg/ml of collagen type I to facilitate cell adhesion. Cell migration was visualized and recorded via time-lapse live microscopy in an enclosed, humidified microscope stage maintained at 37°C and 5% $CO_2$ using stage automation and a Nikon Inverted microscope. Phase contrast time-lapse images were taken at every 10 min for 24 h with a 10x Ph1 objective. The spatial x and y positions of all non-dividing and viable cells that entered and migrated in the microchannels were tracked overtime with the Manual Tracking plugin in ImageJ. Motility parameters, namely velocity, speed and persistence, were computed using a custom-written Matlab code as previously described (77,97).

### 3.3.7 Actin dynamics with fluorescence recovery after photobleaching (FRAP)

Cells were transfected with LifeAct-GFP (Addgene, plasmid # 58470) using Lipofectamine 3000 (Invitrogen) according to manufacturer's protocol. 48 h post transfection, cells were replated onto a 35 mm glass bottom dish coated with 20 μg/ml of collagen type I and allowed to adhere overnight to grow into a 70-80% confluent monolayer. The cells were imaged using a Zeiss LSM 700 laser scanning confocal microscope (Zeiss, Oberkochen, Germany) with a 63×/1.4 NA oil-immersion objective every 1.04 s before and after photobleaching. A circular region of interest of 4 μm diameter was positioned at cell-cell borders of cells expressing LifeAct-GFP, which was then photobleached using a 488nm laser at 100% power. At least 25 different cell-cell borders

were imaged per condition. The FRAP time-lapse video was analyzed with ImageJ by as previously described (161).

### 3.3.8 Microtubule dynamics with EB1-GFP

Cells were transfected with EB1-GFP (Addgene, plasmid # 17234) using Lipofectamine 3000. 48 h post transfection, cells were replated onto collagen I-coated glass bottom dishes and allowed to adhere overnight. Individual cells expressing EB1-GFP were imaged at an interval of 3.08 s for a total duration of 6 min with a 63×/1.4 NA oil-immersion objective on a Zeiss LSM 700 laser scanning confocal microscope. At least 20 different EB1-GFP expressing cells were imaged per condition. The time-lapse confocal raw images were exported to and analyzed via ImageJ as previously described (97).

### 3.3.9 FA density measurement with total internal reflectance fluorescence (TIRF) microscopy

$5\times10^4$ cells were seeded onto collagen I-coated glass bottom dishes and allowed to adhere overnight. Cells were fixed in 4% paraformaldehyde for 10 min, permeabilized in 0.25% Triton X-100 for 5 min, and blocked for 2 h in PBS with 10% normal goat serum (Cell Signaling) and 1% bovine serum albumin. Cells were incubated with primary antibody against phosphor-paxillin (Tyr118) (Cell Signaling, 2541S, 1:100) overnight at 4°C, followed by 2 h incubation with Alexa Fluor 488 goat anti-rabbit secondary antibody (Invitrogen, A11034, 1:200). The cells were washed thoroughly with PBS between each step. The immunostained cells were imaged by TIRF microscopy using a 3i Mariana inverted microscope (Intelligent Imaging Innovation, Denver, CO, USA) equipped with a 100×/1.45 NA oil immersion objective and Slidebook 8.0

software. At least 60 cells were analyzed per condition. The TIRF images were processed and analyzed for FA density as previously described (160).

### 3.3.10 RhoA and Rac active pulldown assays

RhoA Pulldown Activation Assay (Cytoskeleton, BK036) and Rac1 Pulldown Activation Assay (Cytoskeleton, BK035) were conducted according to manufacturer's protocols.

### 3.3.11 Co-IP and mass spectrometry

Co-IP was performed to identify the binding partner(s) of PODXL in pancreatic cancer cells with Pierce co-IP Kit (Thermo Scientific). The co-IP assays were performed by incubating pre-cleared cell lysates containing 500 μg of total protein with 25 μl of resin immobilized with 10 μg of antibody overnight at 4°C. PODXL (EPR9518) rabbit monoclonal antibody (Abcam, ab150358) was used to immunoprecipitate PODXL. A rabbit IgG monoclonal isotype (EPR25A, Abcam, ab172730) or beads-only controls were included to account for non-specific binding. Unbound proteins were washed away from the antibody-immobilized resin by centrifugation with IP lysis buffer supplemented with 1M NaCl for 10 times. Bound proteins were eluted with 1% SDS and concentrated. The co-IP elution was submitted to the Johns Hopkins Mass Spectrometry and Proteomics Core Facility (Baltimore, MD, USA) for protein identification or analyzed with standard western blot protocol once the candidate protein was identified. In subsequent reciprocal co-IP experiments, Dynamin-2 rabbit polyclonal antibody (Abcam, ab3457) or NHERF2 (D3A5) rabbit monoclonal antibody (Cell Signaling, 9568) were used to immunoprecipitate dynamin-2 or NHERF2, respectively.

### 3.3.12 *In-Vitro* His-tag pulldown assay

*In-vitro* His-tag pulldown assays were conducted using a recombinant purified His-DNM2 probe (Gift from Dr. Mark McNiven) (162). Additional His-DNM2 constructs consisting of select Dynamin-2 domains, and the His-tagged PODXL cytoplasmic tail (PCT, aa484 to aa558) were created using standard molecular cloning techniques with the same pQE-80L vector as the full length His-DNM2 probe. His-tagged constructs were transformed into and produced with BL21 Competent *E.coli* under 0.1 mM Isopropyl β-D-1-thiogalactopyranoside induction at 16°C overnight. The recombinant His-tagged proteins were purified using HisPur™ Ni-NTA Spin Purification Kit (Thermo Scientific). The *in vitro* pulldown assay was performed using Pierce™ His Protein Interaction Pull-Down Kit (Thermo Scientific). For experiments involving purified glutathione S-transferase (GST)-tagged PCT, GST-PCT is cloned into pGEX-2T vector via standard molecular cloning techniques. The recombinant GST-PCT proteins were induced and purified from *E.coli* using glutathione–agarose beads (Pierce).

### 3.3.13 Colocalization staining

$5\times10^4$ cells were plated onto collagen I-coated glass bottom dishes and allowed to adhere overnight. Cells were fixed in 4% paraformaldehyde for 10 min, permeabilized in 1% Triton X-100 for 10 min, and blocked for 2 h in blocking buffer comprising PBS with 2% bovine serum albumin and 0.1% Triton X-100. Cells were incubated with Podocalyxin-like 1 (3D3) mouse monoclonal antibody (Santa Cruz Biotechnology, sc-23904, 1:50) and Dynamin-2 rabbit polyclonal antibody (Abcam, ab3457, 1:300) diluted in blocking buffer simultaneously overnight at 4°C, followed by 2 h incubation with Alexa Fluor 488 goat anti-mouse secondary antibody (Invitrogen, A11001, 1:200), Alexa Fluor 568 goat anti-rabbit secondary antibody (Invitrogen,

A11011, 1:200) and Hoechst 33342 (ThermoFisher Scientific, H3570, 1:2000) diluted in blocking buffer. The samples were washed thoroughly with PBS between each step. Imaging was performed with a 63×/1.4 NA oil-immersion objective on a Zeiss LSM 700 laser scanning confocal microscope.

### 3.3.14 Hemispleen mice model

A preclinical murine model of hepatic metastasis was performed via a hemispleen injection technique (157) to assess the metastatic potential of PODXL-expressing and PODXL-KD pancreatic cancer cells. All animal work was approved and performed in compliance with the Institutional Animal Care and Use Committee (IACUC) at the Johns Hopkins University. Prior to surgery, trypsinized cells were incubated in DMEM with 10% FBS at 37°C with intermittent mixing to restore surface glycoprotein expression. Next, the cells were washed with PBS 3X and resuspended in anti-clumping buffer diluted 1:1000 in Hanks' balanced salt solution (Gibco) to single cell suspensions of $1\times10^7$/ml for Pa03c and $2.5\times10^6$/ml for SW1990. The cells were maintained on ice at all times for subsequent steps. 6 to 8 weeks old female NOD-SCID mice were purchased from Johns Hopkins Research Animal Resources (Baltimore, MD, USA) and maintained in accordance with Institutional Animal Care and Use Committee guidelines. At surgery, the spleen of a fully anesthetized mouse was eviscerated, clipped and excised into 2 halves. 100 µl of cell suspension was injected into one half of the excised spleen, followed by a flush with 150 µl of ice-cold PBS. The cells were allowed to flow into the liver via the splenic vessels for 2 min, after which the splenic vessels were clipped and removed, followed by suturing. All mice were monitored regularly and sacrificed when they display morbid characteristics. At necropsy, livers were harvested and examined macroscopically and

microscopically with haematoxylin and eosin staining for evidence of metastases. Additionally, any visible splenic tumors formed at the injection sites were collected and measured for size with the formula, V=(LxWxW)/2, where V is the tumor volume, L is the tumor length and W is the tumor width.

### 3.3.15 Immunohistochemistry

Immunohistochemistry staining for PODXL in the primary splenic tumor samples was performed manually. Following tissue deparaffinization and hydration, heat-induced antigen retrieval was performed in EDTA buffer (pH9.0) using a steamer for 40 min at 100°C. The tissue was then blocked for endogenous peroxidase and alkaline phosphatase (Dual Endogenous Enzyme Blocking Reagent, Dako), and endogenous biotin, biotin receptors and avidin binding sites (Avidin/Biotin Blocking Kit, Vector Laboratories). Primary antibody incubation with PODXL (EPR9518) rabbit monoclonal antibody (Abcam, ab150358, 1:500) for 1 h was followed by incubation with biotinylated secondary goat antibodies against rabbit IgG (Vector Laboratories, BA-100, 1:500) for 30 min, with TBST washes following each incubation steps. For detection, the sample was first incubated with ABC Vectastain reagent (Vector Laboratories) for 30 min, followed by development with DAB substrate (Dako) for 4 min. All slides were counterstained with haematoxylin.

### 3.3.16 *In vitro* and *in vivo* tumor growth assays

To quantity the effects of PODXL knockdown on *in vitro* growth rate, equal number of scramble control and PODXL-KD SW1990 or Pac03c cells at $1\times10^5$ were seeded into 6 well plates. Cell growth was quantified each day by counting the total number of cells per well following

trypsinization using a Countess Automated Cell Counter (Invitrogen) for each cell line in triplicates for 6 days. To assess the same parameter *in vivo,* a subcutaneous implantation model was used. $1\times10^6$/ml scramble control or PODXL-KD SW1990 or Pa03c cancer cells in 50% matrigel (Sigma Aldrich, diluted into 50% with equal volume of culture media) were injected subcutaneously into both flanks of 6-8 weeks old NOC-SCID mice. The animals were sacrificed appropriately when at least a mouse started to develop tumor that exceed 2 mm in diameter. Tumors were harvested post mortem and weighed with an electronic balance. All animal work was approved and performed in compliance with the Institutional Animal Care and Use Committee at the Johns Hopkins University.

### 3.3.17 Statistical analysis

All data are presented as mean±S.E.M. from 3 independent experiments unless otherwise stated. Graphing and statistical analyses were performed with GraphPad Prism. Statistical significance was determined between pairs of data with a t-test, or between groups of data with one-way ANOVA and a Tukey's Multiple Comparison post-hoc test.

## 3.4 Results

### 3.4.1 PODXL knockdown impairs pancreatic cancer cell migration *in vitro*

We generated scramble control and stable PODXL-KD SW1990 cells via lipofectamine transfection followed by clonal selection. PODXL knockdown was verified via immunoblotting (**Figure 3.1.A**). We first investigated the potential role of PODXL in regulating random 2D migration of pancreatic cancer cells on collagen I-coated glass coverslips. Scramble control

relative to PODXL-KD SW1990 cells were more motile (**Figure 3.1.B**), as evidenced by their higher mean squared displacement (**Figure 3.1.C**), and as such, were able to explore a larger surrounding area (**Figure 3.1.D**). Interestingly, morphometric analysis revealed that PODXL knockdown renders cells smaller, more circular and less protrusive (**Figure 3.S1.A**). Depletion of PODXL also diminishes cell morphodynamics, as evidenced by smaller changes of their various morphological indices (**Figure 3.S1.B**). In line with random 2D migration data, PODXL knockdown significantly suppressed chemotactically-driven cell migration inside both unconfined and confined PDMS-based microchannels (**Figure 3.1.E**), which resulted in lower velocity, speed and persistence relative to scramble control cells (**Figure 3.1.F**).

To validate our observations, we knocked down PODXL on both SW1990 and Pa03c pancreatic cancer cells using two different shRNA lentivirus sequences. Both sequences were able to knockdown PODXL (**Figure 3.S1.C**) and suppress migration of SW1990 (**Figure 3.S1.D**) and Pa03c (**Figure 3.S1.E**) cells through both unconfined and confined microchannels. To further generalize our findings and to extend their significance to other cancer cell types, we also knocked down PODXL in the widely-used human breast cancer cell line, MDA-MB-231 (**Figure 3.S1.C**), and observed a similar inhibition in cell migration through both unconfined and confined microchannels (**Figure 3.S1.F**).

### 3.4.2 PODXL knockdown alters microtubule and adhesion dynamics in pancreatic cancer cells

Given the pronounced effect of PODXL knockdown in altering cell morphology and slowing down cell migration, we hypothesized that PODXL mediates these changes by regulating

cytoskeletal and/or adhesion dynamics in pancreatic cancer cells. We first quantified actin dynamics in scramble control and PODXL-KD LifeAct-GFP-transfected SW1990 cells using FRAP. Both control and PODXL-KD cells exhibited nearly identical mobile fractions of LifeAct-GFP molecules and half-lives of recovery (**Figure 3.2.A**), suggesting that PODXL knockdown does not alter actin dynamics. We next investigated the effects of PODXL knockdown on microtubule dynamics by imaging and quantifying the rate of EB1-GFP incorporation to the positive growing ends of microtubules. Interestingly, SW1990 PODXL-KD cells demonstrated a significantly lower microtubule growth rate compared to the scramble control cells (**Figure 3.2.B**), thereby indicating that PODXL depletion slows down microtubule dynamics.

To investigate the potential role of PODXL in regulating cell adhesion, we visualized FAs by staining scramble control and PODXL-KD SW1990 cells for phosphorylated paxillin and imaging by TIRF microscopy (**Figure 3.2.C**). PODXL-KD cells relative to scramble controls displayed a higher FA density, quantified either as number of individual FAs over total cell area or as percentage of total cell area covered by FAs (**Figure 3.2.D**). Interestingly, the sizes of the individual FAs were not different between scramble control and PODXL-KD cells.

Most cytoskeletal and adhesion dynamics changes are regulated by the activity of small GTPase proteins, such as RhoA and Rac1 (163). However, neither active RhoA (**Figure 3.S2.A**) nor active Rac1 (**Figure 3.S2.B**) were differentially modulated following PODXL knockdown, indicating that the microtubule and adhesion changes induced by PODXL are mediated by a distinct mechanism that is independent of both Rac1 and Rho.

### 3.4.3 PODXL associates with dynamin-2 in pancreatic cancer cells

Ezrin is one of the most commonly reported cytoplasmic binding partners of PODXL, where it serves as a scaffold that links the plasma membrane to actin cytoskeleton (140,149). PODXL-ezrin interaction has also been reported to promote migration by activating Rac1 and RhoA (140,147,152). Given that PODXL knockdown fails to alter both actin dynamics and the activities of RhoA and Rac1 (**Figure 3.2.A**, **Figure 3.S2.A-B**), we questioned the validity of PODXL-ezrin interaction in pancreatic cancer cells. Interestingly, we failed to detect ezrin in immunoprecipitated PODXL specimens from SW1990 cell lysates (**Figure 3.3.A**), thereby indicating that PODXL does not associate with ezrin in pancreatic cancer cells.

To identify the cytoplasmic binding partner of PODXL in pancreatic cancer cells, we immunoprecipitated PODXL using a PODXL-specific antibody, EPR9518, along with an appropriate IgG isotype and beads-only (no antibody) controls. Specimens were subjected to mass spectrometry followed by bioinformatics analysis. Only proteins enriched by at least two-fold in PODXL immunoprecipitated samples relative to those of isotype or beads-only control specimens were selected for further analysis (**Table 3.1**).

Among the listed proteins, dynamin-2 emerged as a promising candidate for the following reasons. First, dynamin-2 is a large GTPase protein that associates with microtubules and promotes their dynamic instability (164). Second, dynamin-2 triggers FA disassembly (162). Third, dynamin-2 is overexpressed in pancreatic ductal carcinoma cells and potentiates migration and invasion (165). As such, we hypothesized that dynamin-2 could serve as a novel cytoplasmic

binding partner of PODXL and function as its effector to induce cytoskeletal and migratory changes in pancreatic cancer cells.

By performing reciprocal co-IP experiments using specific antibodies against PODXL and dynamin-2, we demonstrated their physical association in SW1990 pancreatic cancer specimens. Specifically, in PODXL co-IP samples, dynamin-2 was also pulled down and detected only in the PODXL antibody lane, but not in the beads-only or isotype control lanes (**Figure 3.3.B**). Similarly, in dynamin-2 immunoprecipitated specimens, PODXL was also found to be co-IPed (**Figure 3.3.B**). These findings were validated and extended using Pa03c pancreatic cancer cells (**Figure 3.S3.A**) as well as MDA-MB-231 breast cancer cells (**Figure 3.S3.B**).

Immunofluorescence followed by confocal microscopy revealed the colocalization of PODXL and dynamin-2 around the cell membrane and the thin cytoplasmic area surrounding the nucleus in SW1990 cells (**Figure 3.S3.C**). While PODXL localizes apically in primary cilium (166), embryonic and stem cells (167), normal endothelial and epithelial cells (168,169), and is crucial for the formation of apical lumen in blood vessels (170,171), its spatial localization is not as extensively characterized in cancer cells. Although ectopically expressed PODXL has been reported to localize to the apical surface of OVCAR-3 ovarian and MCF7 breast cancer cells (138,172), confocal imaging disclosed the presence of endogenous PODXL not only at the apical but also at the basal surfaces of SW1990 pancreatic cancer cells (**Figure 3.S3.C**). This spatial localization pattern of PODXL at the basal surfaces enables it to interact and ultimately affect focal adhesion dynamics in pancreatic cancer cells.

To identify the essential domains of dynamin-2 responsible for binding to PODXL, probes consisting of 6x His tags fused to either full-length or truncated constructs encompassing different domains of dynamin-2 were generated and used in *in vitro* His-tag pulldown assays (**Figure 3.3.C**). His-tagged full-length dynamin-2 pulled down PODXL following incubation with SW1990 cell lysate (**Figure 3.3.D**). These assays further revealed that the GTPase, middle and pleckstrin homology domains of dynamin 2 are responsible for binding PODXL, as His-constructs containing either of these domains individually or in combination with others were able to pull down PODXL (**Figure 3.3.D**). On the other hand, the GTPase effector domain and the proline-rich domain of dynamin-2 were found to be dispensable for this binding interaction (**Figure 3.3.D**). Moreover, recombinant His-tagged PCT (aa484 to aa558) was sufficient to bind to endogenous dynamin-2 from SW1990 cell lysate (**Figure 3.3.E**). Importantly, we herein demonstrate the direct and specific binding interaction between PODXL and dynamin-2 via *in vitro* His-tag pulldown assays using both purified recombinant dynamin-2 domains and PCT. Specifically, we show that purified GST-tagged PCT binds to recombinant His-tagged dynamin-2 D3+D4 domains, but not to D4 alone (**Figure 3.3.F**). To further demonstrate the specificity of this binding interaction, we show that purified GST alone does not bind to either His-tagged constructs (**Figure 3.3.F**). Taken together, mass spectrometry followed by bioinformatics analysis, co-IP, colocalization staining and *in vitro* His-tag pulldown assays disclose that PODXL and dynamin-2 interact directly to form a complex in pancreatic cancer cells.

### 3.4.4 Pro-migratory phenotypes of PODXL-expressing cells are coupled to dynamin-2 function

To assess the functional significance of PODXL-dynamin-2 interaction, a dynamin-2 inhibitor, dynasore, or siRNA (siDNM2) were used in both scramble control and PODXL-KD SW1990 cells. Dynasore (40 μM) significantly reduced the migration velocities of scramble control SW1990 cells to the identical levels of the DMSO-treated PODXL-KD cells in both unconfined and confined microchannels (**Figure 3.4.A**). Interestingly, dynasore had no additional inhibitory effect on PODXL-KD SW1990 cells. Similar phenotypic mimicry was also observed in the microtubule growth rate using EB1-GFP (**Figure 3.4.B**) and FA density (**Figure 3.4.C**).

To eliminate any potential off-target effects of dynasore, siDNM2 was used to knock down dynamin-2 expression in both scramble control and PODXL-KD SW1990 cells (**Figure 3.S4.A**). Of note, PODXL knockdown did not affect dynamin-2 expression (**Figure 3.S4.A**). Similar to the data acquired using dynasore, dynamin-2 depletion decreased the migration of the scramble control SW1990 cells to the levels of PODXL-KD, without altering migration in PODXL-KD cells (**Figure 3.S4.B**). Cumulatively, these data disclose the functional role of dynamin-2 in mediating the cytoskeletal remodeling and pro-migratory effects of PODXL on pancreatic cancer cells.

According to mass spectrometry results, NHERF2 was also enriched in the immunoprecipitate fraction of PODXL (**Table 3.1**). Since NHERF2 has been reported to act as a scaffolding protein that bridges the interaction between PODXL and ezrin in glomerular foot processes (148), we sought to delineate the potential role of NHERF2 in PODXL-dependent migration. Although

NHERF2 interacts with PODXL in SW1990 pancreatic cancer cells as evidenced by co-IP assays, dynamin-2 was not detected in the NHERF2 immunoprecipitate fraction (**Figure 3.S4.C**). Also, NHERF2 was not detected in the dynamin-2 immunoprecipitate fraction (**Figure 3.S4.D**). We next generated NHERF2-KD SW1990 cells using shRNA lentivirus (**Figure 3.S4.E**), and compared their migratory potential to that of scramble controls. In distinct contrast to PODXL-KD and dynamin 2-KD cells, which displayed a markedly reduced migration velocity, NHERF2-KD cells moved much faster than scramble control cells (**Figure 3.S4.F**). Of note, NHERF2-KD cells exhibit a clear mesenchymal/protrusive phenotype in contrast to the epithelial/rounded morphology of scramble control or PODXL-KD cells. In view of these findings and given that PODXL and/or dynamin-2 knockdown suppress migration to an equivalent extent without any additive effect, we conclude that dynamin-2 regulates PODXL-mediated migration of pancreatic cancer cells via its direct binding interaction with PODXL (**Figure 3.3.F**). The precise role of NHERF2 in pancreatic cancer cell migration, which may extend beyond PODXL, deserves further investigation that goes beyond the scope of this current study.

### 3.4.5 Microtubule and Src kinase are downstream effectors of PODXL-dynamin-2 complex

Because PODXL knockdown (**Figure 3.2.B**) and dynamin-2 inhibition (**Figure 3.4.B**) slow down microtubule growth with similar efficiency, we reasoned that microtubules represent a downstream target of the PODXL-dynamin-2 signaling cascade. In light of prior work showing that dynamin-2 regulates microtubule dynamic instability (164), we examined the effects of taxol, which stabilizes microtubules by preventing their depolymerization. Treatment of scramble control SW1990 cells with taxol (1.2 μM) had the same effect as dynamin-2

inhibition/knockdown or PODXL knockdown. Specifically, taxol suppressed the migration velocities of scramble control cells to the levels of untreated PODXL-KD cells (**Figure 3.4.D**). Of note, PODXL-KD SW1990 cells treated with taxol displayed a further, albeit moderate, reduction of migratory potential in microchannels with a width ≥10 μm, thereby indicating a potential mild synergistic effect.

Microtubule polymerization towards FAs has been reported to induce FA disassembly, leading to more dynamic FAs (173). Along these lines, stabilizing microtubules via cell treatment with taxol increased both FA density and the percentage of total cell area covered by FAs in scramble control, but not PODXL-KD, SW1990 cells (**Figure 3.4.E**). Taken together, our data are in concert with the notion that PODXL, through its binding to dynamin-2, regulates microtubule dynamics, which in turn modulates FA assembly and disassembly.

Evidence suggests that dynamin-2 forms a trimeric complex with FAK and Src kinase to induce FA disassembly by activating integrin endocytosis (162). Interestingly, treatment of scramble control SW1990 cells with the Src kinase inhibitor dasatinib (10 nM) recapitulated the phenotypic responses of PODXL knockdown. Specifically, dasatinib concurrently reduced the migration velocities (**Figure 3.4.F**) and increased the FA density and the percentage of total area covered by FAs (**Figure 3.4.G**) in scramble control cells. In marked contrast, Src kinase inhibition had a negligible effect on PODXL-KD SW1990 cells (**Figure 3.4.F, Figure 3.4.G**). Interestingly, dasatinib failed to modulate microtubule dynamics (**Figure 3.S4.G**), suggesting that Src kinase regulates migration and FA dynamics downstream of PODXL without involving microtubules. To validate the role of Src kinase in PODXL-dynamin-2-dependent migration of

pancreatic cancer cells, we also assessed the effect of PP2, a more specific Src kinase inhibitor, on migration of both SW1990 scramble control and PODXL-KD cells. Similar to Dasatinib, PP2 inhibition reduced the velocity of the scramble control cells down to the same level as the PODXL-KD cells, without affecting the velocity of PODXL-KD cells (**Figure 3.S4.H**).

### 3.4.6 PODXL knockdown decreases liver metastasis *in vivo*

To test whether the enhanced migratory propensity of PODXL-expressing cells observed *in vitro* facilitates metastasis *in vivo*, we employed the well-established preclinical model of pancreatic cancer metastasis to the liver following a hemispleen injection technique (157). To this end, we injected $1\times10^6$ scramble control or PODXL-KD Pa03c pancreatic cancer cells into the spleen of mice (n=15 for scramble, n=12 for PODXL-KD). Knockdown of PODXL significantly decreased liver metastasis, as evidenced by the gross anatomy photographs (**Figure 3.5.A**) and further confirmed microscopically via histology (**Figure 3.5.B**). PODXL knockdown generated significantly smaller number of visible liver macrometastasis foci in mice (**Figure 3.5.C**). It is noteworthy that the size of the primary splenic tumor at the injection site was similar between scramble control and PODXL-KD Pa03c cells (**Figure 3.5.D**). Of note, immunohistochemistry staining for PODXL in primary splenic tumors derived from mice injected with PODXL-KD Pa03c cells showed a dramatic reduction in PODXL staining intensity relative to scramble control specimens (**Figure 3.5.E**), indicating that PODXL knockdown was maintained throughout the entire duration of the *in vivo* hemispleen experiment.

We replicated the aforementioned findings with a second pancreatic cancer cell line, SW1990. Because of the larger size of SW1990 than Pa03c cells, injection of the $1\times10^6$ cells resulted in

high post-operative mortality approximating 90%, possibly due to clotting and thrombosis. Another potential reason for the differential prothrombotic profile of the two pancreatic cancer cell types could stem from inherent differential surface expression of procoagulant molecules, such as tissue factor that can initiate the coagulation cascade (174). In breast cancer cells, clotting time was determined to be both tissue factor- and cell number- dependent (175). As such, a lower number of cells ($2\times10^5$) was attempted for injection into the spleen of mice to mitigate this issue. While the lower cell number did improve postoperative survival, about 40% of the mice still died after surgery. Despite the lower sample size (n=7 for scramble, n=5 for PODXL-KD), the inhibitory effect of PODXL knockdown on liver metastasis was even more pronounced, as almost all mice injected with the scramble control SW1990 cells developed liver metastasis, whereas only one out of five mice injected with PODXL-KD SW1990 cells developed metastasis (**Figure 3.S5.A, Figure 3.S5.B, Figure 3.S5.C**). In concert with our findings using Pa03c cells, PODXL also failed to alter primary splenic tumors size (**Figure 3.S5.D**). Moreover, PODXL knockdown was preserved *in vivo* for SW1990 tumors as evidenced by immunohistochemistry (**Figure 3.S5.E**).

The growth of scramble control versus PODXL-KD cells was unaltered *in vitro* and in a subcutaneous injection model *in vivo* as quantified by the weight of tumors harvested post-mortem, using Pa03c (**Figure 3.S5.F, Figure 3.S5.G**) and SW1990 (**Figure 3.S5.H, Figure 3.S5.I**) cells. Collectively, these data reveal that the increased metastatic potential of PODXL-expressing cells is attributed to their elevated capacity to migrate and metastasize in the liver rather than to proliferate at higher levels at the primary tumor site per se.

### 3.5 Discussion

By employing mass spectrometry followed by bioinformatics analysis, co-immunoprecipitation and *in vitro* His-tag pulldown assays, we herein demonstrate a novel direct binding interaction between the cytoplasmic tail of PODXL and the large GTPase dynamin-2. Given that PODXL knockdown and dynamin-2 inhibition suppress with similar efficiency microtubule growth rate, and that dynamin-2 is a microtubule-associated large GTPase, we reasoned that microtubules are a downstream target of the PODXL-dynamin-2 signaling cascade. This is further substantiated by a previous study showing that dynamin-2 regulates dynamic instability of microtubules (164). Because PODXL knockdown or dynamin-2 inhibition or stabilization of microtubules via cell treatment with taxol increase FA density and the percentage of total cell area covered by FAs, we propose a model by which PODXL, through its binding to dynamin-2, regulates microtubule dynamics, which in turn modulates FA assembly and disassembly (**Figure 3.6**). Specifically, we postulate that PODXL binds to and activates dynamin-2 at the cell periphery, where dynamin-2 could enhance the dynamic instability of microtubules, causing microtubules to polymerize more towards existing FA and promote FA disassembly. Alternatively, dynamin-2, by forming a trimer with FAK and Src kinase (162), could also regulate FA turnover via a Src kinase pathway (**Figure 3.6**). Along these lines, our data reveal that Src kinase inhibition concurrently reduces cell migration and increases the FA density in scramble control, but not PODXL-KD, cells. We further postulate that both the microtubule- and Src kinase-dependent pathways, which are downstream of the PODXL-dynamin-2 signaling axis, regulate FA dynamics, thereby ultimately facilitating cell migration and metastasis (**Figure 3.6**). This proposed model was rigorously tested by inhibiting dynamin-2, microtubules and Src kinase. Interfering with any of these downstream targets causes the scramble cells to phenotypically mimic the PODXL-KD cells, as

evidenced by their slower cell migration, decreased microtubule growth rate and increased FA density, thus validating their functional significance in propagating the downstream effects of PODXL.

The cytoplasmic domain of PODXL, despite its short size, has been reported to associate with proteins, such as ezrin and NHERF1/2 to mediate downstream signaling involved in cytoskeletal remodeling and cell migration (140,146). PODXL is considered to form a stable complex with ezrin, which in turns connects to actin filaments, leading to redistribution of actin towards the apical membrane in kidney podocytes (146). NHERF1 and 2, which are two highly homologous scaffold proteins with two PDZ domains and an ERM binding domain, interact directly with PODXL and serve as a linker between PODXL and ezrin (148). Interestingly, the N-terminus of ezrin has also been reported to bind directly to the HQRIS sequence in the juxtamembrane region of PODXL independent of NHERF1/2 (147). Binding of ezrin to PODXL, either directly or indirectly, activates ezrin, which in turn activates RhoA through sequestration of RhoGDI by activated ezrin (147). With its second PDZ domain binding to PODXL, the first PDZ domain of NHERF1 can also bind to Rac1 guanine nucleotide exchange factor ARHGEF7 to activate Rac1, promoting lamellipodia formation and cell migration (140).

Although ezrin has emerged as a widely accepted binding partner of PODXL, there are reports showing that PODXL and ezrin may have non-related or even opposing effects in certain cancer types, thereby suggesting that the PODXL-ezrin association may not be as universal as one is led to believe. In urothelial bladder cancer, for instance, while high membranous PODXL expression correlates with poor prognosis (139), low membranous expression ezrin was instead an

independent marker of progression and disease-specific survival in another study (176). In our study, we consistently and repeatedly failed to identify the presence of ezrin in immunoprecipitated PODXL specimens either via immunoblotting or mass spectrometry. Moreover, the inability of PODXL knockdown to alter actin dynamics and RhoA or Rac1 activity in pancreatic cancer cells further suggests that the pro-migratory role of PODXL is independent of the actin cytoskeleton and the classical Rac1 and/or RhoA signaling induced by ezrin following its binding to PODXL. Collectively, these previous reports showing that PODXL and ezrin have opposing effects on tumor cells, coupled with our data showing the absence of PODXL-ezrin association and the inability of PODXL knockdown to alter actin polymerization, strongly support the existence of a novel cytoplasmic binding partner, which we demonstrated to be dynamin-2.

While there have been several *in vitro* studies on PODXL and its involvement in cancer, there is no preclinical animal model study aimed to evaluate the potential oncogenic role of PODXL in pancreatic cancer. To the best of our knowledge, the well-established preclinical model of pancreatic cancer metastasis to the liver via an injection using the hemispleen technique represents the first ever-reported *in vivo* model that directly assesses the effect of PODXL on pancreatic cancer metastasis. Prior *in vivo* models associated with PODXL have been performed primarily with breast cancer cells, where impairment in the formation of lung metastases was demonstrated with tail vein injection, subcutaneous injection and orthotopic implantation into mammary fat pad for PODXL-KD cells (152,177). In our work, we demonstrate that PODXL knockdown exerts a pronounced inhibitory effect on liver metastasis using two distinct pancreatic cancer cell lines without affecting primary splenic tumor growth.

The KRAS oncogene undergoes mutational activation in 95% of pancreatic ductal adenocarcinoma patients, and plays a crucial role in initiating and driving pancreatic cancer pathogenesis (178). In addition to KRAS, signal transducer and activator of transcription 3 (STAT3) has been implicated in malignant transformation of pancreatic cancer (179). Interestingly, both KRAS and STAT3 interact with tubulin and microtubules (180,181). Moreover, oncogenic KRAS upregulates Src in pancreatic cancer cells (182). Because 69% of pancreatic ductal adenocarcinomas stain positively for PODXL (144), and given that MTs and Src regulate PODXL-dependent pancreatic cancer cell migration, the potential link among oncogenic KRAS, STAT3 and PODXL deserves to be investigated.

In conclusion, we discovered a novel direct binding interaction between PODXL and dynamin-2 that is critical for promoting the efficient migration *in vitro* and metastasis *in vivo* of pancreatic cancer cells. PODXL, through its binding to dynamin-2, regulates microtubule dynamics and Src activation, which in turn modulate FA assembly and disassembly, and ultimately regulate migration. The functional role of PODXL in promoting pancreatic cancer metastasis *in vivo* was demonstrated using a physiologically relevant hemispleen-based hepatic metastasis model.

### 3.6 Figures and tables

Figure 1

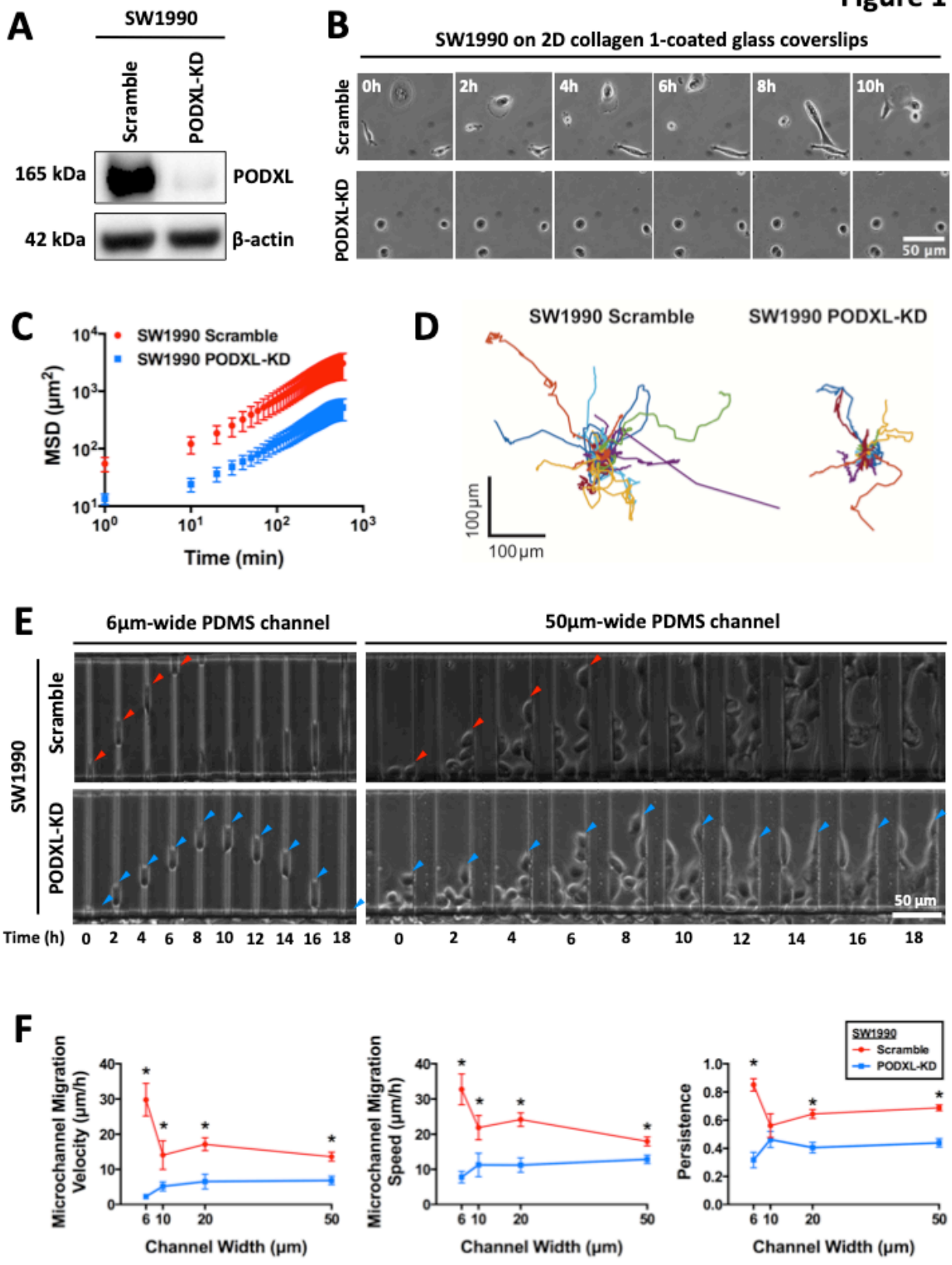

**Figure 3.1 PODXL knockdown in pancreatic cancer cells suppresses random 2D migration and chemotactic migration inside unconfined and confined channels**

**(A)** Western blot showing efficient knockdown of PODXL in SW1990 pancreatic cancer cells using shRNA lipofectamine transfection followed by stable clonal selection. **(B)** Representative time-lapse micrographs of scramble control and PODXL-KD SW1990 cells migrating on 2D collagen I-coated glass coverslips. The images are spaced at 2 h intervals. **(C)** Average mean squared displacement (MSD) over time of migrating scramble control and PODXL-KD SW1990 cells. Data represent the mean±S.E.M from 3 independent experiments. **(D)** Superimposed images of individual trajectories of scramble control and PODXL-KD SW1990 cells migrating on 2D collagen I-coated surfaces. **(E)** Representative time-lapse micrographs of scramble control (top row) and PODXL-KD (bottom row) SW1990 cells migrating inside 6 μm-wide, confined microchannels (left panels) and 50 μm-wide, unconfined microchannels (right panels). The images are spaced at 2 h intervals. Arrowheads indicate the leading edge of a migrating cell. **(F)** Migration velocity (left panel), speed (middle panel) and persistence (right panel) of scramble control and PODXL-KD SW1990 cells in PDMS-based microchannels of 10 μm in height, 200 μm in length, and either 6, 10, 20 or 50 μm in width. Data represent the mean±S.E.M from at least 3 independent experiments. * represents $p<0.05$ between scramble control and PODXL-KD cells.

**Figure 2**

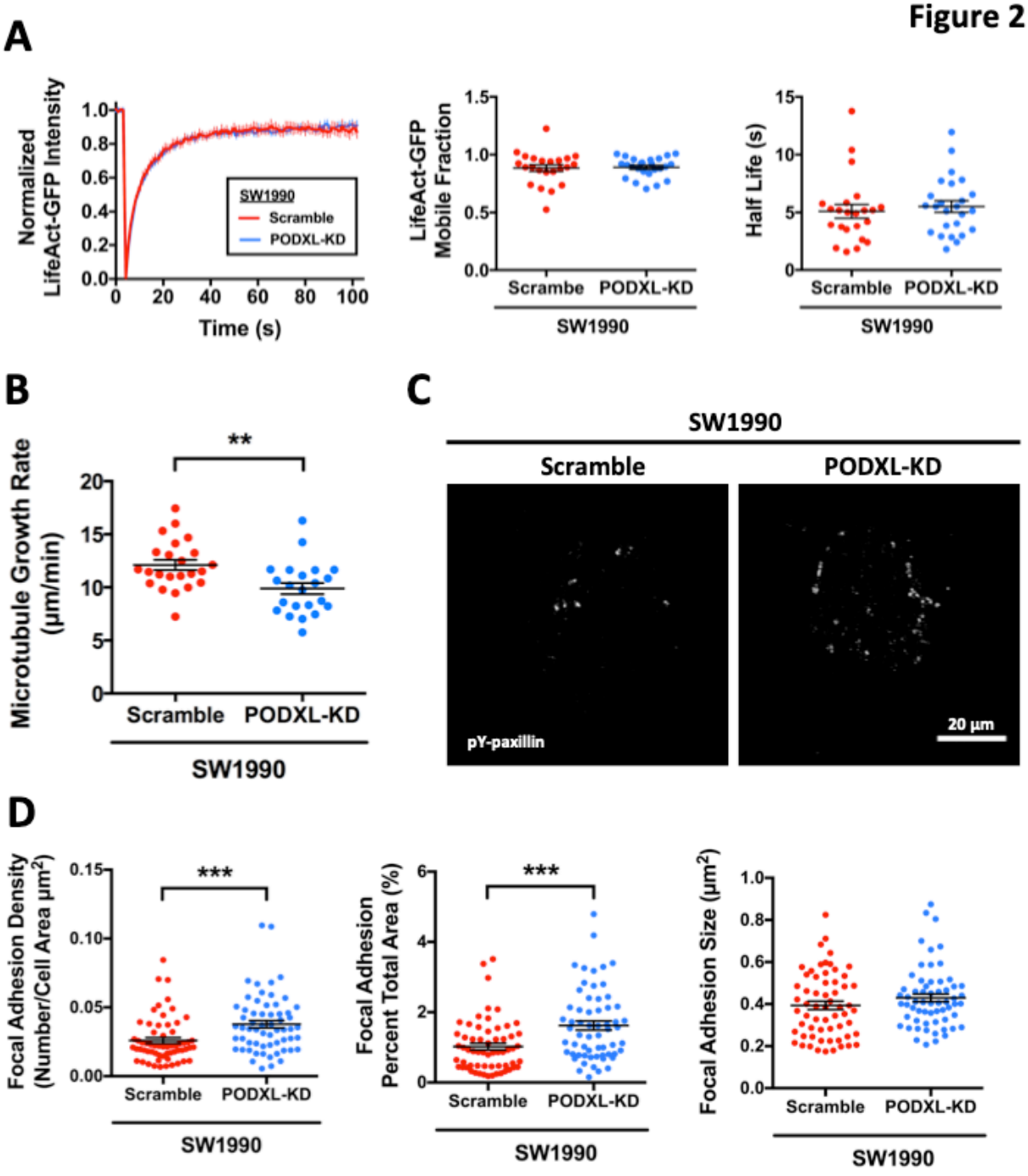
A
Normalized LifeAct-GFP Intensity
SW1990
Scramble
PODXL-KD
Time (s)
LifeAct-GFP Mobile Fraction
Scrambe
PODXL-KD
SW1990
Half Life (s)
Scramble
PODXL-KD
SW1990
B
Microtubule Growth Rate (µm/min)
**
Scramble
PODXL-KD
SW1990
C
SW1990
Scramble
PODXL-KD
pY-paxillin
20 µm
D
Focal Adhesion Density (Number/Cell Area µm²)
***
Scramble
PODXL-KD
SW1990
Focal Adhesion Percent Total Area (%)
***
Scramble
PODXL-KD
SW1990
Focal Adhesion Size (µm²)
Scramble
PODXL-KD
SW1990

**Figure 3.2 PODXL knockdown decreases microtubule growth rate and increases FA density without altering actin dynamics**

**(A)** Actin dynamics was assessed using FRAP at cell-cell junctions of scramble control and PODXL-KD SW1990 cells transiently transfected with LifeAct-GFP. Representative FRAP curves of the fraction of initial fluorescence intensity as a function of time for scramble control (red) and PODXL-KD (blue) cells (left panel). Mobile fraction (middle panel) and recovery half-life (right panel) of LifeAct-GFP molecules in scramble control and PODXL-KD SW1990 cells. Data represent the mean±S.E.M. from 3 independent experiments. **(B)** Average microtubule growth rate of scramble control and PODXL-KD SW1990 cells, as determined from the life history plots and kymographs of EB1 comets in cells transiently transfected with EB1-GFP. Data represent the mean±S.E.M from 3 independent experiments. **(C)** Representative TIRF microscopy images of immunostained phospho-paxillin in scramble control and PODXL-KD SW1990 cells. **(D)** Quantification of the average number of discrete FAs per cell area (left panel), FA area per total cell area (middle panel) and FA size (right panel) of scramble control and PODXL-KD SW1990 cells. Data represent the mean±S.E.M from 3 independent experiments. ** represents $p<0.01$ and *** represents $p<0.001$ between scramble control and PODXL-KD cells.

**Figure 3**

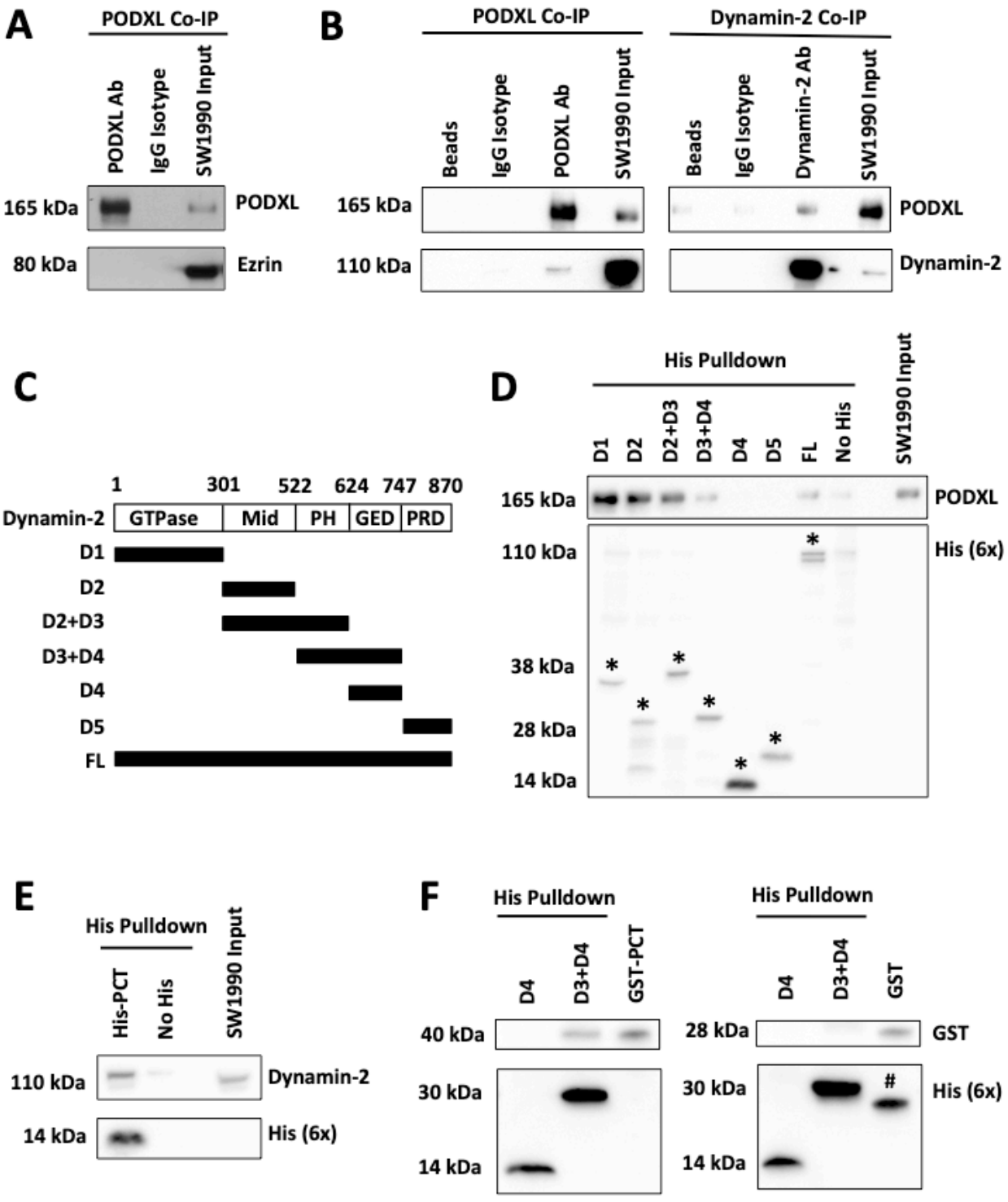
A
PODXL Co-IP
PODXL Ab
IgG Isotype
SW1990 Input
165 kDa
PODXL
80 kDa
Ezrin
B
PODXL Co-IP
Dynamin-2 Co-IP
Beads
IgG Isotype
PODXL Ab
SW1990 Input
Beads
IgG Isotype
Dynamin-2 Ab
SW1990 Input
165 kDa
PODXL
110 kDa
Dynamin-2
C
1
301
522
624
747
870
Dynamin-2
GTPase
Mid
PH
GED
PRD
D1
D2
D2+D3
D3+D4
D4
D5
FL
D
His Pulldown
D1
D2
D2+D3
D3+D4
D4
D5
FL
No His
SW1990 Input
165 kDa
PODXL
110 kDa
His (6x)
38 kDa
28 kDa
14 kDa
E
His Pulldown
His-PCT
No His
SW1990 Input
110 kDa
Dynamin-2
14 kDa
His (6x)
F
His Pulldown
D4
D3+D4
GST-PCT
40 kDa
30 kDa
14 kDa
His Pulldown
D4
D3+D4
GST
28 kDa
GST
30 kDa
#
His (6x)
14 kDa

**Figure 3.3 PODXL interacts with dynamin2 in pancreatic cancer cells**

**(A)** Ezrin was not detected in the immunoprecipitate fraction generated from SW1990 pancreatic cancer cells using a PODXL specific antibody. An IgG isotype antibody was used as a control. The right lane shows the presence of both PODXL and ezrin in SW1990 cell lysate input. **(B)** Co-IP experiments from SW1990 cell lysates were performed using either a PODXL (left panels) or a dynamin-2 (right panels) specific antibody along with matched isotype controls. The resultant immunoprecipitates were subsequently resolved with SDS-PAGE and blotted with antibodies against PODXL and dynamin-2. Dynamin-2 was detected in the immunoprecipitates of PODXL and vice versa. The right lanes in both panels reveal the presence of both PODXL and dynamin-2 in SW1990 cell lysate inputs. The left lanes in both panels show the beads-only (no antibody) controls. **(C)** His-tagged constructs encompassing different domains of dynamin-2 were used for the *in vitro* His-tag pulldown assay. Mid, middle domain; PH, pleckstrin homology domain; GED, GTPase effector domain; PRD, proline-rich domain. **(C)** *In-vitro* His-tag pulldown assays demonstrating that the GTPase, middle and pleckstrin homology domains of dynamin-2 are responsible for binding PODXL from SW1990 cell lysates. * denotes the respective His constructs. **(E)** *In-vitro* His-tag pulldown assay showing that His-tagged PODXL cytoplasmic tail (PCT) is sufficient to bind to endogenous dynamin-2 from SW1990 cell lysates. **(F)** *In-vitro* His-tag pulldown assay demonstrating that purified GST-tagged PCT binds to recombinant His-tagged dynamin-2 D3+D4 domains but not to D4 alone (left panel). Purified GST alone does not bind to either His-tagged constructs. # denotes the protein band of GST (28kDa) from previous immunoblotting with anti-GST antibody.

Figure 4

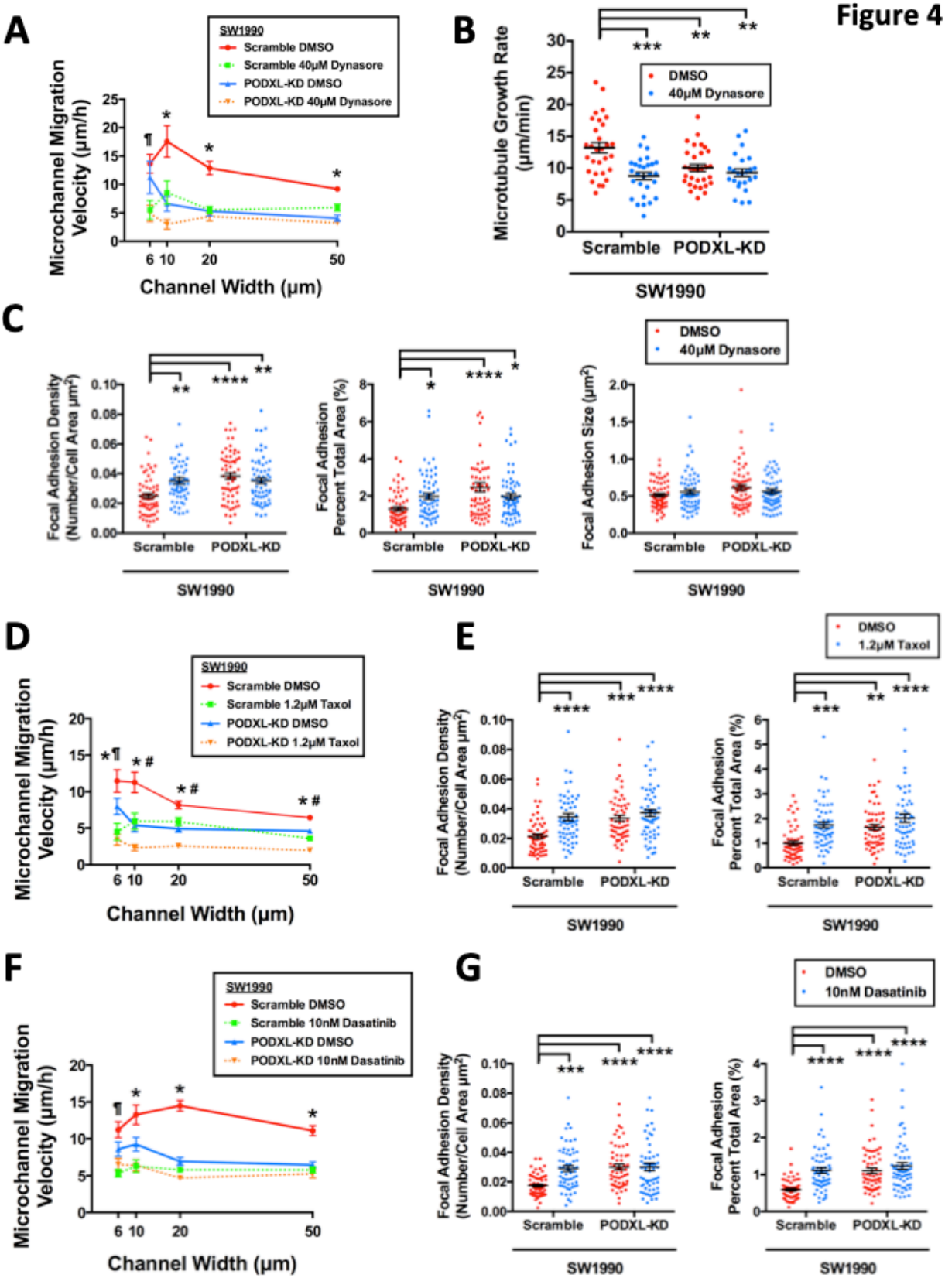
A
SW1990
Scramble DMSO
Scramble 40μM Dynasore
PODXL-KD DMSO
PODXL-KD 40μM Dynasore
Microchannel Migration Velocity (μm/h)
Channel Width (μm)
B
Microtubule Growth Rate (μm/min)
DMSO
40μM Dynasore
Scramble
PODXL-KD
SW1990
C
Focal Adhesion Density (Number/Cell Area μm²)
Focal Adhesion Percent Total Area (%)
Focal Adhesion Size (μm²)
DMSO
40μM Dynasore
Scramble
PODXL-KD
SW1990
D
SW1990
Scramble DMSO
Scramble 1.2μM Taxol
PODXL-KD DMSO
PODXL-KD 1.2μM Taxol
Microchannel Migration Velocity (μm/h)
Channel Width (μm)
E
DMSO
1.2μM Taxol
Focal Adhesion Density (Number/Cell Area μm²)
Focal Adhesion Percent Total Area (%)
Scramble
PODXL-KD
SW1990
F
SW1990
Scramble DMSO
Scramble 10nM Dasatinib
PODXL-KD DMSO
PODXL-KD 10nM Dasatinib
Microchannel Migration Velocity (μm/h)
Channel Width (μm)
G
DMSO
10nM Dasatinib
Focal Adhesion Density (Number/Cell Area μm²)
Focal Adhesion Percent Total Area (%)
Scramble
PODXL-KD
SW1990

**Figure 3.4 Inhibiting dynamin-2, microtubules or Src kinase abrogates the migratory potentiation and cytoskeletal remodeling effects of PODXL**

**(A)** Migration velocity of scramble control and PODXL-KD SW1990 cells inside microchannels of prescribed width after treatment with dynasore (40 μM). Data represent the mean±S.E.M. from 3 independent experiments. * represents $p<0.05$ between scramble DMSO control and all three other conditions, ¶ represents $p<0.05$ between scramble DMSO control versus scramble plus dynasore or PODXL-KD plus dynasore. **(B)** Microtubule growth rate of scramble control and PODXL-KD SW1990 cells following dynasore (40 μM) treatment as measured by an EB1-GFP assay. Data represent the mean±S.E.M from 3 independent experiments. ** represents $p<0.01$, *** represents $p<0.001$. **(C)** FA density quantified as the number of discrete FAs per cell area (left panel) or FA area per total cell area (middle panel) and FA size (right panel) of scramble control and PODXL-KD SW1990 cells following dynasore (40μM) treatment, as assessed by TIRF imaging of phospho-paxillin immunostaining. Data represent the mean±S.E.M, * represents $p< 0.05$, ** represents $p<0.01$, *** represents $p<0.001$, **** represents $p<0.0001$. **(D)** Migration velocity of scramble control and PODXL-KD SW1990 cells inside microchannels of prescribed width after taxol (1.2 μM) treatment. Data represent the mean±S.E.M. from 3 independent experiments. * represents $p<0.05$ between scramble DMSO control and all three other conditions. # represents $p<0.05$ between PODXL-KD plus taxol versus scramble plus taxol or PODXL-KD plus DMSO control. ¶ represents $p<0.05$ between PODXL-KD plus taxol versus PODXL-KD plus DMSO control. **(E)** FA density quantified as described in **(C)** using scramble control and PODXL-KD SW1990 cells after taxol (1.2μM) treatment, as assessed by TIRF imaging of phospho-paxillin immunostaining. Data represent the mean±S.E.M. from 3 independent experiments. ** represents $p<0.01$, *** represents $p<0.001$, **** represents

$p<0.0001$. **(F)** Migration velocity of scramble control and PODXL-KD SW1990 cells inside microchannels of prescribed width after dasatinib (10 nM) treatment. Data represent the mean±S.E.M. from 3 independent experiments. * represents $p<0.05$ between scramble DMSO control and all three other conditions, ¶ represent $p<0.05$ between scramble DMSO control versus scramble control plus dasatinib or PODXL-KD plus dasatinib. **(G)** FA density quantified as described in **(C)** using scramble control and PODXL-KD SW1990 cells after dasatinib (10 nM) treatment, as assessed by TIRF imaging of phospho-paxillin immunostaining. Data represent the mean±S.E.M from 3 independent experiments. *** represents $p<0.001$, **** represents $p<0.0001$.

Figure 5

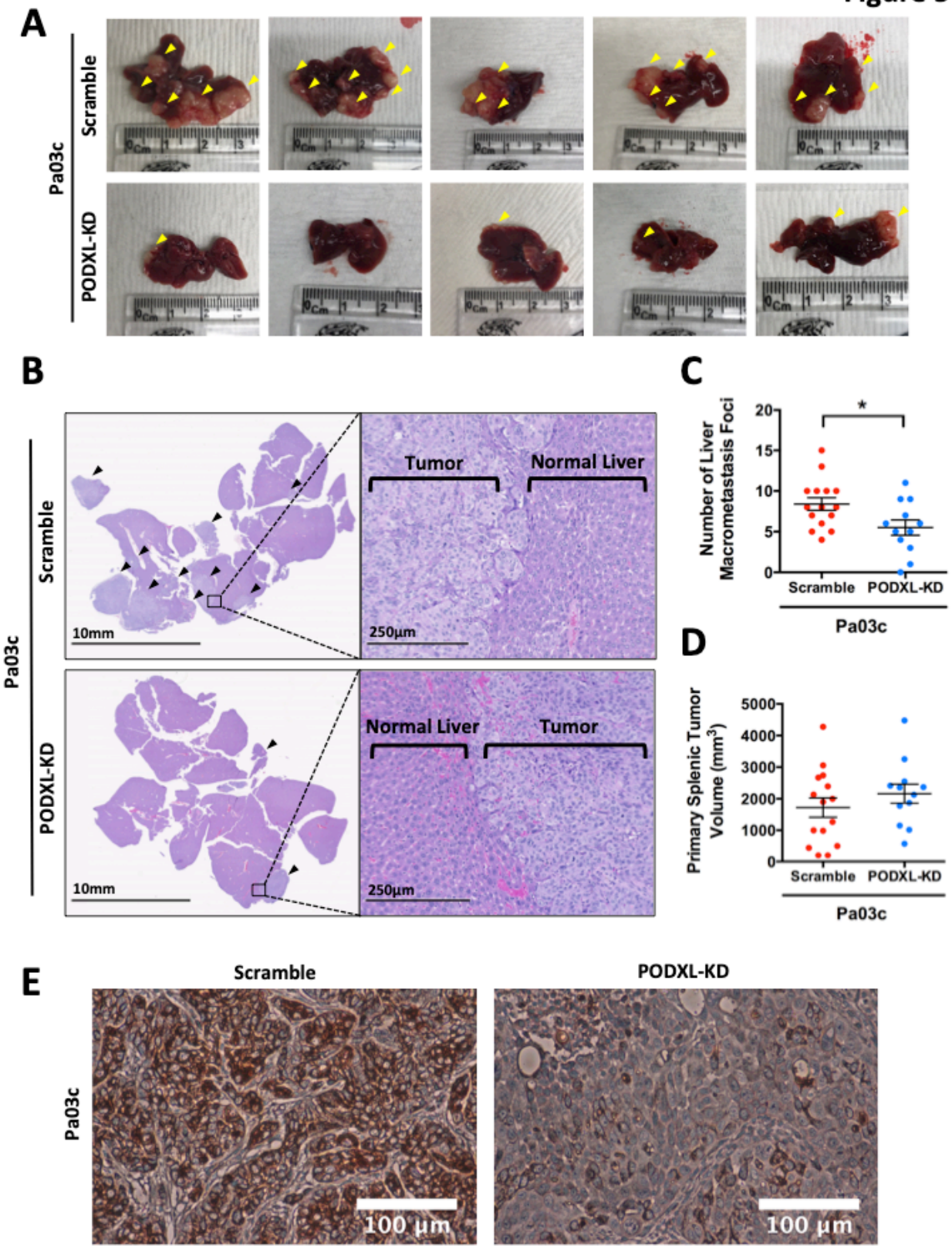
A
Pa03c
Scramble
PODXL-KD
B
Pa03c
Scramble
PODXL-KD
Tumor
Normal Liver
10mm
250µm
Normal Liver
Tumor
10mm
250µm
C
Number of Liver Macrometastasis Foci
20
15
10
5
0
*
Scramble
PODXL-KD
Pa03c
D
Primary Splenic Tumor Volume (mm3)
5000
4000
3000
2000
1000
0
Scramble
PODXL-KD
Pa03c
E
Scramble
PODXL-KD
Pa03c
100 µm
100 µm

**Figure 3.5 PODXL knockdown decreases metastasis *in vivo* in a preclinical murine model of pancreatic cancer metastasis using a hemispleen injection technique**

**(A)** Gross anatomical pictures of representative livers harvested from mice injected with scramble control (top row) or PODXL-KD (bottom row) Pa03c cells via the hemispleen technique. Yellow arrowheads indicate visible liver macrometastases. **(B)** Representative histological sections of livers harvested from mice injected with scramble control (top row) or PODXL-KD (bottom row) Pa03c cells. Black arrowheads indicate areas of metastasis. **(C)** Quantification of the number of visible liver macrometastasis foci observed on the harvested livers and **(D)** the volume of the primary splenic tumor of mice injected with scramble control or PODXL-KD Pa03c cells. Data represent the mean±S.E.M from 15 and 12 mice for the scramble control and PODXL-KD groups, respectively. * represents $p<0.05$. **(E)** Representative immunohistochemistry sections of primary splenic tumors derived from scramble control (left) or PODXL-KD (right) Pa03c cells stained for PODXL reveal that PODXL knockdown is maintained *in vivo.*

**Figure 6**

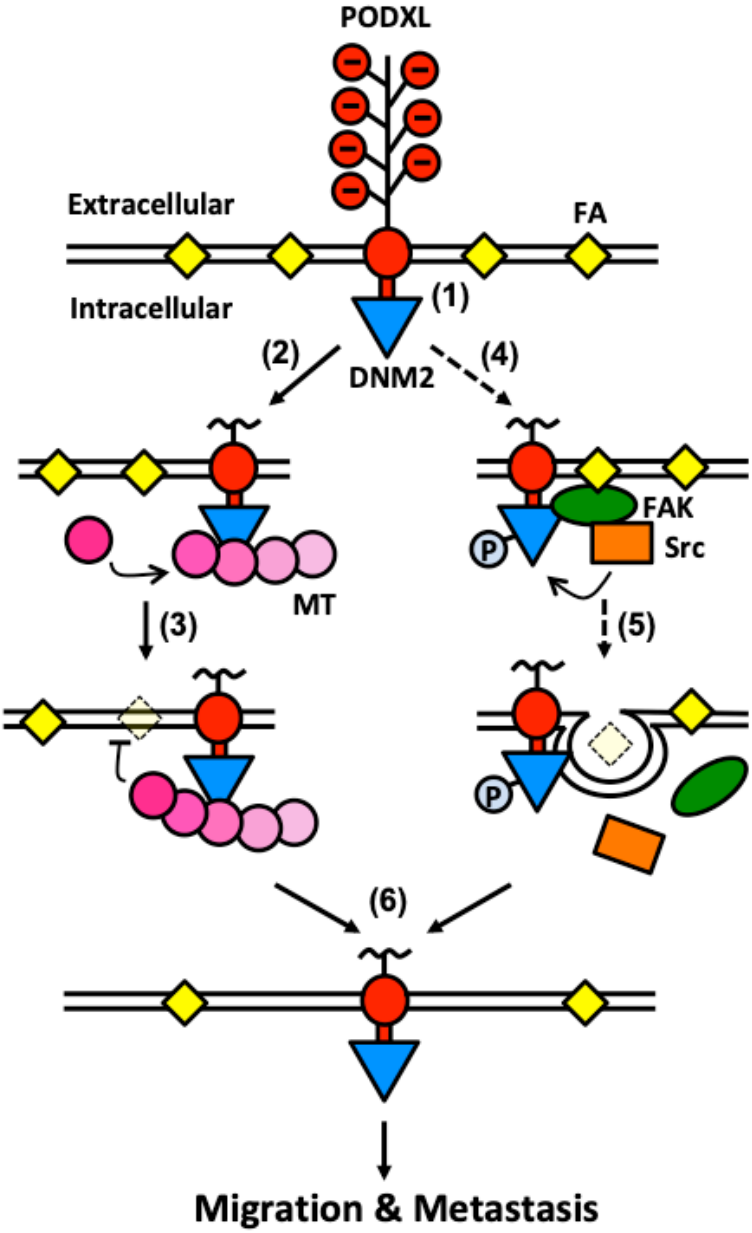
PODXL
Extracellular
FA
Intracellular
(1)
(2)
DNM2
(4)
FAK
Src
P
MT
(3)
(5)
P
(6)
Migration & Metastasis

**Figure 3.6 Proposed mechanism by which PODXL facilitates pancreatic cancer cell migration and metastasis**

(1) PODXL is a transmembrane protein expressed on pancreatic cancer cells. The cytoplasmic tail of PODXL binds to dynamin-2, thereby recruiting dynamin-2 close to the plasma membrane. (2) The local enrichment of dynamin-2 causes increased microtubule growth rates and dynamics. (3) Polymerization of microtubules towards FA sites induces FA disassembly. (4) Alternatively, dynamin-2 proximal to the membrane could also interact with FAK and Src kinase to form a trimeric complex next to FAs. (5) Src kinase then phosphorylates and activates dynamin-2, leading to endocytic internalization of integrin and FA disassembly. (6) All these events lead to the cells having less FAs, ultimately resulting in increased migration *in vitro* and enhanced metastasis *in vivo*. Dashed lines denote data from prior work while solid lines represent findings from this study.

## Supplementary Figure 1

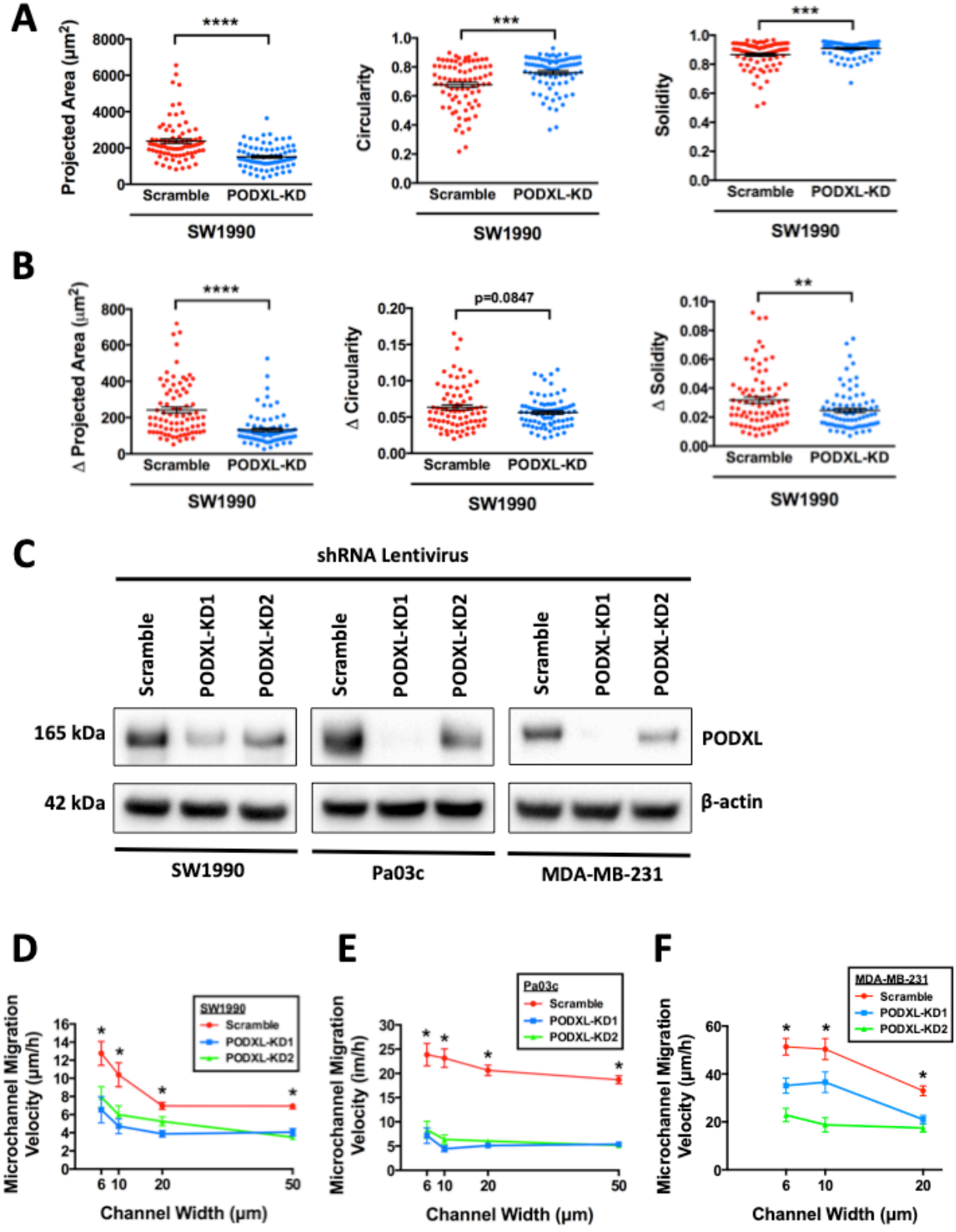

**Figure 3.S1 PODXL knockdown alters cellular morphology and diminishes morphodynamics of SW1990 cells, and decreases migration in Pa03c pancreatic and MDA-MB-231 breast cancer cells**

**(A)** Morphological parameters (projected area, circularity and solidity) of scramble control and PODXL-KD SW1990 cells migrating on 2D collagen I-coated surfaces. **(B)** Morphodynamic parameters (changes in projected area, circularity and solidity) of scramble control and PODXL-KD SW1990 cells migrating on 2D collagen I-coated surfaces. Data represent the mean±S.E.M from 3 independent experiments. ** represents $p<0.01$, *** represents $p<0.001$, **** represents $p<0.0001$. **(C)** Western blots showing efficient knockdown of PODXL in SW1990 (left panel), Pa03c (middle panel) pancreatic cancer cells, and MDA-MB-231 breast cancer cells (right panel) using shRNA lentiviruses. Migration velocity of scramble control, PODXL-KD1 and PODXL-KD2 SW1990 **(D),** Pa03c **(E)** and MDA-MB-231 cells **(F)** inside microchannels of prescribed widths. Data represent the mean±S.E.M. from 3 independent experiments. * represents $p<0.05$ between scramble control and PODXL-KD1 or PODXL-KD2. **Related to Figure 3.1**

**Supplementary Figure 2**

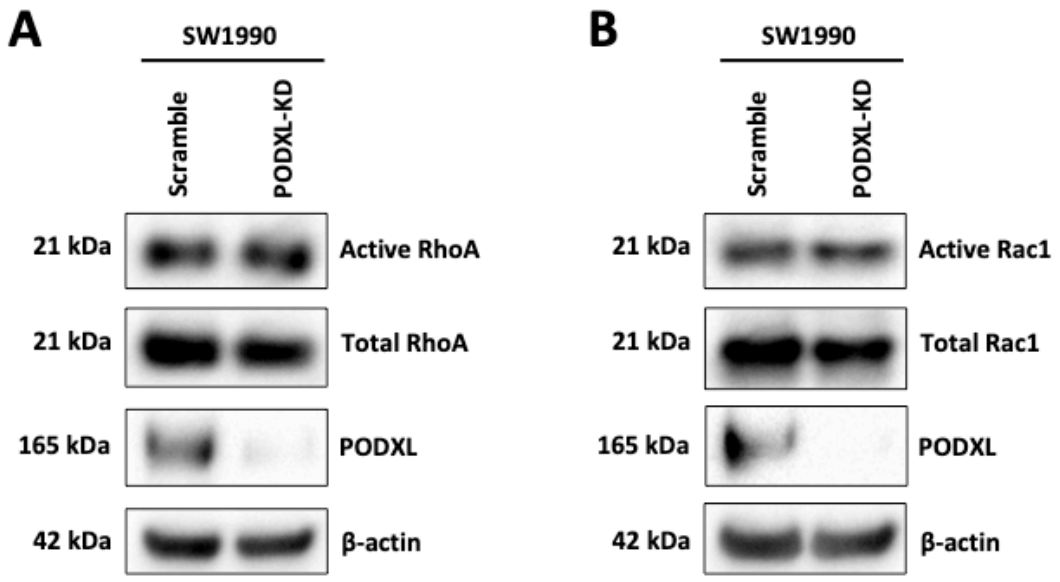


**Figure 3.S2 PODXL knockdown does not modulate RhoA/Rac1 activity**

Western blot of scramble control and PODXL-KD SW1990 specimens using pull-down activation assays for active RhoA **(A)** and active Rac1 **(B)**. PODXL silencing does not alter the levels of active RhoA or active Rac1. Total RhoA/Rac1 and β-actin served as loading controls. **Related to Figure 3.2**

## Supplementary Figure 3

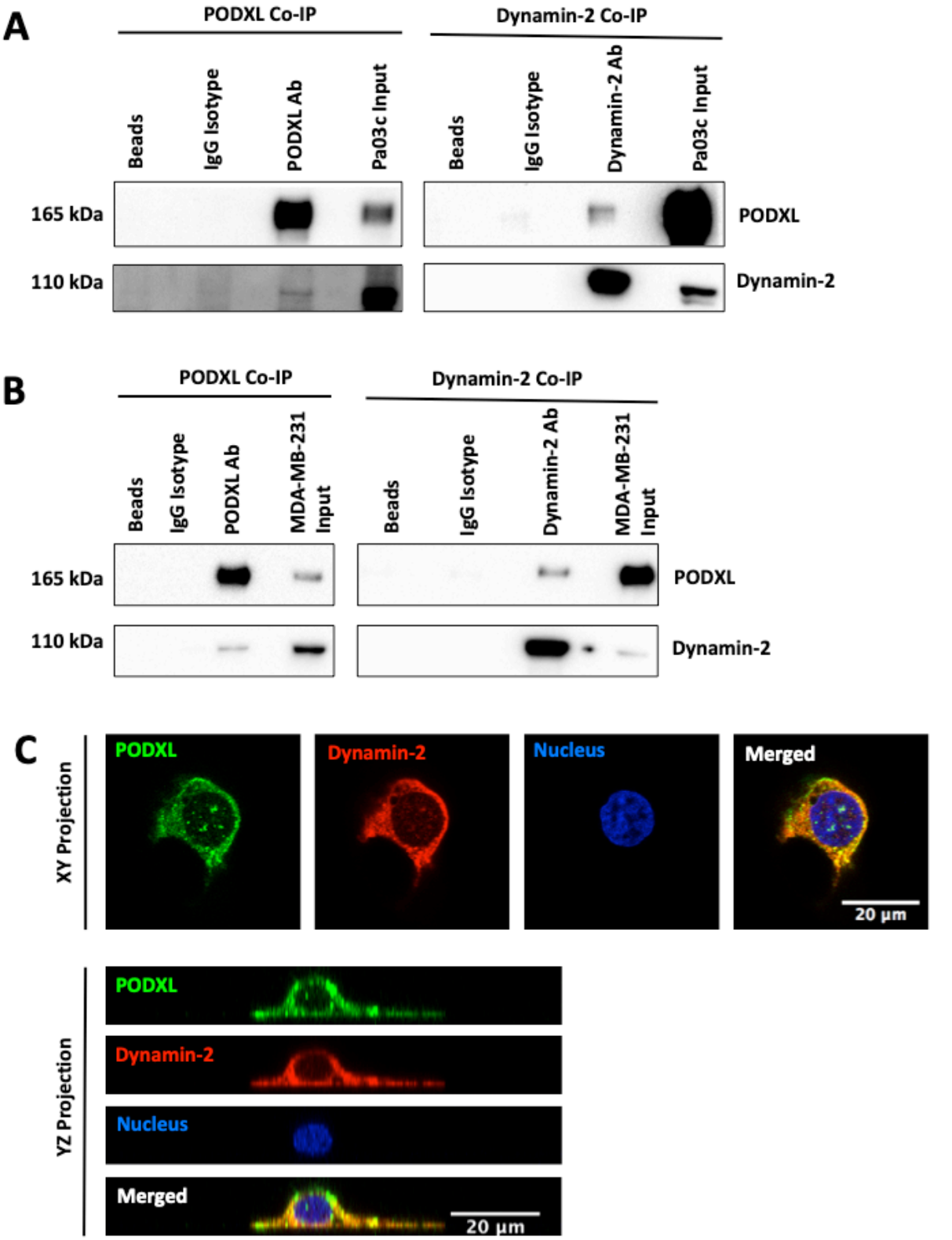

**Figure 3.S3 PODXL interacts and colocalizes with dynamin-2**

Co-immunoprecipitation experiments from Pa03c pancreatic cancer cell lysates **(A)** and MDA-MB-231 breast cancer cell lysates **(B)** were performed using either a PODXL (left panels) or a dynamin-2 (right panels) specific antibody along with match isotype controls. The resultant immunoprecipitates were subsequently resolved with SDS-PAGE and blotted with antibodies against PODXL and dynamin-2. Dynamin-2 was detected in the immunoprecipitates of PODXL and vice versa. The right lanes in both panels reveal the presence of both PODXL and dynamin-2 in Pa03c and MDA-MB-231 cell lysate inputs. The left lanes in both panels show the beads-only (no antibody) controls. **(C)** Representative immunofluorescence images of PODXL (green) and dynamin-2 (red) with a counter-stained nucleus (blue) showing colocalization of PODXL and dynamin-2 in SW1990 pancreatic cancer cells as shown in a XY (top panel) and a YZ projection (bottom panel). **Related to Figure 3.3**

## Supplementary Figure 4

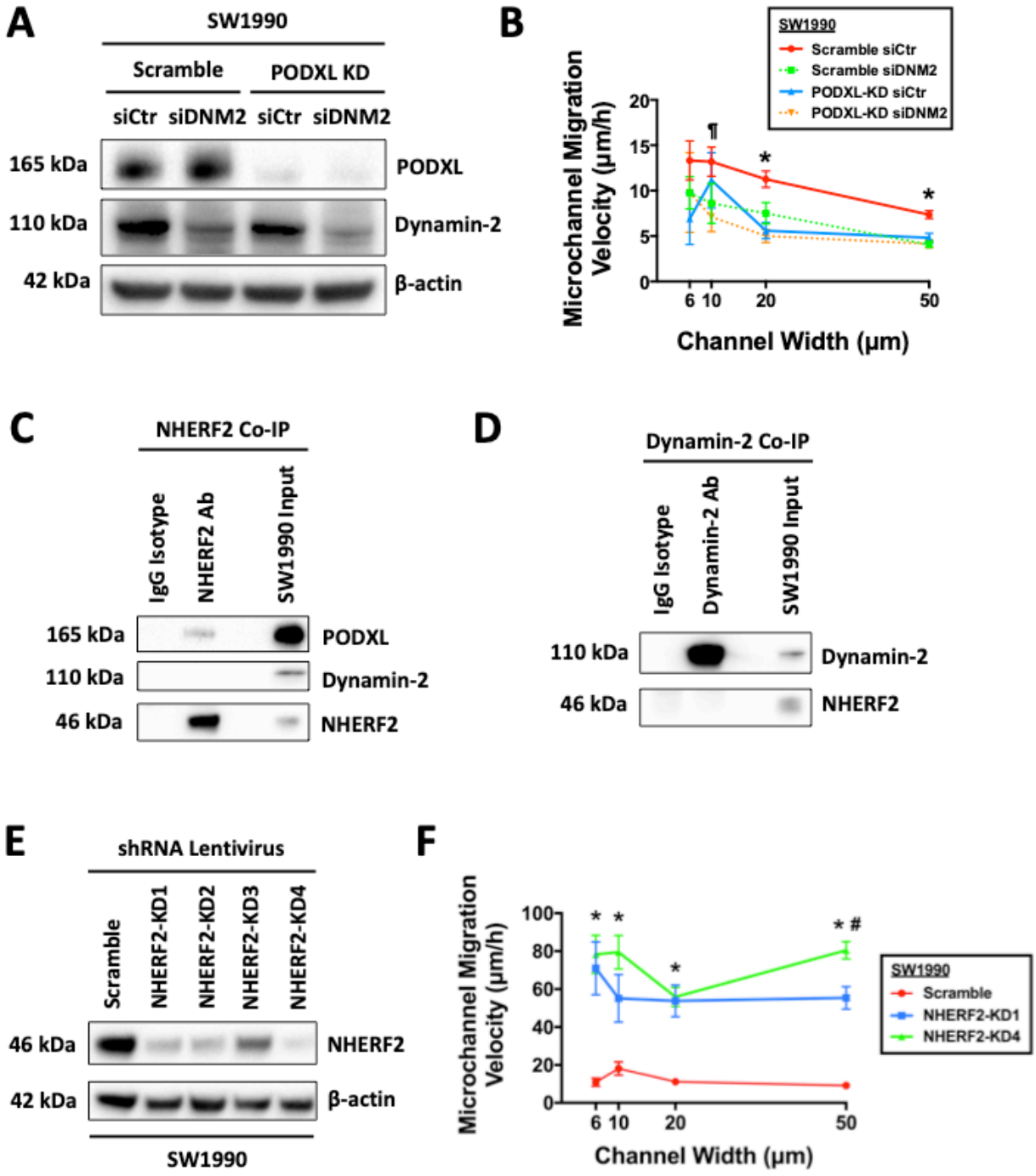

**Supplementary Figure 4 (Continued)**

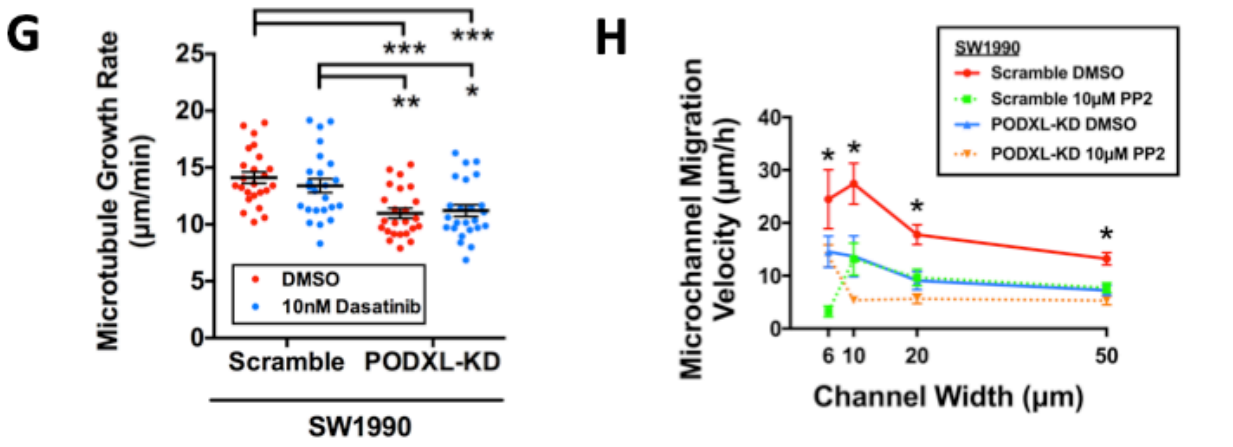


**Figure 3.S4 Effects of knocking down dynamin-2 and NHERF2, and inhibiting Src kinase on PODXL-mediated cytoskeletal changes and migration of SW1990 cells**

**(A)** Western blot showing efficient knockdown of dynamin-2 using siRNA in both scramble control and PODXL-KD SW1990 pancreatic cancer cells. **(B)** Migration velocity of scramble control and PODXL-KD SW1990 cells following dynamin-2 knockdown by siRNA treatment in microchannels of prescribed widths. Data represent the mean±S.E.M. from 3 independent experiments. * represents $p<0.05$ between scramble siCtr and all three other conditions. ¶ represents $p<0.05$ between scramble siCtr and PODXL-KD siDNM2. **(C)** Co-immunoprecipitation assays from SW1990 pancreatic cancer cell lysates were carried out using a NHERF2 specific antibody along with a match isotype control. The resultant immunoprecipitates were subsequently resolved with SDS-PAGE and blotted with antibodies against PODXL, dynamin-2 and NHERF2. NHERF2 and PODXL, but not dynamin-2, were detected in the NHERF2 immunoprecipitate fractions. The right lanes reveal the presence of PODXL, dynamin-2 and NHERF2 in SW1990 cell lysate inputs. **(D)** Co-immunoprecipitation assays from SW1990

pancreatic cancer cell lysates were carried out using a dynamin-2 specific antibody along with a match isotype control. The resultant immunoprecipitates were subsequently resolved with SDS-PAGE and blotted with antibodies against dynamin-2 and NHERF2. NHERF2 was not detected in the dynamin-2 immunoprecipitate fractions. The right lanes reveal the presence of dynamin-2 and NHERF2 in SW1990 cell lysate inputs. **(E)** Western blot showing efficient knockdown of NHERF2 in SW1990 pancreatic cancer cells using shRNA lentiviruses. NHERF2-KD1 and KD4 resulted in the highest degree of knockdown and were used in subsequent migration experiments. **(F)** Migration velocity of scramble control, NHERF2-KD1 and NHERF2-KD4 SW1990 cells in microchannels of prescribed widths. Data represent the mean±S.E.M. from 3 independent experiments. * represents $p<0.05$ between scramble control and NHERF2-KD1 or NHERF2-KD4. # represents $p<0.05$ between NHERF2-KD1 and NHERF2-KD4. **(G)** Microtubule growth rate of scramble control and PODXL-KD SW1990 cells following dasatinib (10 nM) treatment as measured by an EB1-GFP assay. Data represent the mean±S.E.M. from 3 independent experiments. * represents $p< 0.05$, ** represents $p<0.01$, *** represents $p<0.001$. **(H)** Migration velocity of scramble control and PODXL-KD SW1990 cells inside microchannels of prescribed width after PP2 (10 μM) treatment. Data represent the mean±S.E.M. from 3 independent experiments. * represents $p<0.05$ between scramble DMSO control and all three other conditions. **Related to Figure 3.4**

## Supplementary Figure 5

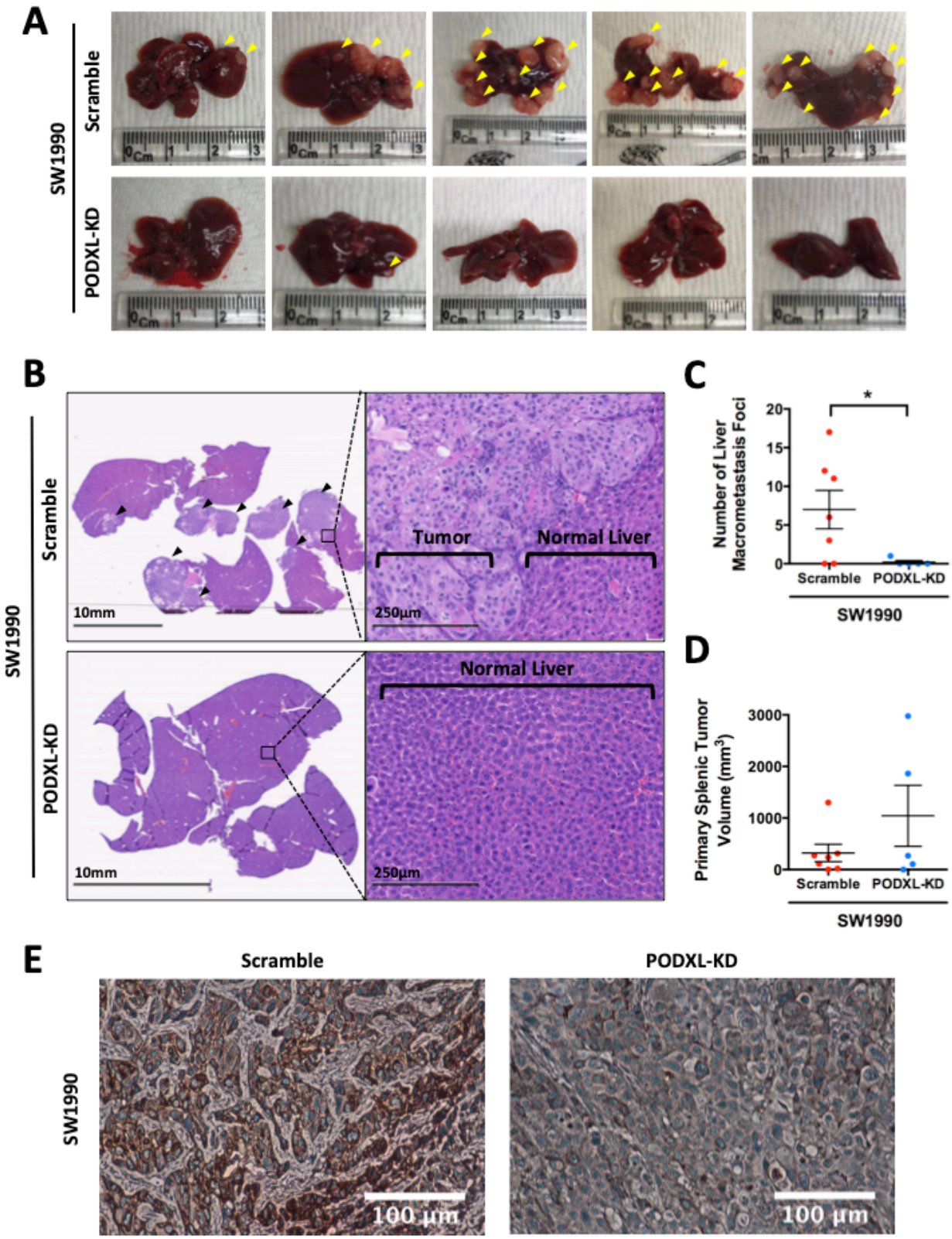

## Supplementary Figure 5 (Continued)

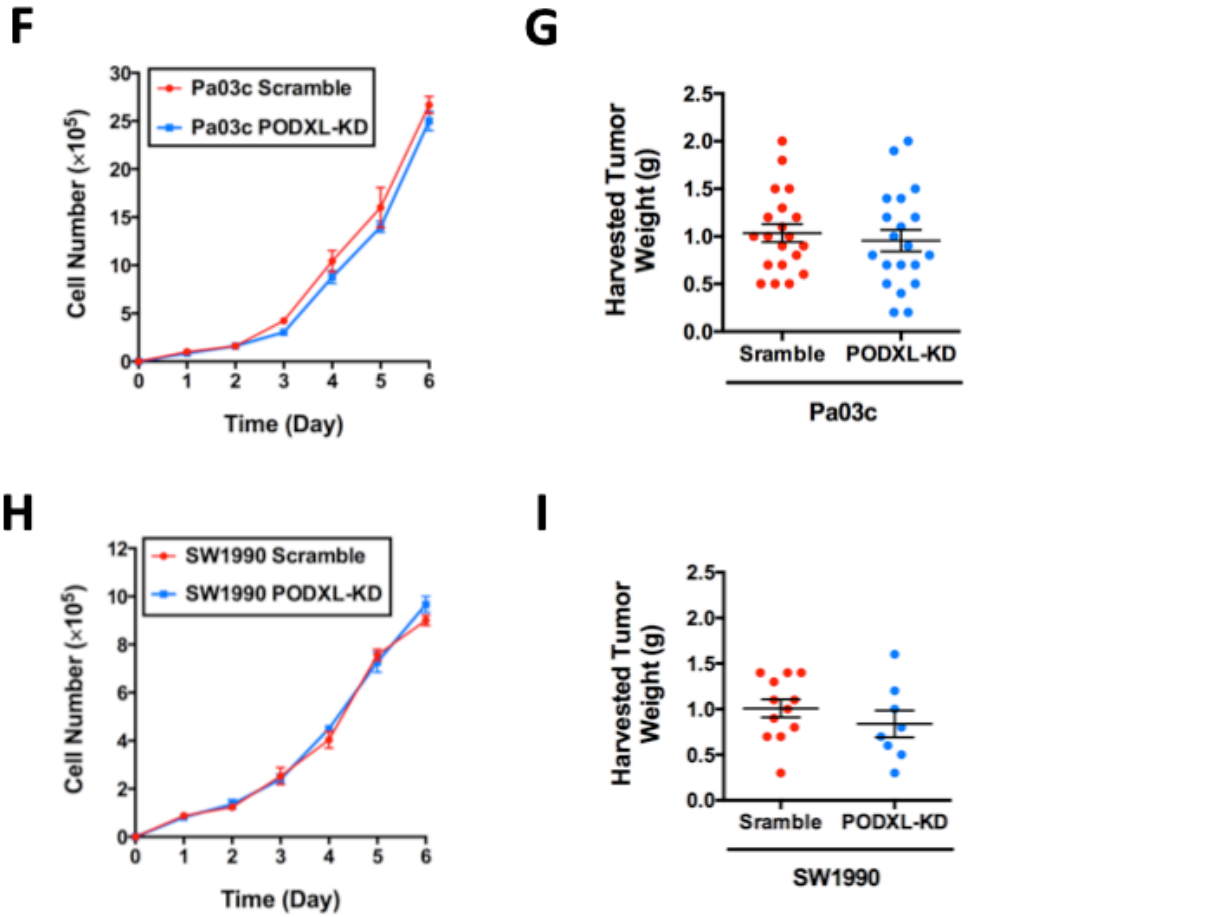

**Figure 3.S5 PODXL knockdown decreases liver metastasis *in vivo* for SW1990 pancreatic cancer cells and does not affect tumor growth *in vitro* or *in vivo***

**(A)** Gross anatomical pictures of representative livers harvested from mice injected with scramble control (top row) or PODXL-KD (bottom row) SW1990 cells via the hemispleen technique. Yellow arrowheads indicate visible liver macrometastases. **(B)** Representative histological sections of livers harvested from mice injected with scramble control (top row) and PODXL-KD (bottom row) SW1990 cells. Black arrowheads indicate areas of metastasis. **(C)** Quantification of the number of visible liver macrometastasis foci observed on the harvested livers and **(D)** the volume of the primary splenic tumor of mice injected with scramble control or PODXL-KD SW1990 cells. Data represent the mean±S.E.M from 7 and 5 mice for the scramble control and PODXL-KD groups, respectively. * represents $p<0.05$. **(E)** Representative immunohistochemistry sections of primary splenic tumor derived from scramble control (left) or PODXL-KD (right) SW1990 cells stained for PODXL showing that PODXL knockdown is maintained in vivo. *In vitro* growth curves of scramble control and PODXL-KD Pa03c **(F)** and SW1990 **(H)** pancreatic cancer cells. Data represent the mean±S.E.M. from 3 independent experiments. *In vivo* growth of scramble control and PODXL-KD Pa03c **(G)** and SW1990 **(I)** pancreatic cancer cells in a subcutaneous injection model, as assessed by the weight of tumors harvested post-mortem**.** Data represent the mean±S.E.M from 20, 20, 12 and 8 mice for scramble control Pa03c, PODXL-KD Pa03c, scramble control SW1990 and PODXL-KD SW1990, respectively. **Related to Figure 3.5**

| Identified proteins | Accession Number | MW (kDa) | Normalized Spectra Count | | | Protein functions |
|---|---|---|---|---|---|---|
| | | | Bead | Isotype | PODXL Ab | |
| Podocalyxin isoform 2 precursor | 33598950 | 55 | - | - | 3.0 | Cell adhesion, cell migration, glomerular microvillus assembly |
| Dynamin-2 isoform 5 | 299758394 | 98 | - | - | 3.0 | Endocytosis, membrane fusion, mitochondrial fission, golgi organization, G2/M transition of mitosis, apoptosis, transcription, Rac signaling, lamellipodium assembly, adhesion-dependent cell spreading, antigen processing and presentation, nitric oxide biosynthesis, synaptic vesicle transport, development of neuron, cilium, heart and sperm |
| Na+/H+ exchange regulatory cofactor NHERF2 isoform a | 194018553 | 37 | - | - | 3.0 | Protein complex assembly, cell-cell adhesion |
| Abhydrolase domain-containing protein 16A isoform a | 15100151 | 63 | - | - | 3.0 | Monoacylglycerol catabolism |
| Cytochrome P450 2S1 precursor | 13449277 | 56 | - | - | 3.0 | Redox process |
| Serine-tRNA ligase, cytoplasmic | 16306548 | 59 | - | - | 3.0 | Translation, tRNA processing, selenocysteine metabolism |
| Acyl-protein thioesterase 1 isoform 3 | 525342581 | 23 | 0.6 | - | 2.4 | Fatty acid metabolism, golgi to plasma membrane protein transport, nitric-oxide synthase activity |
| SRA stem-loop-interacting RNA-binding protein, mitochondrial isoform 1 precursor | 13654278 | 12 | - | 0.6 | 2.4 | Mitochondrial RNA catabolism, mitochondrion morphogenesis, transcription |
| RelA-associated inhibitor | 215820635 | 89 | 0.2 | 0.4 | 2.4 | Transcription, apoptosis, cell differentiation, cell-cell adhesion, p53 signal transduction, cardiac development, hair cycle |
| Cytochrome c1, heme protein, mitochondrial precursor | 21359867 | 35 | - | 0.6 | 2.4 | Energy production and conversion |
| 60S ribosomal protein L18 isoform 1 | 4506607 | 22 | - | 0.7 | 2.3 | Translation, ribosomal structure and biogenesis |
| Isoleucine-tRNA | 46852147 | 114 | - | 0.7 | 2.3 | tRNA aminoacylation, |

| | | | | | | |
|---|---|---|---|---|---|---|
| ligase, mitochondrial precursor | | | | | | translational fidelity |
| Phosphoenolpyruvate carboxykinase [GTP], mitochondrial isoform 1 precursor | 614458221 | 71 | 0.7 | - | 2.3 | Pyruvate metabolism, gluconeogenesis, insulin secretion, response to lipopolysaccharide and glucose |
| UDP-glucose 6-dehydrogenase isoform 2 | 296040443 | 48 | 0.4 | 0.3 | 2.3 | Carbohydrate metabolism, redox process, |
| Histone H4 | 77539758 | 11 | 1.0 | - | 2.0 | Nucleosome assembly, epigenetic, telomere organization, megakaryocyte differentiation, protein heterotetramerization |
| Glycine-tRNA ligase precursor | 116805340 | 83 | 0.5 | 0.5 | 2.0 | tRNA aminoacylation, diadenosine tetraphosphate synthesis |
| Ribosome maturation protein SBDS | 28416940 | 29 | 0.5 | 0.5 | 2.0 | rRNA processing, ribosome assembly, mitotic spindle organization, cell proliferation, bone development, leukocyte chemotaxis, |
| Tubulin alpha-4A chain isoform 1 | 17921989 | 50 | 0.6 | 0.8 | 1.6 | G2/M transition of mitosis, platelet degranulation, cytoskeleton organization, microtubule-based process |

**Table 3.1 Summary of results from mass spectrometry analysis of immunoprecipitate fraction generated from SW1990 pancreatic cancer cells using a PODXL specific antibody**

An isotype antibody and beads-only samples were included as additional controls to account for non-specific interactions. Immunoprecipitate fractions were submitted for mass spectrometry analysis. Proteins presented in the table were filtered to include only those that showed preferential enrichment in the PODXL antibody samples relative to the other controls (≥2X enrichment relative to the two controls). A brief description of the protein function is also included in the table. **Related to Figure 3.3**

# Chapter 4 - Predicting Progression-Free Survival and Recurrence Time of Primary Glioblastoma Using a Microfluidic Invasion Network Device (MIND)

## 4.1 Abstract

Glioblastoma (GBM) is the most aggressive form of brain cancer, characterized by high recurrence and dismal prognosis. Presently, there is no effective *in vitro* platform that can rapidly measure complex cellular phenotypic traits and accurately predict patient-specific clinical outcomes. Here, we fabricated and employed an *in vitro* testing platform, Microfluidic Invasion Network Device (MIND), and screened a panel of 22 patient-derived primary GBM specimens in a blind manner. We evaluated the ability of GBM cells to navigate and squeeze through confined microenvironments that mimic *in vivo* tight perivascular conduits and white matter tracts in the brain parenchyma, as well as the proliferative capacity of highly motile subpopulations. By combining migratory- and proliferative-based indices, MIND predicts progression-free survival ($p=0.008$) and time to recurrence ($p=0.006$) retrospectively with high sensitivity (85%), specificity (89%), and accuracy (86%). In a pilot prospective study, MIND classified all patients accurately based on their survival outcomes. Overall, our study suggests that invasive growth is intimately linked with GBM progression and patient outcomes, and reveals the translational potential of MIND for personalized GBM care.

## 4.2 Introduction

Glioblastoma (GBM) is the most common and aggressive type of primary brain cancer in adults, accounting for about 15-20% of all brain malignancies (19). Owing to its high proliferative and

infiltrative nature, the median patient survival of GBM is only approximately 14.6 months with less than 5% of patients surviving past 5 years (19,25). GBMs invade locally into the surrounding brain parenchyma and frequently spread to the contralateral hemisphere through the corpus callosum, thereby confounding local therapy and rendering gross total resection nearly impossible (23-25). As a result, despite aggressive radical surgical resection coupled with concurrent chemo- and radio- therapy, GBMs remain incurable and recur frequently (26).

To date, there is a lack of testing platforms that can effectively predict GBM outcomes in a patient-specific manner. While certain demographic (e.g. age), tumor (e.g. tumor locations, cytologic and histologic compositions) and clinical parameters (e.g. Karnofsky Performance Score) have demonstrated some prognostic values in terms of survival correlation, they are often confounded by patient comorbidities, and thus rarely affect GBM treatment decision (183,184). Recent advancements in proteomics and genomics have identified certain molecular markers, such as $O^6$-methylguanine DNA-methyltransferase (MGMT) promoter methylation and isocitrate dehydrogenase 1 (IDH1) mutation status, as independent prognostic factors for gliomas (30,41,42,185-189). MGMT promoter methylation has been shown to be associated with longer overall survival and enhanced sensitivity to therapy (43,190-192). However, inter- and intra-tumoral heterogeneity coupled with the lack of standardization and reproducibility of MGMT methylation status classification have prevented its widespread use in the clinic (193,194). IDH1 mutation status has emerged as one of the leading prognostic markers for gliomas. Specifically, low-grade glioma patients harboring the mutant form of IDH1 have improved prognosis and median survival compared to those expressing the wildtype IDH1 (195). Yet, the prognostic power of IDH1 mutation status on primary GBM remains limited as IDH1 mutations are often

associated with lower grades diffuse gliomas (Grade II and III) and with secondary GBM (46). Finally, the use of laborious and time-consuming *ex vivo* expansion of cancer cells in murine xenograft model for phenotypic testing is impractical for informing patient care given the short survival span of GBM patients (196).

Cell population-based molecular analysis techniques often overlook the inherent diversity of cancer cells and suffer from the inability to discern inter- and intra- tumoral heterogeneity that may contribute to the aggressiveness of GBM (197). While high throughput single-cell genomic and proteomic analyses could potentially ameliorate the problem of tumor heterogeneity, these techniques require sophisticated and expensive equipment and facilities, rendering their widespread application rather infeasible in most clinical settings (198,199). Importantly, the aggressiveness of cancers is frequently a result of an amalgamation of multiple distinct combinations of genetic and proteomic alterations, which cannot be predicted accurately by just one or two molecular markers and might be difficult to decipher (200). The heterogeneous and complex nature of GBM therefore necessitate the development of more direct, faster, inexpensive, high throughput and unbiased *in vitro* testing platform for GBM prognosis at single cell resolution capable of dissecting the heterogeneity among the cancer cells derived from individual patients. It is known that highly metastatic subpopulations of cancer cells have enhanced motility and proliferation rates that are linked to the aggressiveness and invasiveness of the cancer (201,202). The ability to identify a subpopulation of migratory and proliferative cells from a patient's heterogeneous tumor could therefore be the key to predicting prognosis and tailoring optimal personalized treatments for GBM patients.

With the aim to identify GBM patients with highly aggressive disease and therefore poor prognosis, we developed and fabricated a Microfluidic Invasion Network Device (MIND) that can be used to concurrently evaluate the migratory and proliferative potentials of patient-derived primary GBM cells. MIND consists of two parallel seeding and media channels connected by a series of 10 μm-high Y-shaped microchannels (99) with 20 μm-wide stem feeder channels bifurcating into either a 10 μm- or 3 μm-wide branches **(Figure 4.1.A).** These microchannels aim to recapitulate aspects of the complex topography and confining longitudinal pores or perivascular tracks of the brain parenchyma formed between glial cells and the basement membrane of vascular smooth muscle cells which ranges from 10-300 $\mu m^2$ in diameter (57). By quantifying the abundance of highly motile cells that have successfully navigated the Y-shape microchannels and the proliferative potential of these migratory subpopulations, we demonstrate that MIND can predict individual patient survival and time to recurrence with close to 90% sensitivity, specificity and accuracy in our retrospective patient cohort. Furthermore, in a pilot prospective study MIND successfully classified all patients accurately based on their survival outcomes. Overall, our study suggests that invasive spread and tumor growth are primary hallmarks of tumor aggressiveness, which can be exploited to accurately predict patient clinical outcomes.

## 4.3 Materials and methods

### 4.3.1 Cells and cell culture

Patient-derived primary human GBM cells (Retrospective: GBM153, GBM276, GBM318, GBM496, GBM499, GBM501, GBM549, GBM609, GBM612, GBM626, GBM651, GBM653, GBM692, GBM714, GBM731, GBM832, GBM897, GBM940, GBM960, GBM965, GBM1049,

GBM1298; Prospective: GBM1280, GBM1283, GBM1295, GBM1296) were isolated from primary tumor tissue samples of patients undergoing brain resection surgery for GBM at the Johns Hopkins Hospital with approval of the Institutional Review Board. All tumor samples were pathologically confirmed to be GBM. Tissue donors did not receive any treatment prior to surgery. The primary cells were isolated, purified and maintained through previously described methods that eliminate cross-contamination from other cell types and are capable of maintaining the stemness and molecular characteristics of the original primary tumors (203). The primary GBM cells were grown as adherent cultures on tissue culture flasks pre-coated with laminin (Trevigen) at a density of 1 μg/cm$^2$ surface area diluted with PBS without magnesium and calcium for 3 h at 37°C. The culture media consisted of 1:1 Dulbecco's Modified Eagle Medium/Nutrient Mixture F-12 (DMEM/F12, Invitrogen), Gem21 Neuroplex$^{TM}$ without vitamin A serum-free supplement (Gemini), 1× antibiotic/antimycotic solution (Sigma-Aldrich), 10 ng/ml of recombinant human fibroblast growth factor (Peprotech) and 20 ng/ml of recombinant human epidermal growth factor (Peprotech). Accutase solution (Sigma-Aldrich) was used to dissociate cells from the laminin-coated tissue culture flasks instead of trypsin.

### 4.3.2 Microfluidic Invasion Network Device (MIND)

MIND comprised a series of 400 μm-long and 10 μm-tall Y-shape microchannels (99), with a 20 μm-wide feeder channel bifurcating at an angle of 65° to 10 μm-wide or 3 μm-wide branches, arrayed perpendicularly between cell seeding (100 μm-wide, 50 μm-high) and media channels (400 μm-wide, 50 μm-high). There are a total of 243 Y-shape microchannels per device spaced at an interval of 50 μm from each other.

MIND was fabricated using standard multilayer photolithography and replica molding techniques (77,98). The design of the microfluidic device was created in AutoCAD (Autodesk) and transferred to chrome-on-glass darkfield photolithography masks (Photoplot Store). The primary feature of the negative silicon wafer mold, corresponding to the Y-shape microchannels, was fabricated using SU-8 3010 negative photoresist (Microchem). SU-8 3010 was spun to a thickness of 10 μm on a cleaned silicon wafer (University Wafer) with a spin-coater (Single Wafer Spin Processor, Model WS-400A-6NPP-LITE, Laurell Technologies). The film was soft baked and UV-exposed through a photomask defining the Y-shape microchannels array using an EVG620 mask aligner (EVG) at 170 mJ/cm$^2$. The exposed wafer was then baked, developed with SU-8 developer, rinsed with isopropanol and dried. To fabricate the cell and medium inlet lines, the photolithography step was repeated using a 50 μm-thick layer of SU-8 3025, with exposure through a mask defining the cells and medium feed lines aligned over primary features at 250 mJ/cm$^2$. The completed wafer was passivated by treating with (tridecafluoro-1,1,2,2,-tetrahydrooctyl)-1-trichlorosilane (Pfaltz & Bauer) overnight in a vacuum desiccator.

Completed MIND was formed using standard replica molding from the silicon wafer. PDMS elastomer and crosslinker (Sylgard® 184 Silicone Elastomer Kit, Dow Corning) were mixed at a 10:1 w/w ratio, poured over the wafer, degassed in a vacuum, and cured at 85 °C for 2 h. Solidified PDMS were peeled off of the wafer, punched with a 5 mm-diameter hole puncher at the designated well inlets and outlets and cut into appropriate sizes. The cut PDMS devices and 25 mm × 75 mm microscope slides (Electron Microscopy Sciences) were cleaned with 100% ethanol, blown dry with filtered air, and treated with oxygen plasma (Plasma Cleaner PDC-32G, Harrick Plasma) for 2 min at 18W to render the surfaces hydrophilic. The plasma treated PDMS

devices were subsequently attached and sealed to the glass slides. To enable cell binding and adhesion, each MIND device was coated with 3 μg of laminin 1 (Trevigen) diluted in PBS without magnesium and calcium at 37 °C for 1 h followed by 4 °C overnight.

### 4.3.3 MIND assay

Patient-derived primary GBM was detached from laminin-coated tissue culture flask with Accutase, counted and resuspended to a final concentration of $1 \times 10^6$ cells/ml. Prior to cell seeding, laminin coating solution was aspirated from the microchannels and the devices were washed once with PBS without magnesium and calcium. 30 μl was added to the bottom most medium inlet reservoir as backpressure to prevent the cells from prematurely traversing the Y-shape microchannels by convective flow. 50 μl of cell suspension, which is equivalent to $5 \times 10^5$ cells, was then introduced to the right cell seeding inlets and the cells were allowed to incubate at 37 °C for 5 min to allow for attachment and seeding at the entrance of the Y-shape microchannels. After 5 min, 30 μl was transferred to the left cell seeding inlets to enable cell flow and seeding from the other direction, followed by another 5 min of incubation. Afterwards, all cell suspension was removed and transferred from the right cell seeding inlets and the left cell seeding inlets, and the cells were then incubated again for another 5 min. All remaining cells in the cell inlets reservoir were then removed. 100 μl of GBM media was then introduced to each of the three medium inlet reservoirs and also the cell seeding inlets on the right side of the device. Migration of GBM in MIND was visualized and recorded via time-lapse live microscopy via software-controlled stage automation. The cells were imaged via a 10x/0.30 numerical aperture Ph1 objective lens every 20 min for 24 h using a Digital Sight Qi1Mc camera mounted on a

Nikon Inverted microscope equipped with a stage top incubator (Tokai Hit Co., Shizuoka, Japan) maintained at 37°C with 5% $CO_2$ and humidity.

The video was inspected visually and analyzed using the NIS Elements Viewer to quantify the number of highly motile and lowly motile cells. Highly motile cells are defined as cells that migrate up the feeder channels, reach the bifurcation and enter either one of the two branches. Conversely, lowly motile cells include the cell population that enter and migrate in the feeder channels but do not enter the bifurcations. Tracking for a cell ceases either after more than half of the cell body has entered the bifurcations or has exited the bottom of the feeder channels. Cells are excluded from analysis if they 1) started already more than half way in the feeder channels at the beginning of the experiment; 2) undergo cell division; 3) exited and reenter the microchannels. The % of highly motile cells was calculated as the ratio of highly motile cells over the sum of both highly motile and lowly motile cells. The number of cells that either enter the 3 μm or and 10 μm-wide branches were also recorded for the calculation of % of narrow entry, which is defined as the % of highly motile cells that enter the 3 μm narrow channels.

#### 4.3.4 Ki67 Immunofluorescence staining

Patient-derived primary GBM cells were seeded into MIND as per the protocol used for the migration study and allowed to migrate in MIND for 24 h at 37°C. Cells were fixed in 4% paraformaldehyde for 20 min, permeabilized in 1% Triton X-100 for 10 min and blocked for 2 h in blocking buffer comprising PBS without magnesium and calcium with 2% bovine serum albumin and 0.1% Triton X-100. Cells were incubated with Ki67 (8D5) mouse monoclonal antibody (Cell Signaling, 9449S, 1:800) diluted in blocking buffer at 4°C overnight, followed by

2 h incubation with Alexa Fluor 488 goat anti-mouse secondary antibody (Invitrogen, A11001, 1:200) and Hoechst 33342 (ThermoFisher Scientific, H3570, 1:2000) diluted in blocking buffer in room temperature protected from light. The cells were washed thoroughly with PBS without magnesium and calcium between each step. Imaging of the immunostained samples was performed on an inverted Eclipse Ti epifluorescence microscope (Nikon) with a 10×/0.30 numerical aperture lens. The % Ki67-positive cells was calculated for the highly motile cells (i.e. % highly motile Ki67-positive cells) and for all of the cells that enter the Y-shape microchannels (i.e. % unsorted Ki67-positive cells).

### 4.3.5 Western blot and antibodies

Standard western blot techniques were performed as previously described (159). The antibodies used are listed below. Primary antibodies: 1) IDH1 (D2H1) rabbit mouse monoclonal antibody (Cell Signaling, 8137S, 1:1000). 2) Anti-IDH1 R132H mouse monoclonal antibody (Sigma Aldrich, SAB4200548, 1:250). 3) GAPDH (14C10) rabbit monoclonal antibody (Cell Signaling, 2118S, 1:2000). Secondary antibodies: 1) Anti-mouse IgG, HRP-linked antibody (Cell Signaling, 7076S, 1:2000). 2) Anti-rabbit IgG, HRP-linked antibody (Cell Signaling, 7074S, 1:2000).

### 4.3.6 Correlation between *in vitro MIND* and clinical data

To assess the relationship between the migratory and proliferative measurements obtained with MIND to clinical patient outcome, the samples were separated into low and high survival groups based on the threshold of 14.6 month of median GBM patient survival established by *Stupp et al*. (25). Student's t-test was conducted to detect statistical difference between the MIND measurement metrics between the high versus low survival groups. Additionally, Pearson's

correlation analysis was conducted to assess the linear correlation between the MIND measurement metrics and patient survivals (in months).

### 4.3.7 Identification of optimal threshold

The thresholds of the *in vitro* MIND measurement metrics were systematically varied. For each threshold value, the % of the *in vitro* MIND measurement metric was compared against to classify the samples into either high survivors (< threshold) or low survivors ((≥threshold). MIND's prediction was then compared to the actual patient survival months which have been previously stratified into high and low survivors based on the 14.6 months median GBM patient survival established by *Stupp et al* (25), to label each prediction as true positive, true negative, false positive, or false negative (where true represents a match between MIND's prediction and actual patient survival, and positive/negative denotes low/high survivors respectively). With these classifications, the prediction performance characteristics, including sensitivity, specific, PPV, NPV and accuracy, of the MIND measurement metric at that particular threshold value was computed. This process is iterated for the entire range of each MIND measurement metric and the optimal threshold value was selected at a value that maximizes the average of all the prediction performance characteristics.

### 4.3.8 Assessment of the prognostic value of MIND measurement metrics

**T**he patient survival data was plotted as a Kaplan-Meier graph and the mean survival time in months of patients were compared between the groups separated by the optimal threshold determined. Log-Rank (Mantel Cox) test was conducted to detect statistical significance between the two survival curves. The performance characteristics, including sensitivity, specificity,

positive predictive value (PPV), negative predictive value (NPV), accuracy and area under curves of receiver operating characteristic curve, of each of the MIND measurement metric in successfully classifying patients into either low and high survivors was computed and tabulated. Additionally, the time to recurrence of the samples was compared between groups as separated by the optimal threshold. Similar Kaplan-Meier curve comparisons were also made with demographic, surgical and tumor characteristic information collected from the patients to assess the prognostic values of these other clinically available indices.

### 4.3.9 Logistic Regression

A composite MIND score that combines the individual MIND measurement metrics was computed via logistic regression, where the probability of each sample belonging to the low survival group (i.e <14.6 months) was calculated based on the predictors ($X_i$): % highly motile cells, % narrow entry and % highly motile Ki67-positive cells (**Equation 1**). Logistic regression coefficients ($b_i$) were determined in MATLAB using the glmfit function for all the retrospective cell lines (n=22) based on the high and low GBM survival stratification of 14.6 months **(Table 4.S2)**. Probability values, namely composite MIND scores, were calculated in MATLAB using the glmval function. Similar threshold identification, correlation and Kaplan-Meier curve comparison analyses as described above were repeated with the composite MIND score to evaluate its prognostic performance.

$$p = \frac{e^{(b_0 + b_1 X_1 + b_2 X_2 + b_3 X_3)}}{1 + e^{(b_0 + b_1 X_1 + b_2 X_2 + b_3 X_3)}} \qquad \textbf{(Equation 1)}$$

### 4.3.10 Statistical analysis

All data are presented as mean±S.E.M. from n≥3 independent experiments unless otherwise stated. Graphing and statistical analyses were performed with GraphPad Prism 7 (GraphPad Software). Statistical significance was determined between pairs of data with an unpaired student's t-test for continuous variables and Fisher's exact test for categorical variables. Pearson's correlation was used to assess the degree of correlation between two continuous variables. Two-tailed log-rank (Mantel-Cox) test was employed to assess the statistical difference between two Kaplan-Meier survivor curves.

## 4.4 Results

### 4.4.1 MIND distinguishes patient-derived primary GBM cells based on their migratory and proliferative potentials

To assess the capacity of MIND to predict individual GBM patient outcomes, we evaluated the migratory and proliferative potentials of patient-derived primary GBM cells. All cells that enter the feeder channels were analyzed and classified into 2 categories based on their migratory behaviors: lowly motile cells are defined as cells that migrated into the feeder channels but failed to reach and/or enter the bifurcations, while highly motile cells are defined as cells that successfully traversed the entire length of the feeder channels and entered either one of the branch channels (**Figure 4.1.A**). Using live-cell imaging, we calculated the percentage of highly motile cells that migrated in the microchannels, and the percentage of these highly motile cells that preferentially entered the narrower 3 μm-wide branches (termed as percentage of narrow entry). Aside from cell migration, cell proliferation is also an important factor that governs cancer aggressiveness and ability to colonize (204). Ki67 is a nuclear antigen that is specific to

actively proliferating cells and has been used in the clinic to evaluate cancer patient prognosis (205,206). With MIND, we have the unique ability to assess the proliferative capacities of GBMs, either for the unsorted total population or specifically for the sorted highly motile subpopulation. Actively proliferating cells would stain positive for Ki67 **(Figure 4.1.B)**. The percentages of Ki67-positive highly motile or unsorted cells were quantified.

A retrospective panel of 22 patient-derived primary GBM cells with complete clinical outcome information was tested in MIND in a blind manner to assess their % highly motile cells, % narrow entry, % highly motile Ki67-positive cells and % unsorted Ki67-positve cells. The median survival of this retrospective population was 12.2 months and consisted of 13 patients whom are classified as low survivors (<14.6 months, median=6.3 months) and 9 patients whom are classified as high survivors (>14.6 months, median=29.3 months) based on the 14.6 months of median GBM patient survival threshold established by *Stupp et al* (25) **(Figure 4.S1.A)**. A list of the demographic, tumor, surgical and clinical characteristics of the retrospective cohort is available in **Table 4.S1**. Notably, these demographic (age and gender), tumor (pre-operative tumor volume and tumor spread) and surgical attributes (number of surgical resections) all failed to predict survival of GBM patients between the two cohorts (**Figure 4.S1.B-F**).

Representative magnetic resonance imaging of the brains of GBM patients reveals that low GBM survivors typically possess a larger degree of butterfly tumor spread than high survivors (**Figure 4.1.C**), alluding to the potential roles of migration and proliferation as determinants of patient prognosis. The retrospective panel of 22 patient-derived primary GBM cells exhibited a

heterogeneous and wide range of migratory patterns and proliferative potentials as tested with MIND **(Figure 4.1.D)**.

### 4.4.2 Migratory and proliferative potentials of GBMs correlate with GBM patient survival

To begin evaluating the prognostic values of the various MIND measurement metrics, namely % highly motile cells, % narrow entry, % highly motile Ki67-positive cells and % unsorted Ki67-positive cells, we separated the retrospective patients into either low or high survival groups. Interestingly, primary GBM cells that are derived from the low survivors displayed higher migratory and proliferative potentials, as evidenced by their significantly higher % highly motile cells **(Figure 4.2.A)** and % highly motile Ki67-positive cells **(Figure 4.2.C)**. The low survival groups also exhibited a trend of higher % narrow entry **(Figure 4.2.B)**. The % of unsorted Ki67-positive cells, on the other hand, was similar between the two groups **(Figure 4.2.D)**.

Linear regression between each of the MIND measurement metrics and GBM patient survival in months revealed that % of highly motile cells, % of narrow entry and % of highly motile Ki67-positive cells were all negatively correlated with GBM patient survival (**Figure 4.2.E**). Interestingly, there was no correlation between % of unsorted Ki67-positive cells and GBM patient survival (**Figure 4.2.E**).

We next sought to determine a threshold value for each MIND measurement metric that can be used to classify the retrospective cohort into either low or high survivals based on the 14.6 months of median GBM survival threshold established by *Stupp et al* (25). The individual thresholds used to separate the patients were determined at levels that optimized the sensitivity,

specificity, PPV, NPV and accuracy of MIND to correctly categorize GBM patients into either high or low survivors **(Figure 4.S2.A-D)**. Segmenting the 22 retrospective patients based on the optimal threshold of 14% highly motile cells or 12% narrow entry achieved a significant separation of the Kaplan-Meier survival curves, with the curves corresponding to the group exceeding the threshold (high) exhibiting a significantly shorter median survival months than the group that fell below the threshold (low) (**Figure 4.2.F**). The optimal threshold % of Ki67-positive cells, either for the highly motile subpopulation (40%) or the entire unsorted population (45%), failed to achieve significant survival curve separation **(Figure 4.2.F)**.

Lastly, receiver-operating characteristic (ROC) curves and corresponding area under curve (AUC) were generated and calculated for each MIND measurement metric to quantify their ability to correctly identify patients based on their survival outcomes **(Figure 4.2.G)**. ROC curve is a graphical representation of the benefit-cost tradeoff between the true positive (i.e. sensitivity) and false positive (i.e. 1 minus specificity) of a binary classifier system as its discriminatory threshold is systematically varied. The AUC of ROC indicates the usefulness of a test, where a higher value (with a maximum of 1) corresponds to a more useful test. In addition, the sensitivity, specificity, PPV, NPV and accuracy for each MIND measurement metric at their optimal threshold were also tabulated in **Table 4.1**. In general, all of the individual MIND measurement metrics were able to achieve similar values of around 70-80% sensitivity, specificity, PPV, NPV and accuracy **(Table 4.1)**. It is noteworthy that % of unsorted Ki67-positive cells represented the most inferior discriminators as compared to the other 3 metrics as it had the lowest value of AUC of ROC **(Figure 4.2.G)**.

### 4.4.3 Combining the migratory and proliferative indices into a single composite score maximizes the prognostic performance of MIND

The % highly motile cells, % narrow entry and % highly motile Ki67-positive cells correlated to GBM patient survival but exhibited a rather suboptimal prognostic capability compared to what is considered to be clinically ideal. In order to further improve the predictive power of MIND, we combined these 3 indices into a composite MIND score (ranging from 0 to 1) using logistic regression **(Figure 4.3.A)**. A composite MIND threshold score of 0.5 was used to stratify patients into high (>0.5, n=12) and low composite MIND score groups (<0.5, n=10) **(Figure 4.S2.E)**. The differences in composite MIND score between the low and high survivors were magnified, with low survivors having a higher composite MIND score than the high survivors (**Figure 4.3.B**). The linear correlation between composite MIND score and GBM patient survival in months also improved substantially with a markedly higher $R^2$ value (**Figure 4.3.C**). This classification was able to achieve the greatest degree of Kaplan-Meier survival curves separation with the largest difference in median survival **(Figure 4.3.D).** Importantly, the sensitivity, specificity, PPV and NPV and accuracy of employing composite MIND score to correctly identify high and low survival patients markedly improved to approximately 90% **(Table 4.1)**. Finally, the AUC of ROC of the composite MIND score was also increased to 0.90 from around 0.80 for the individual MIND measurement metrics, signifying that the composite MIND score could now be considered an optimal discriminator **(Figure 4.3.E)**.

Aside from GBM patient survival, MIND measurement metrics and the composite MIND score can also be used to predict time to recurrence. GBM lines which were derived from patients with a high composite score, % narrow entry and % of highly motile Ki67-positive cells **(Figure**

**4.3.F)** had a significantly shorter time to recurrence. % highly motile cells alone also showed a trend in predicting time to recurrence though not statistically significant (p=0.09) **(Figure 4.3.F)**.

### 4.4.4 MIND predicts GBM patient survival retrospectively and prospectively with high effectiveness

The ability for each individual MIND measurement metric and the MIND composite score to categorize the 22 retrospective GBM patients into low versus high survival cohorts is summarized in a heat map **(Figure 4.4.A)**. The patient-derived primary GBM lines were arranged in order of increasing survival and color coded with a red-blue double gradient with white color set at the threshold of 14.6 months while the true red and true blue colors represent the lowest and highest survival respectively. The effectiveness of the individual MIND measurement metrics and the composite MIND score were also represented in the red-blue double gradient with white color being set as the optimal threshold previously determined (i.e. 14% migratory cells, 12% narrow entry, 40% migratory Ki67-positive cells, 0.5 composite score) and the true red and true blue color represents the highest and lowest value of each discriminators, respectively. With these heat maps, the false positive (i.e. patients who were high survivors but incorrectly predicted as low survivors) and the false negative (i.e. patients who were low survivors but incorrectly predicted as high survivors) results were identified by a mismatch in color hue to the survival heat map panel. The composite MIND score emerged as the most accurate discriminator compared to the individual MIND measurement metrics as it produced the least number of false positive and false negative predictions **(Figure 4.4.A)**. Of note, the survival prediction made by MIND is independent of the demographics, surgical, tumor and clinical attributes of the retrospective patient cohorts. There were no significant differences

in terms of age, gender, KPS score, pre-operative tumor volume, extent of resection and tumor extension when the patients are separated based on low versus high MIND measurement metrics or composite MIND score with their optimized threshold **(Figure 4.S3.A-G)**.

While IDH1 mutation status has been shown to be an independent prognostic predictor for lower grade gliomas(195), screening of the IDH1 mutation status of our retrospective patient cohort (**Figure 4.S4.A**) revealed its shortcomings in predicting the survival of patients suffering from primary GBM. Low and high survivors exhibited similar incidence of IDH1 mutation (**Figure 4.S4.B**). There was also no difference in terms of mean or median progression-free survival (**Figure 4.S4.C-D**) of GBM patients harboring wild type or mutated IDH1. With an overall accuracy of only 40% and an AUC of 0.43 (**Figure 4.S4.E, Table 4.1)**, IDH1 mutation status possessed no utility in identifying patients based on their survival outcomes. Overall, these findings demonstrate the superiority of MIND over IDH1 mutation status to accurately determine the clinical outcomes of primary GBM in our retrospective patient cohort.

To further evaluate the potential for MIND to be used in an actual clinical setting for GBM prognosis, we collected and tested in MIND specimens from patients that we followed prospectively (n=4). For this cohort, the patients were still alive at the time when the *in vitro* experiments were conducted and hence the survival outcomes were not available to the researchers. We measured the % of highly motile cells, % narrow entry, % highly motile Ki67-positive cells for these 4 prospective samples and computed the MIND composite score **(Figure 4.4.B, Table 4.2)**. Only 1 out of the 4 samples (GBM1295) displayed a composite score of >0.5 and was predicted to be a low survivor, while the other 3 samples (GBM1296, GBM1283,

GBM1280) were predicted to be high survivors. We continued to follow up with the patients over time and only 1 patient passed away at 6 months, before the 14.6 months of median GBM patient survival threshold. That patient is GBM1295, which MIND had correctly identified **(Table 4.2)**. The other 3 patients survived past 14.6 months, making them high survivors, which MIND had also correctly predicted (**Table 4.2)**. The prognostic performance of MIND for the prospective cohort is illustrated in a heat map similar to the retrospective cohort as described earlier **(Figure 4.4.A)**, where it is evident that the predicted survival outcome based on the composite MIND score matches the actual survival outcome perfectly **(Figure 4.4.C)**.

### 4.5 Discussion

Cell motility is a key process that contributes to a cancer cell's ability to disseminate and invade (69). In fact, enhanced motility of cancer cells has been widely linked with higher metastatic potential, aggressiveness of cancer and overall poor prognosis (51). As such, the migratory capacity of cancer cells has been proposed and used to correlate with patient and clinical outcomes in a wide variety of cancer types, such as breast and brain cancer cells (202,207). While previous studies have revealed that migratory behavior of GBM cells is qualitatively instructive in determining tumor aggressiveness (208), no study or method to date has defined an effective quantitative approach to predicting individual patient prognosis for GBM. Moreover, most of our knowledge of cell migration stems from 2D or 3D collagen assays that do not recapitulate the complex *in vivo* brain tissue microenvironment. *In vivo,* invasive GBMs have to navigate confining 3D perivascular tracks in brain vessels formed between glial cells and the basement membrane of vascular smooth muscle cells (54,209). Indeed, prior attempts at examining the relationship between glioma cell migration on 2D surfaces and disease

progression have failed to achieve significant predictions to clinically relevant patient features (210). Introducing complexity to the migration assays by examining the migratory behaviors of individual GBM cells on 1D nano-pattern substratum in response to platelet-derived growth factor (PDGF) stimulation enabled successful prediction of GBM location and recurrence potential in a small retrospective cohort of patients (202). However, no significant correlation to patient survival outcomes or prognosis was observed (202). Furthermore, it is unclear whether and how such parameters can independently or in conjunction with other cellular behavior(s) to quantitatively and precisely predict individual patient clinical outcomes for GBM patients.

In MIND, the microchannels were designed to recapitulate and mimic key aspects of the complex topography and confining longitudinal pores or perivascular tracks of the brain parenchyma. By examining the migratory behaviors of patient-derived primary GBM cells in response to topographical cues in the absence of any growth factor or chemoattractant stimulation, we found that the % of highly motile cells correlates remarkably well with overall progression-free survival, an unprecedented observation for any *in vitro* phenotypic-based prognostic assay for GBM. The success of this simple and easy-to-interpret analysis could be attributed to the ability of MIND to provide a more physiologically relevant confining microenvironment compared to conventional 1D or 2D migration assays. Along these lines, we have also observed significant correlation between patient survival and the % of highly motile cells that entered even more confining 3μm narrow branches (i.e. % narrow entry), indicating once again the value of subjecting the cells to migrate in a confined microenvironment and how this phenotypic trait can be exploited to determine patient outcome.

Aside from elevated motility, another key hallmark of aggressive cancer is its ability to grow and proliferate uncontrollably. Ki67 is a marker that is commonly used in the clinical setting to assess the proliferation potentials of cancer biopsies via immunohistochemistry staining and has been explored for cancer prognosis application with variable success (206,211). However, owing to the inherent heterogeneity of cancer cells, it is challenging to ascertain if migratory and non-migratory cells display different proliferative potentials and if these potential differences possess any prognostic values. With MIND, we have the unique ability to sort the bulk total cancer cell population into different subpopulations based on their motility and assess their Ki67 status independently. Notably, if we just quantify the % of Ki67+ cells for the total unsorted cell population, similar to just performing a regular Ki67 staining without the use of MIND, we fail to achieve any correlation to patient survival. In stark contrast, the % of Ki67+ cells for the highly motile cell subpopulation significantly correlated to GBM patient survival showcasing the importance of MIND as a sorting device. Interestingly, at the optimal threshold that maximized the accuracy of categorizing patients into either low or high survival groups, both % of highly motile Ki67+ and % of unsorted Ki67+ incidentally identified the same sets of patient into each group. Of note, both metrics were unable to achieve significant survival curve separation, unlike the migratory indices, suggesting proliferation alone is not sufficient for GBM prognosis despite demonstrating some promising correlation to patient survival.

While individually, migration indexes, namely % of migratory cells and % of narrow entry, and proliferative indices, such as % of highly motile Ki67+ cells, each possess certain degree of prognostic values for GBM patient prognosis, they also have their respective shortcomings and, with sensitivity, specificity and accuracy values of only around 70%, they are far from what is

considered clinically ideal. Given that all GBMs exhibit enhanced cellular proliferation, it is difficult to utilize proliferation index alone as a benchmark for determining individual patient outcomes. Similarly, in order for invasive cells to colonize after they have migrated to distant sites, they need to be able to proliferate in order to establish secondary colonies. To further improve the prognostic performance of MIND, we combined the migratory- and proliferative-based indices using logistic regression into a single composite MIND score. Remarkably, the composite MIND score emerged as the most accurate predictor compared the individual MIND measurement metrics, demonstrating the strongest correlation to patient survival, separating the survival curves to the greatest degree, and achieving sensitivity, specificity and accuracy of categorizing patients based on their survival outcomes to close to 90%. Moreover, MIND composite score predicts recurrence time successfully in our retrospective patient cohort. Recurrence of GBM following surgical resection represents the primary cause of death in patients and is intimately associated with future patient outcome (23,26). By quantifying the ability of GBMs to both migrate and proliferate, MIND is able to capture this aggressive invasive growth behavior and capitalize on this knowledge to make meaningful predictions regarding recurrence time and patient survival. Overall, these results reveal the benefits of combining multiple cellular parameters into making accurate prediction related to patient-specific outcomes and prognosis.

Our results also highlight the advantages of MIND over traditional non-molecular and molecular characterizations. Notably, demographic, tumor and surgical parameters, such as age, gender, tumor volume, tumor spread, number of surgical resections and KPS score, were all non-indicative of GBM patient survival and prognosis. MIND also outperforms IDH1 mutation

status, which is a clinically utilized independent prognosis indicator for certain subsets of glioma. Interestingly, in our retrospective patient cohort, we observed a complete lack of correlation between patient survival and IDH1 mutation status.

Our retrospective-based findings provide an impetus to test the efficacy of MIND in a prospective manner. As a proof of concept, we have collected and tested 4 samples. Out of the 4 prospective patients, only one patient passed away before the established median threshold of 14.6 months and was hence classified as a low survivor, while the other 3 patients were high survivors. Remarkably, MIND was able to predict all four patients specifically and successfully. This suggests promising potential for MIND to be tested in a larger prospective pre-clinical study.

Looking forward, MIND has the potential to be used in the clinical setting to rapidly distinguish between aggressive and less-aggressive cancers to inform patient care, management, and potential therapies that can impact the disease. During surgical resection of brain cancer, excess tumor specimen, which is generally discarded as medical waste after allocating a portion for pathological evaluation, can be used to perform MIND-related prognostic testing. Such excess specimen is frequently used by research laboratories to establish primary cell lines for future studies. MIND technology can thus enable us to examine patient-derived cells in order to quantitatively predict patient cancer aggressiveness. Moreover, MIND can serve as a platform for therapeutic screening to determine individual response and identify patient-specific effective therapies that can reduce the abundance of highly motile and proliferative cells. Given the promising performance of MIND in GBM, this functional assay may be useful for determining

patient surgical and clinical outcomes of other solid cancers, including those with increased propensity to migrate beyond tumor margins and ultimately metastasize to distal sites. MIND can also be extended for basic science applications where in depth molecular and genetic characterizations can be performed on highly motile and/or proliferative cells that can be physically isolated from the device following migration.

Overall, our study reveals that invasive growth is intimately associated with disease progression and overall patient outcomes. By quantitatively evaluating both migratory and proliferative behaviors of patient-derived primary GBM cells in a physiologically relevant confining microenvironment that mimics the natural invasive routes of native GBM cells, our *in vitro* testing platform, MIND, can precisely determine prognosis in a patient-specific manner **(Figure 4.5)**. We believe that this *in vitro* testing platform will provide a useful prognostic tool that can be translated into the clinics to improve personalized management of GBM patients.

## 4.6 Figures and tables

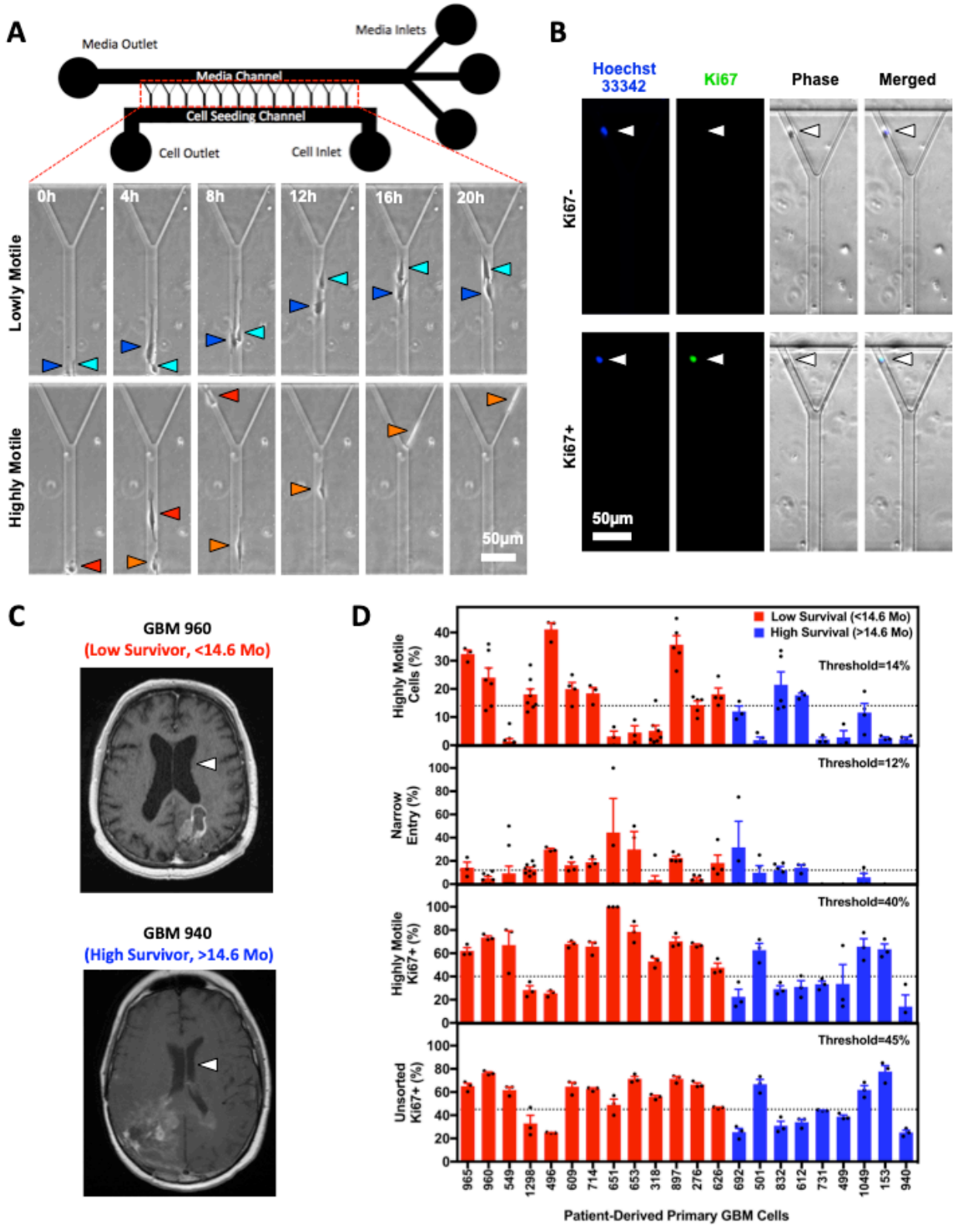

**Figure 4.1 Microfluidic Invasion Network Device (MIND) distinguishes patient-derived primary GBM cells based on their migratory and proliferative potentials**

**(A)** Schematic of MIND consisting of a series of 10 μm-tall and 400 μm-long Y-shape microchannels, with a 20 μm-wide feeder channel bifurcating to an either 10 μm- or 3 μm-wide branch. Inset: Representative time-lapse micrographs of GBM714 migrating in MIND. Lowly motile cells (top row) are defined as cells that remain in the feeder channels and fail to enter the bifurcations (blue and cyan triangles). Highly motile cells (bottom row) are defined as cells that traverse through the entire length of the feeder channel and enter either the 10 μm wide (red triangle) or 3 μm narrow branches (orange triangle). Duration between each frame is 4 h. **(B)** Representative epifluorescence images of Ki67-negative non-proliferative (top row) and Ki67-positive proliferative (bottom row) GBM965 that have migrated in MIND. The cells (white triangles) were immunostained for Ki67 (green) and counterstained for nucleus with Hoechst 33342 (blue). **(C)** Preoperative axial T1-weighted MRI with contrast showing GBM lesions of a low survivor (top panel) and a high survivor (bottom panel). White triangles represent the bilateral extension of GBM through the corpus callosum into the contralateral hemisphere known as the butterfly spread. **(D)** % highly motile cells ($1^{st}$ row), % narrow entry ($2^{nd}$ row), % highly motile Ki67-positive cells ($3^{rd}$ row) and % unsorted Ki67-positive cells ($4^{th}$ row) of a retrospective panel of 22 patient-derived primary GBM cells tested with MIND. Red bars represent cells that are derived from patients with low survival (<14.6 months, n=13). Blue bars represent cells that are derived from patients with high survival (>14.6 months, n=9). Data represent the mean±S.E.M. from n≥3 independent experiments.

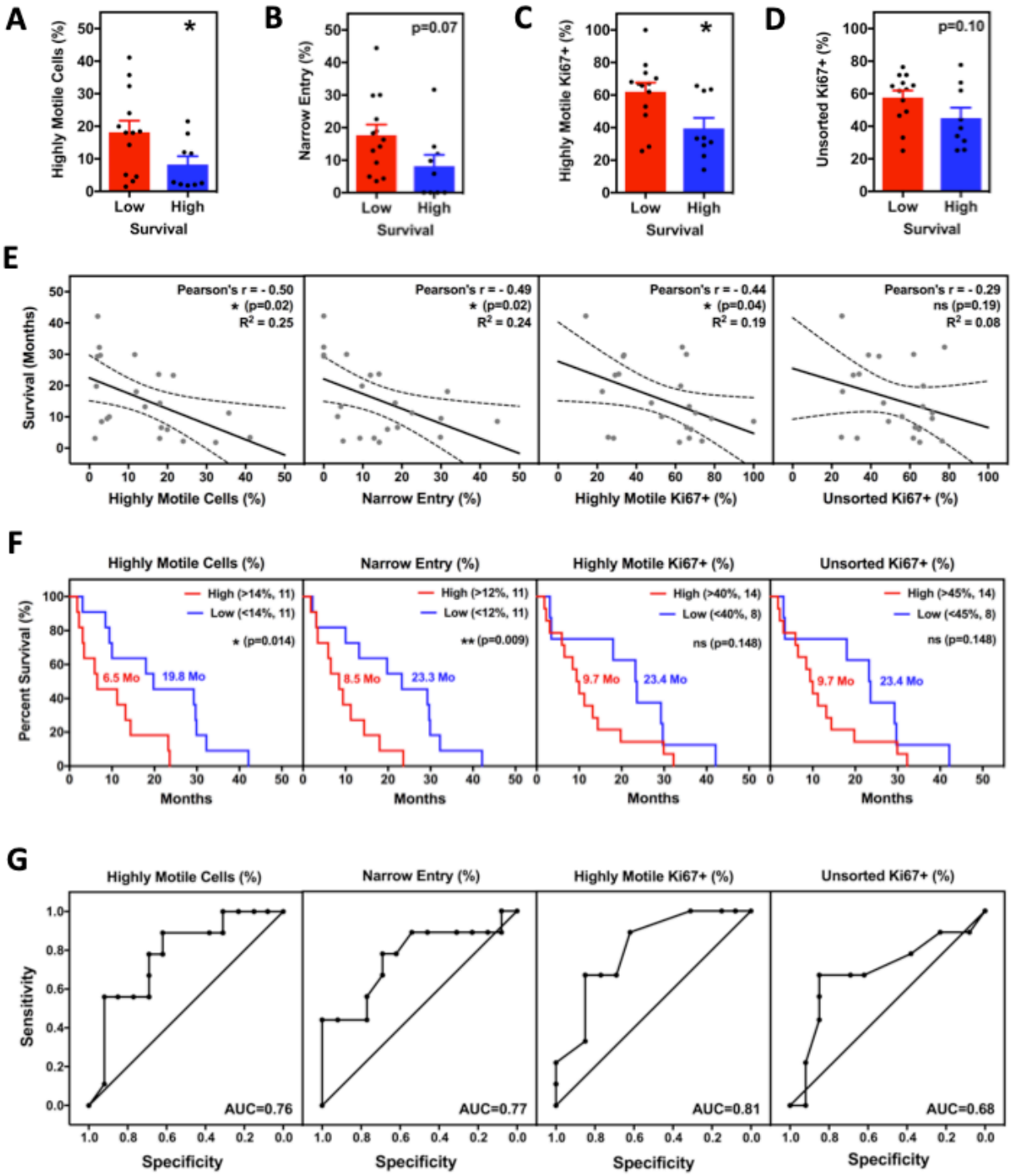
A
Highly Motile Cells (%)
*
Low
High
Survival
B
Narrow Entry (%)
p=0.07
Low
High
Survival
C
Highly Motile Ki67+ (%)
*
Low
High
Survival
D
Unsorted Ki67+ (%)
p=0.10
Low
High
Survival
E
Survival (Months)
Pearson's r = - 0.50
* (p=0.02)
R² = 0.25
Highly Motile Cells (%)
Pearson's r = - 0.49
* (p=0.02)
R² = 0.24
Narrow Entry (%)
Pearson's r = - 0.44
* (p=0.04)
R² = 0.19
Highly Motile Ki67+ (%)
Pearson's r = - 0.29
ns (p=0.19)
R² = 0.08
Unsorted Ki67+ (%)
F
Highly Motile Cells (%)
High (>14%, 11)
Low (<14%, 11)
* (p=0.014)
6.5 Mo
19.8 Mo
Narrow Entry (%)
High (>12%, 11)
Low (<12%, 11)
** (p=0.009)
8.5 Mo
23.3 Mo
Highly Motile Ki67+ (%)
High (>40%, 14)
Low (<40%, 8)
ns (p=0.148)
9.7 Mo
23.4 Mo
Unsorted Ki67+ (%)
High (>45%, 14)
Low (<45%, 8)
ns (p=0.148)
9.7 Mo
23.4 Mo
Percent Survival (%)
Months
G
Highly Motile Cells (%)
AUC=0.76
Narrow Entry (%)
AUC=0.77
Highly Motile Ki67+ (%)
AUC=0.81
Unsorted Ki67+ (%)
AUC=0.68
Sensitivity
Specificity

**Figure 4.2 Migratory and proliferative potentials of GBMs correlate with patient survival**

The retrospective GBM patient cohort is separated into low (red bars, n=13) and high survival (blue bars, n=9), and compared for their % highly motile cells **(A)**, % narrow entry **(B)**, % highly motile Ki67-positive cells **(C)** and % unsorted Ki67-positive cells **(D)**. * represents $p<0.05$ as assessed by unpaired student's t-test. **(E)** Linear regression analysis of GBM patient survival in months against % highly motile cells (1st panel), % narrow entry (2nd panel), % highly motile Ki67-positive cells (3rd panel) and % unsorted Ki67-positive cells (4th panel). Black solid line represents the best-fit line while black dotted line represents the 95% confidence interval. * represents $p<0.05$. Pearson's correlation was used to assess the significance between the variables. **(F)** Kaplan-Meier curves based on MIND measurements, comparing survival of the retrospective cohort as separated by % highly motile cells (1st panel), % narrow entry (2nd panel), % highly motile Ki67-positive cells (3rd panel) and % unsorted Ki67-positive cells (4th panel). * represents $p<0.05$, ** represents $p<0.01$ and ns represents $p>0.05$ as assessed by two-tailed log-rank (Mantel-Cox) test. **(G)** Receiver operating characteristic curves of classifying GBM patients into high or low survivors based on % highly motile cells (1st panel), % narrow entry (2nd panel), % highly motile Ki67-positive cells (3rd panel) and % unsorted Ki67-positive cells (4th panel). Area under curve (AUC) was calculated to indicate the prognostic utility of the different classifiers.

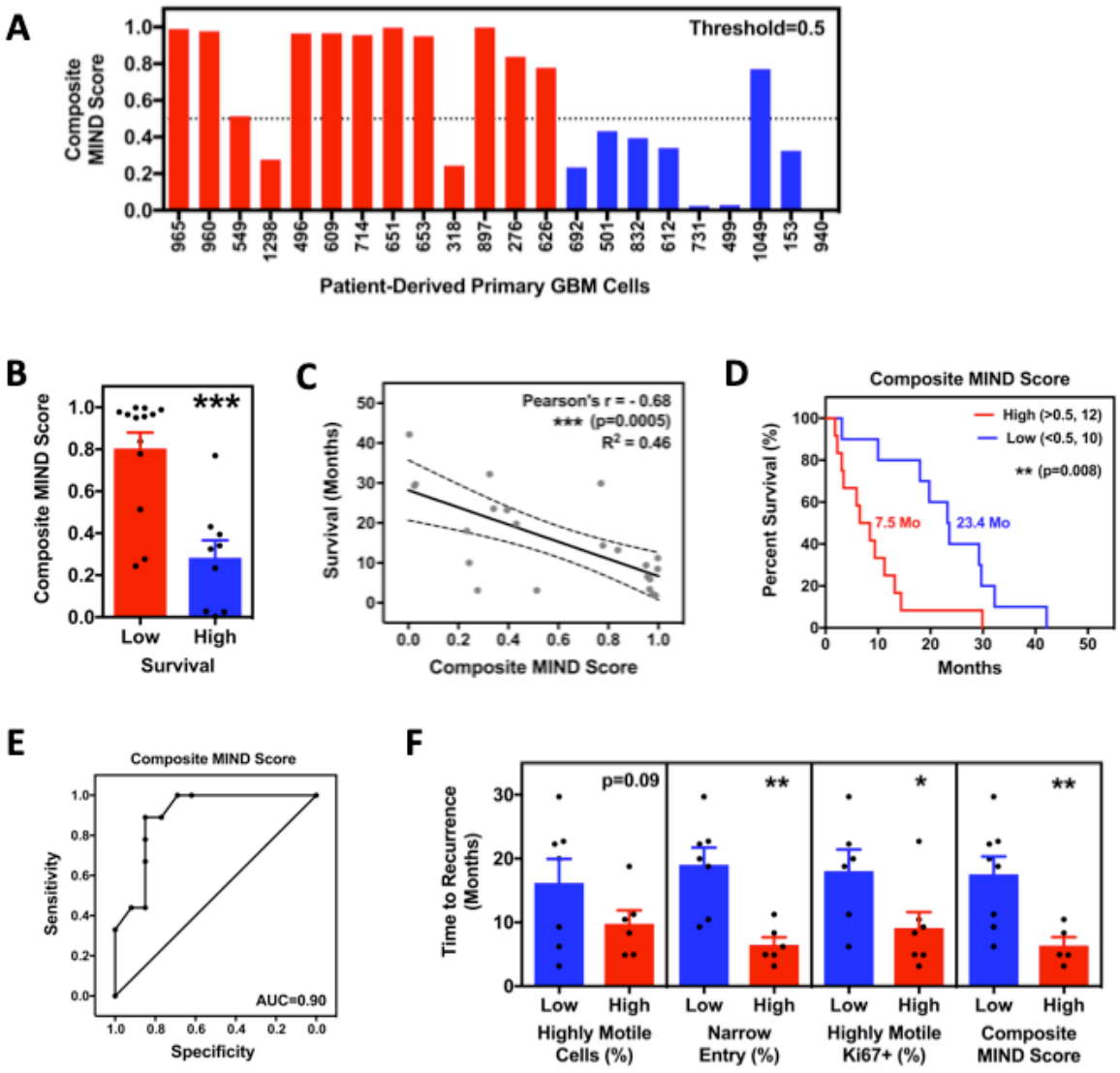
A
Threshold=0.5
Composite MIND Score
1.0
0.8
0.6
0.4
0.2
0.0
965
960
549
1298
496
609
714
651
653
318
897
276
626
692
501
832
612
731
499
1049
153
940
Patient-Derived Primary GBM Cells
B
Composite MIND Score
***
Low
High
Survival
C
Pearson's r = - 0.68
*** (p=0.0005)
R2 = 0.46
Survival (Months)
Composite MIND Score
D
Composite MIND Score
High (>0.5, 12)
Low (<0.5, 10)
** (p=0.008)
7.5 Mo
23.4 Mo
Percent Survival (%)
Months
E
Composite MIND Score
Sensitivity
AUC=0.90
Specificity
F
p=0.09
**
*
**
Time to Recurrence (Months)
Low
High
Highly Motile Cells (%)
Narrow Entry (%)
Highly Motile Ki67+ (%)
Composite MIND Score

**Figure 4.3 Combining migratory and proliferative indices into a single composite score maximize the prognosis performance of MIND**

**(A)** The values of composite MIND score computed with logistic regression by combining % highly motile cells, % narrow entry and % highly motile Ki67-positive cells as independent predictors. **(B)** Mean composite MIND score of low (red bar, n=13) versus high (blue bar, n=9) survivors. *** represents $p<0.001$ as assessed by unpaired student's t-test. **(C)** Linear regression analysis of GBM patient survival against composite MIND score. Black solid line represents the best-fit line while black dotted line represents the 95% confidence interval. *** represents $p<0.001$. Pearson's correlation was used to assess the significance between the variables. **(D)** Kaplan-Meier curve based on composite MIND score, comparing survival of the retrospective cohort as separated by high (>0.5, n=12) or low (<0.5, n=10) composite MIND score. ** represents $p<0.01$ as assessed by two-tailed log-rank (Mantel-Cox) test. **(E)** Receiver operating characteristic curve of classifying GBM patients into high or low survivors based on composite MIND score. AUC was calculated to indicate the prognostic utility of composite MIND score in classifying GBM patient into high or low survivals. **(F)** Mean time to recurrence of low versus high % highly motile cells (1st panel), % narrow entry (2nd panel), % highly motile Ki67-positive cells (3rd panel), and composite MIND score (4th panel). * represents $p<0.05$ and ** represents $p<0.01$ as assessed by unpaired student's t-test.

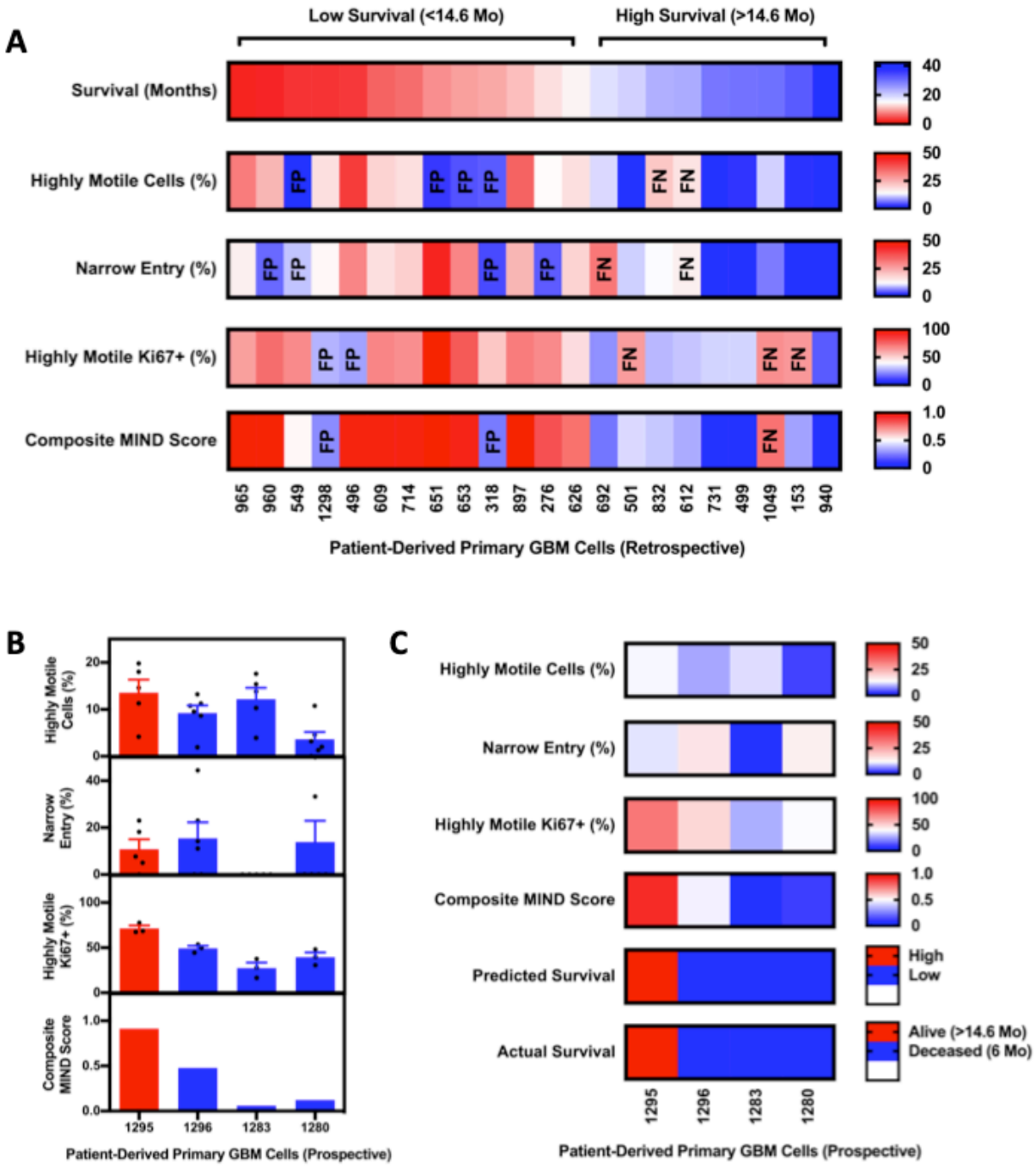
A
Low Survival (<14.6 Mo)
High Survival (>14.6 Mo)
Survival (Months)
Highly Motile Cells (%)
Narrow Entry (%)
Highly Motile Ki67+ (%)
Composite MIND Score
FP
FN
965 960 549 1298 496 609 714 651 653 318 897 276 626 692 501 832 612 731 499 1049 153 940
Patient-Derived Primary GBM Cells (Retrospective)
B
Highly Motile Cells (%)
Narrow Entry (%)
Highly Motile Ki67+ (%)
Composite MIND Score
1295 1296 1283 1280
Patient-Derived Primary GBM Cells (Prospective)
C
Highly Motile Cells (%)
Narrow Entry (%)
Highly Motile Ki67+ (%)
Composite MIND Score
Predicted Survival
Actual Survival
High
Low
Alive (>14.6 Mo)
Deceased (6 Mo)
1295 1296 1283 1280
Patient-Derived Primary GBM Cells (Prospective)

**Figure 4.4 MIND predicts GBM patient survival retrospectively and prospectively with high effectiveness**

**(A)** Heat maps summarizing the ability of individual MIND measurement metrics and composite MIND score in categorizing GBM patients into low or high survivors. The 22 GBM patients are arranged in increasing order with survival (1st panel). % highly motile cells (2nd panel), % narrow entry (3rd panel) and % highly motile Ki67-positive (4th panel) and composite MIND score (5th panel) of the 22 retrospective GBM patients as presented in a red-blue double gradient with white color set as the threshold. False positive (FP: patients who are incorrectly categorized as low survivors) and false negative (FN: patients who are incorrectly categorized as high survivors) are indicated. **(B)** % highly motile cells (1st panel), % narrow entry (2nd panel), % highly motile Ki67-positive (3rd panel) and composite MIND score (4th panel) of 4 prospective patient-derived primary GBM cells. Data represent the mean±S.E.M. from n≥3 independent experiments. **(C)** Heat maps summarizing the individual MIND measurement metrics and composite MIND score as described in (A) for the 4 prospective patients (1st to 4th panels). MIND correctly matches the predicted survival (5th panel; red=predicted to be low survivors; blue=predicted to be high survivors) to the actual survival of the 4 prospective GBM patients (6th panel; red=patient deceased before 14.6 months; blue=patient still alive after 14.6 months).

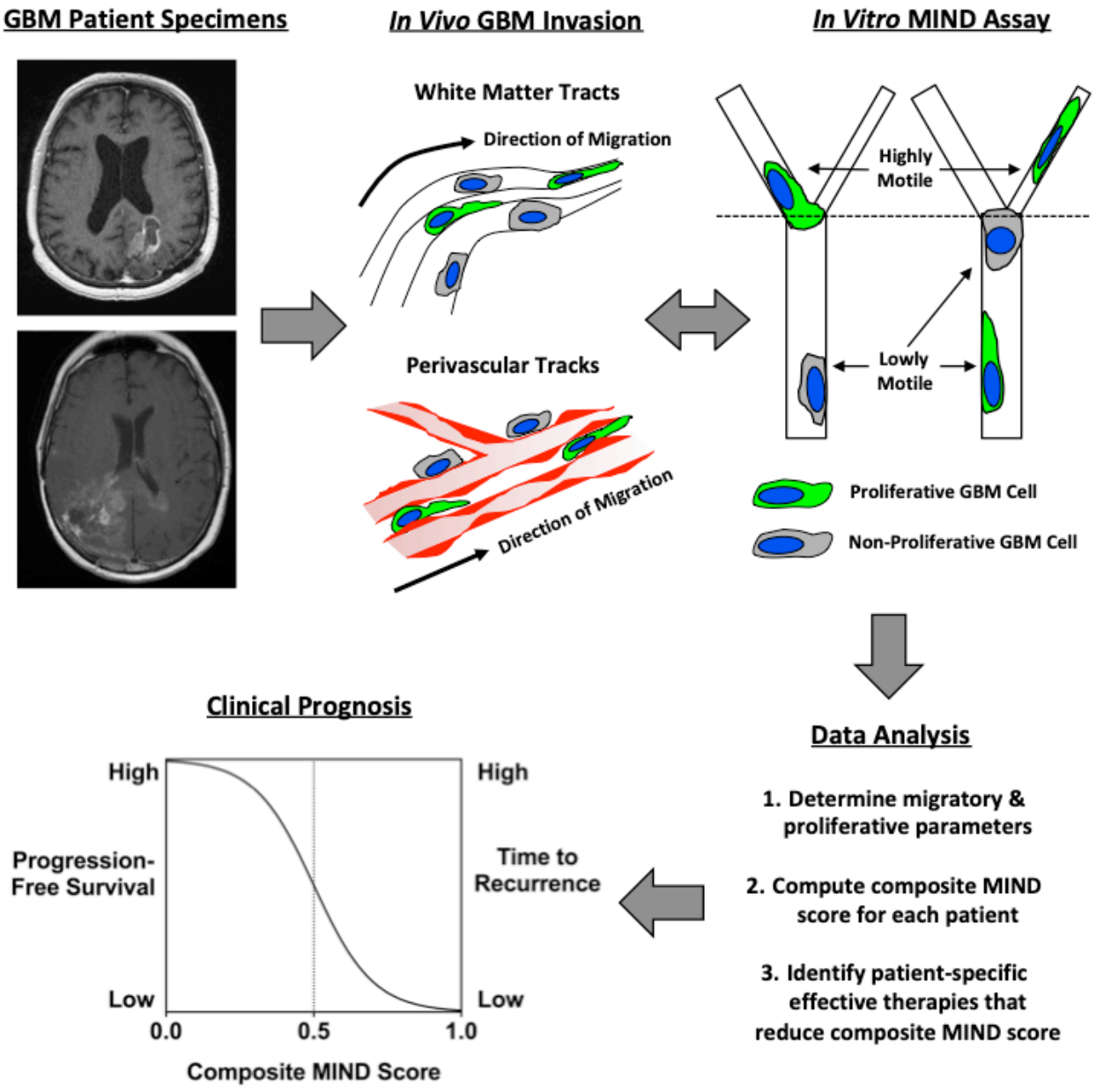
GBM Patient Specimens
In Vivo GBM Invasion
In Vitro MIND Assay
White Matter Tracts
Direction of Migration
Perivascular Tracks
Direction of Migration
Highly Motile
Lowly Motile
Proliferative GBM Cell
Non-Proliferative GBM Cell
Data Analysis
1. Determine migratory & proliferative parameters
2. Compute composite MIND score for each patient
3. Identify patient-specific effective therapies that reduce composite MIND score
Clinical Prognosis
High
Low
Progression-Free Survival
High
Low
Time to Recurrence
0.0
0.5
1.0
Composite MIND Score

**Figure 4.5 Schematic of the clinical usage of MIND**

Primary GBM specimens harvested from patient following surgical resection are allowed to migrate in MIND, which recapitulates key aspects of the complex topography and the confining microenvironment that GBM invasion occurs natively in brain parenchyma. The migratory and proliferative potentials of the patient-derived GBM cells are measured and used to compute a composite MIND score, which is then subsequently used to predict patient prognosis and identify patient-specific effective therapies. Higher composite score correlates with lower progression-free survival and lower time to recurrence.

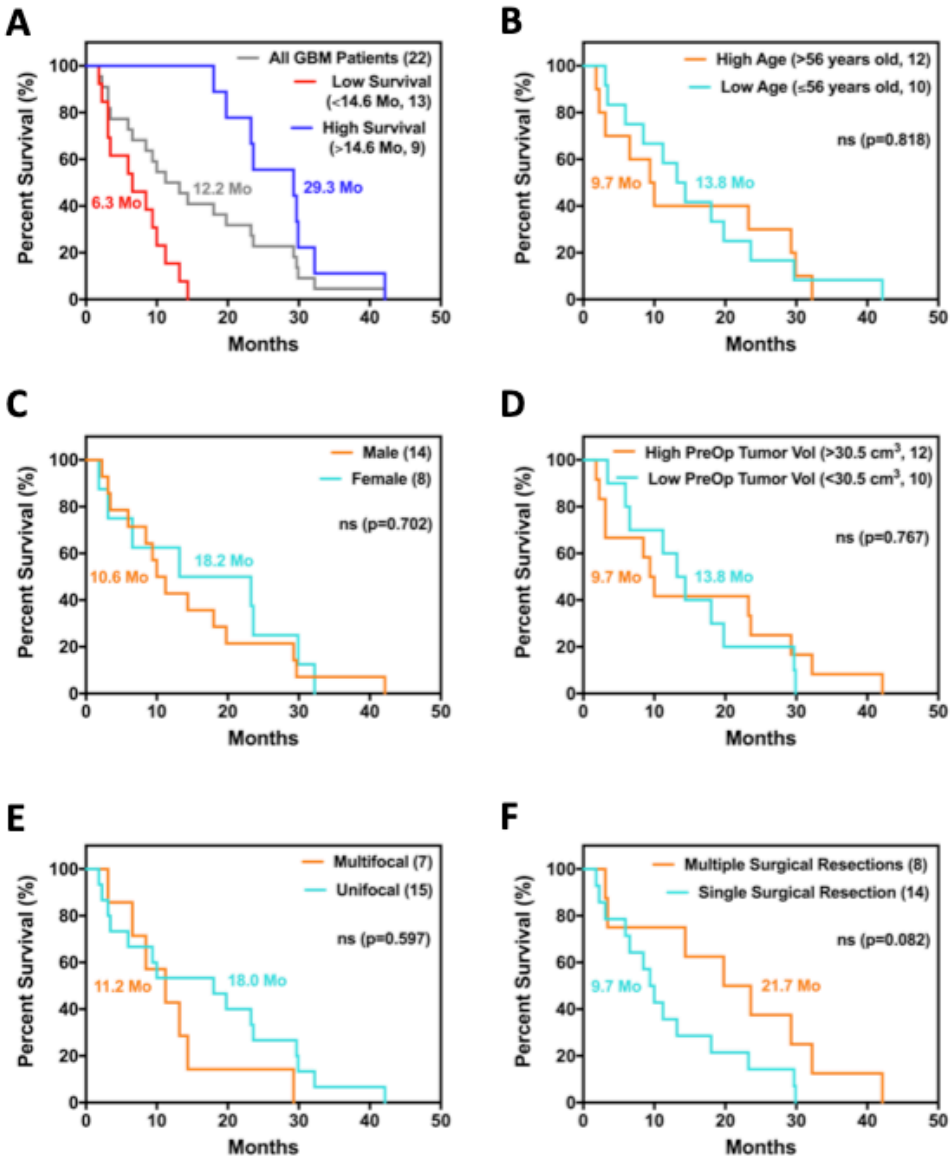
A
All GBM Patients (22)
Low Survival (<14.6 Mo, 13)
High Survival (>14.6 Mo, 9)
6.3 Mo
12.2 Mo
29.3 Mo
Percent Survival (%)
Months
B
High Age (>56 years old, 12)
Low Age (≤56 years old, 10)
ns (p=0.818)
9.7 Mo
13.8 Mo
C
Male (14)
Female (8)
ns (p=0.702)
10.6 Mo
18.2 Mo
D
High PreOp Tumor Vol (>30.5 cm3, 12)
Low PreOp Tumor Vol (<30.5 cm3, 10)
ns (p=0.767)
9.7 Mo
13.8 Mo
E
Multifocal (7)
Unifocal (15)
ns (p=0.597)
11.2 Mo
18.0 Mo
F
Multiple Surgical Resections (8)
Single Surgical Resection (14)
ns (p=0.082)
9.7 Mo
21.7 Mo

**Figure 4.S1 Demographic, tumor and surgical attributes do not correlate with GBM patient survival**

**(A)** Kaplan-Meier curve based on the 14.6 months median survival for GBM patients as established by Stupp *et al*, comparing survival between low (<14.6 months, n=13, red line) and high survivors (>14.6 months, n=9, blue line). Grey line indicates the survival curve of all of the 22 GBM patients. **(B-F)** Kaplan-Meier curve based on demographic, tumor and surgical data of GBM patients, comparing survival of cohorts as divided by median age **(B)**, gender **(C),** median pre-operation tumor volume **(D)**, tumor spread **(E)** and number of surgical resections **(F)**. All of these attributes fail to separate the population significantly ($p>0.05$) as assessed by two-tailed log-rank (Mantel-Cox) test.

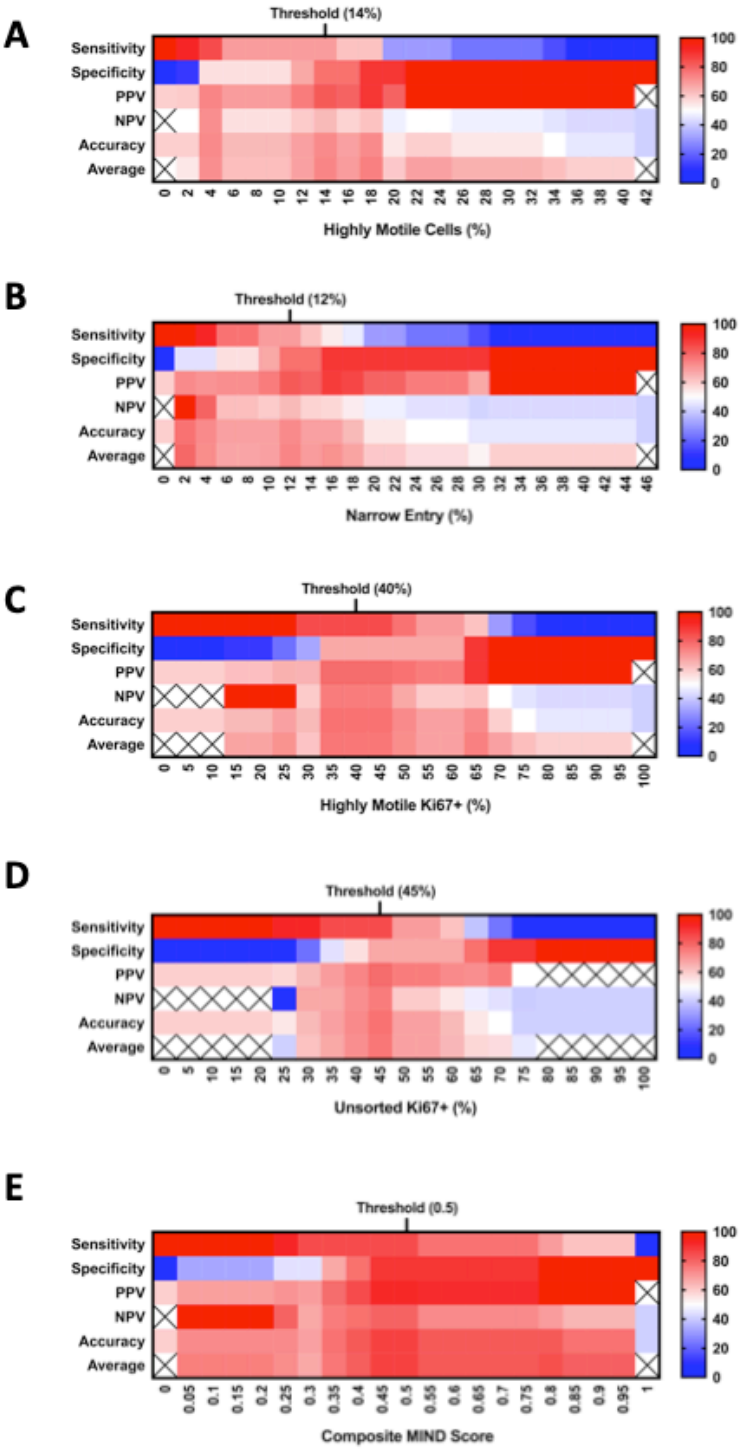
A
Threshold (14%)
Sensitivity
Specificity
PPV
NPV
Accuracy
Average
0 2 4 6 8 10 12 14 16 18 20 22 24 26 28 30 32 34 36 38 40 42
Highly Motile Cells (%)
100 80 60 40 20 0
B
Threshold (12%)
Sensitivity
Specificity
PPV
NPV
Accuracy
Average
0 2 4 6 8 10 12 14 16 18 20 22 24 26 28 30 32 34 36 38 40 42 44 46
Narrow Entry (%)
100 80 60 40 20 0
C
Threshold (40%)
Sensitivity
Specificity
PPV
NPV
Accuracy
Average
0 5 10 15 20 25 30 35 40 45 50 55 60 65 70 75 80 85 90 95 100
Highly Motile Ki67+ (%)
100 80 60 40 20 0
D
Threshold (45%)
Sensitivity
Specificity
PPV
NPV
Accuracy
Average
0 5 10 15 20 25 30 35 40 45 50 55 60 65 70 75 80 85 90 95 100
Unsorted Ki67+ (%)
100 80 60 40 20 0
E
Threshold (0.5)
Sensitivity
Specificity
PPV
NPV
Accuracy
Average
0 0.05 0.1 0.15 0.2 0.25 0.3 0.35 0.4 0.45 0.5 0.55 0.6 0.65 0.7 0.75 0.8 0.85 0.9 0.95 1
Composite MIND Score
100 80 60 40 20 0

**Figure 4.S2 Determination of threshold value for each MIND measurement metric and composite MIND score as predictors for GBM patient survival**

**(A-D)** Heat maps as presented in a red-blue double gradient (blue=minimum 0%, red=maximum 100%, white=base line 50%) indicating the values of sensitivity, specificity, positive predictive value (PPV), negative predictive value (NPV), accuracy and average of the above-mentioned five parameters of correctly categorizing the GBM patients into either high or low survivors as one varies the threshold of % highly motile cells **(A)**, % narrow entry **(B)**, % highly motile Ki67-positive cells **(C)**, % unsorted Ki67-positive cells **(D)**, and composite MIND score **(E)**. An optimal threshold value was determined that maximizes the each of 5 measures of performance. Crossed square represents the inability to compute a numerical value at that particular threshold value.

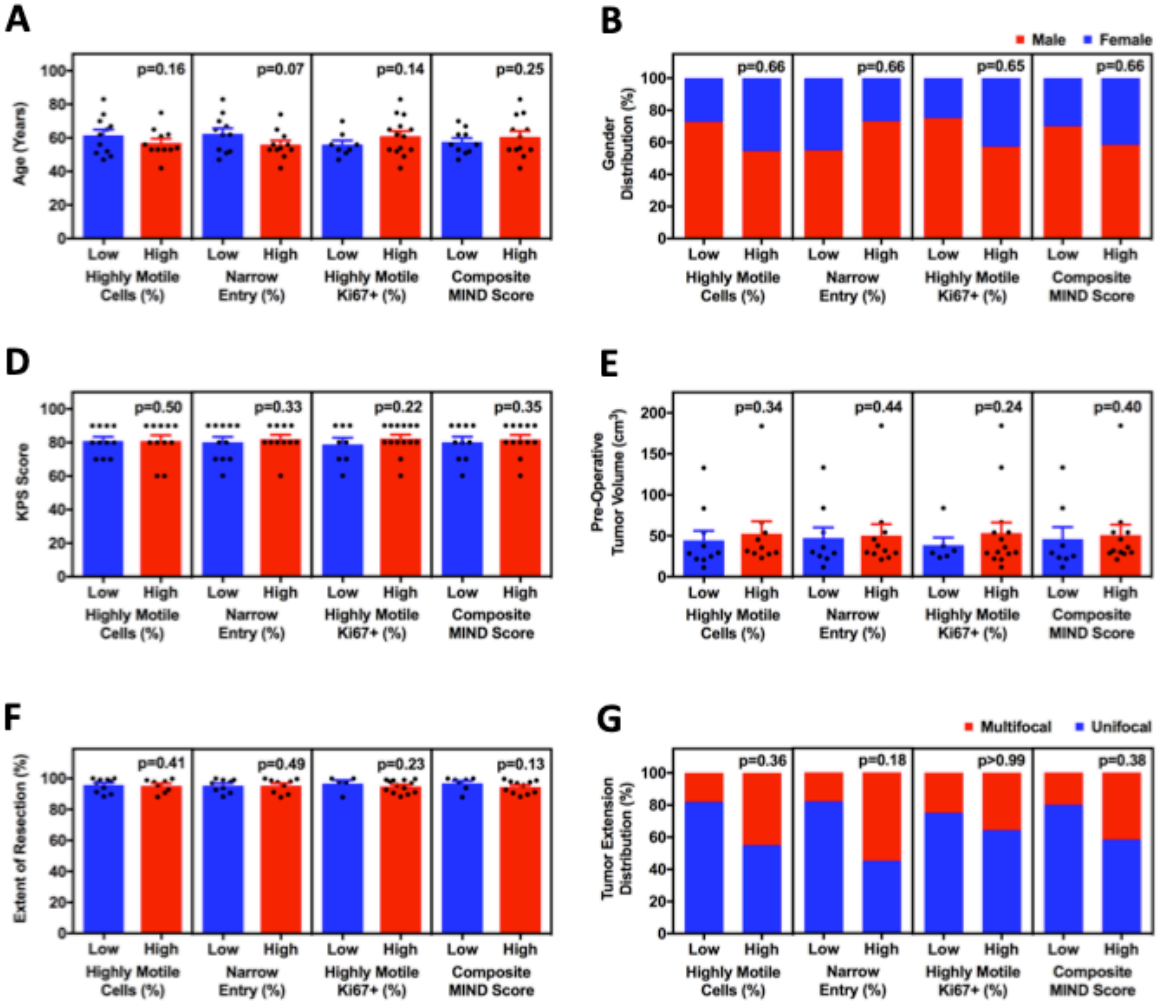
A
Age (Years)
p=0.16
p=0.07
p=0.14
p=0.25
B
Male
Female
Gender Distribution (%)
p=0.66
p=0.66
p=0.65
p=0.66
D
KPS Score
p=0.50
p=0.33
p=0.22
p=0.35
E
Pre-Operative Tumor Volume (cm³)
p=0.34
p=0.44
p=0.24
p=0.40
F
Extent of Resection (%)
p=0.41
p=0.49
p=0.23
p=0.13
G
Multifocal
Unifocal
Tumor Extension Distribution (%)
p=0.36
p=0.18
p>0.99
p=0.38
Low
High
Highly Motile Cells (%)
Narrow Entry (%)
Highly Motile Ki67+ (%)
Composite MIND Score

**Figure 4.S3 MIND does not discriminate against the demographic, surgical, tumor and clinical attributes of GBM patients**

**(A-G)** The retrospective GBM patients cohort is separated into low and high groups based on the threshold of % highly motile cells (1st panel), % narrow entry (2nd panel), % highly motile Ki67-positive (3rd panel) or composite MIND score (4th panel) and compared for their mean age **(A)**, gender **(B)**, Karnofsky Performance Status (KPS) score **(C)**, pre-operative tumor volume **(D)**, extent of resection **(E)** and tumor extension (multifocal versus unifocal) **(F)**. Significance between the low versus high groups for each classifier were assessed using an unpaired student's t-test for the continuous variables and Fisher's exact test for the categorical variables.

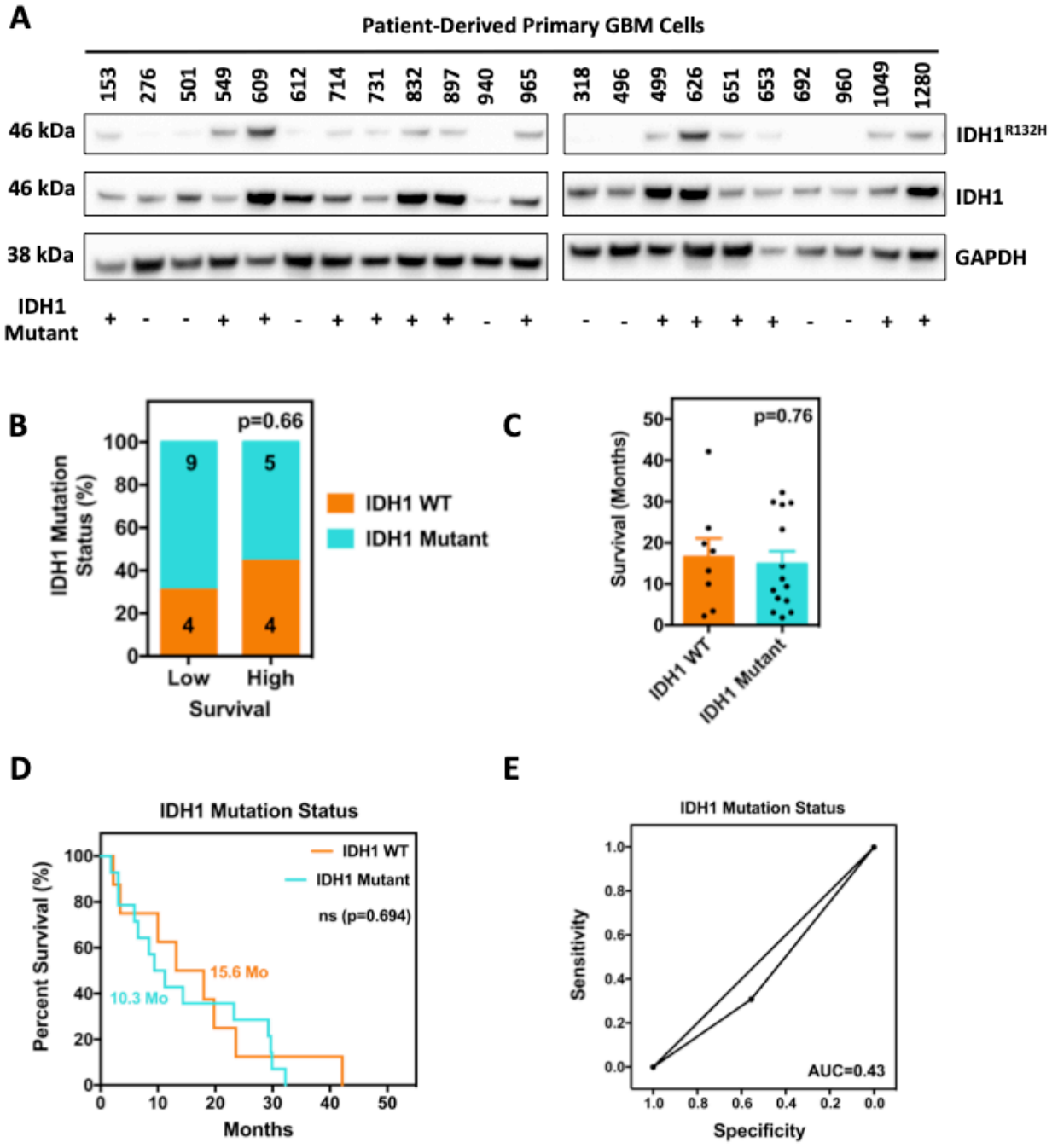
A
Patient-Derived Primary GBM Cells
153 276 501 549 609 612 714 731 832 897 940 965 318 496 499 626 651 653 692 960 1049 1280
46 kDa
46 kDa
38 kDa
IDH1 Mutant
+ - - + + - + + + + - + - - + + + + - - + +
IDH1R132H
IDH1
GAPDH
B
p=0.66
IDH1 Mutation Status (%)
9
5
4
4
Low
High
Survival
IDH1 WT
IDH1 Mutant
C
p=0.76
Survival (Months)
IDH1 WT
IDH1 Mutant
D
IDH1 Mutation Status
Percent Survival (%)
IDH1 WT
IDH1 Mutant
ns (p=0.694)
15.6 Mo
10.3 Mo
Months
E
IDH1 Mutation Status
Sensitivity
AUC=0.43
Specificity

**Figure 4.S4 IDH1 mutation status does not predict GBM patient survival**

**(A)** Western blot panels of primary GBM cells derived from the retrospective patient cohort for the mutant form of IDH1 ($IDH1^{R132H}$, top panel), total IDH1 (middle panel) and GAPDH (bottom panel) as housekeeping and loading control. The patients are classified as IDH1 mutant or IDH1 wild type (WT) based on the presence or absence of $IDH1^{R132H}$ bands. **(B)** Percentage of patients exhibiting either IDH1 WT or mutant of low versus high survivors. Statistical significance was assessed by unpaired student's t-test. **(C)** Mean GBM patient survival in months of patients exhibiting IDH1 WT or mutant. Statistical significance was assessed by unpaired student's t-test **(D)** Kaplan-Meier curve based on IDH1 mutation status, comparing survival of the retrospective cohort as grouped into IDH1 WT (n=8) or IDH1 mutant (n=14). ns represents $p>0.05$ as assessed by two-tailed log-rank (Mantel-Cox) test. **(E)** Receiver operating characteristic curve of classifying GBM patients into high or low survivors based on IDH1 mutation status. AUC was calculated to indicate the prognostic utility of IDH1 mutation status in classifying GBM patient into high or low survivals.

| | Sensitivity (%) | Specificity (%) | PPV (%) | NPV (%) | Accuracy (%) | AUC |
|---|---|---|---|---|---|---|
| **Highly Motile Cells (%)** | 69.2 | 77.8 | 81.8 | 63.6 | 72.7 | 0.76 |
| **Narrow Entry (%)** | 69.2 | 77.8 | 81.8 | 63.6 | 72.7 | 0.76 |
| **Highly Motile Ki67+ (%)** | 84.6 | 66.7 | 78.6 | 75.0 | 77.3 | 0.81 |
| **Unsorted Ki67+ (%)** | 84.6 | 66.7 | 78.6 | 75.0 | 77.3 | 0.68 |
| **IDH1 Mutation Status** | 30.8 | 55.6 | 50.0 | 35.7 | 40.9 | 0.43 |
| **Composite MIND Score** | 84.6 | 88.9 | 91.7 | 80.0 | 86.4 | 0.90 |

**Table 4.1 Measures of performance for individual MIND measurement metrics and composite MIND score in classifying the retrospective GBM patient cohort into either high or low survivors**

A positive event is defined as low survival (<14.6 months) while a negative event is defined as high survival (>14.6 months). Sensitivity is defined as the probability of correctly identifying a low survival patient from all of the low survival patients. Specificity is defined as the probability of correctly identifying a high survival patient from all of the high survival patients. Positive predictive value (PPV) is defined as the proportion of patients who are predicted to be low survival that are truly the low survivors. Negative predictive value (NPV) is defined as the proportion of patients who are predicted to be high survival that are truly the high survivors. Accuracy is defined as the probability of correctly identifying both the low and high survivors from the entire population. Area under curve (AUC) is defined as the area under the receiver operating characteristic curve (ranges from 0 to 1). AUC measures how capable each classifier is able to distinguish and separate the high from the low GBM survival groups.

| GBM | Highly Motile Cells (%) | Narrow Entry (%) | Highly Motile Ki67+ (%) | Composite MIND Score | Predicted Survival | Actual Survival | Prediction |
|---|---|---|---|---|---|---|---|
| **1295** | 13.6 ± 2.8 | 10.8 ± 4.3 | 71.3 ± 3.3 | 0.91 | Low | Deceased (6 Mo) | Correct |
| **1296** | 9.2 ± 1.6 | 15.5 ± 6.8 | 49.4 ± 2.7 | 0.48 | High | Alive (>14.6 Mo) | Correct |
| **1283** | 12.2 ± 2.4 | 0 | 27.4 ± 6.0 | 0.06 | High | Alive (>14.6 Mo) | Correct |
| **1280** | 3.6 ± 1.6 | 13.9 ± 9.0 | 39.6 ± 5.1 | 0.12 | High | Alive (>14.6 Mo) | Correct |

**Table 4.2 Individual MIND measurement metrics, composite MIND score and survival outcomes for the prospective GBM patient cohort**

| Patient Cohort | n | 22 |
|---|---|---|
| **Age at Diagnosis** | Range (Years) | 42 - 83 |
| | Median (Years) | 56 |
| **Gender** | Male (n, %) | 14, 63.6 |
| | Female (n, %) | 8, 36.4 |
| **Surgery Performed** | Yes (n, %) | 22, 100 |
| | No (n, %) | 0, 0 |
| **Resections** | Single (n, %) | 14, 63.6 |
| | Multiple (n, %) | 8, 36.4 |
| **Radiation Therapy** | Yes (n, %) | 20, 90.9 |
| | No (n, %) | 1, 4.5 |
| **KPS Scale** | Average | 80.9 |
| **Tumor Location** | Frontal (n, %) | 4, 18.2 |
| | Temporal (n, %) | 9, 41.0 |
| | Parietal (n, %) | 1, 4.5 |
| | Occipital (n, %) | 3, 13.6 |
| | Other (n, %) | 5, 22.7 |
| **Tumor Volume** | Median ($cm^2$) | 30.51 |
| **Survival** | Median (Months) | 12.2 |
| | Low, < 14.6 Months (n, %) | 13, 59.1 |
| | High, > 14.6 Months (n, %) | 9, 40.9 |
| **Time to Recurrence** | Median (Months) | 10.5 |

**Table 4.S1 Summary of the demographic, tumor, surgical and clinical characteristics of the retrospective GBM patient cohort**

| | Coefficient |
|---|---|
| **Constant** | -7.202 |
| **Highly Motile Cells (%)** | 0.149 |
| **Narrow Entry (%)** | 0.065 |
| **Highly Motile Ki67+ (%)** | 0.096 |

**Table 4.S2 Values of the coefficients and constant of logistic regression as determined and used for the computation of composite MIND score**

# Chapter 5 Future Directions

### 5.1 Characterizing the roles of NHERF2 on pancreatic cancer cell migration

In Chapter 3, we investigated the molecular mechanisms by which PODXL promotes pancreatic cancer cell migration. Contrary to the widely reported binding partners of PODXL as being ezrin and/or NHERF1/2, we instead discovered a novel direct binding interaction between PODXL and dynamin-2, which in turn modulates microtubules and focal adhesion dynamics to facilitate cell motility (**Figure 3.6**). While ezrin is ubiquitously absent in the immunoprecipitate fraction of PODXL, as assessed by both mass spectrometry and western blot (**Table 3.1, Figure 3.3.A**), NHERF2 was actually enriched in the immunoprecipitate fraction of PODXL (**Table 3.1**). Co-immunoprecipitation experiment using NHERF2 specific antibody also pulled down PODXL (**Figure 3.S4.C**). Interestingly, while both dynamin-2 and NHERF2 independently pulled down PODXL, they were unable to pull down each other, indicating that PODXL forms distinct complexes with dynamin-2 and NHERF2 independently (**Figure 3.S4.C-D**).

To examine the role of NHERF2 on the motility of PODXL-expressing pancreatic cancer cells, we knocked down NHERF2 in SW1990 and subjected them to our standard microchannel migration assay (**Figure 3.S4.E**). In distinct contrast to the inhibitory effect of knocking down PODXL and dynamin-2 on cell migration, NHERF2-KD cells moved much faster than scramble control cells (**Figure 3.S4.F**). Of note, NHERF2-KD cells also exhibit a clear mesenchymal/protrusive phenotype as opposed to the epithelial/rounded morphology of scramble control or PODXL-KD cells (**Figure 5.1.A**). In view of these results and given that PODXL and/or dynamin-2 knockdown suppress migration to an equivalent extent without any additive effect, we conclude that dynamin-2 regulates PODXL-mediated migration of pancreatic

cancer cells via its direct binding interaction with PODXL, independent of PODXL binding to NHERF2. The precise role of NHERF2 in pancreatic cancer cell migration, which may extend beyond PODXL, deserves further investigation.

Given that both dynamin-2 and NHERF2 are capable of binding to PODXL independently and the divergent effects of knocking down either of these proteins on cell migration, one can reasonably postulate that NHERF2 may serve as a competitive binding inhibitor to dynamin-2. When the level of NHERF2 is decreased as a result of NHERF2-KD, more PODXL may become available for binding to dynamin-2, leading the faster microtubule growth, reduced focal adhesion density, and ultimately enhanced cell migration. Several experiments can be performed to test this hypothesis. Firstly, we can knock down NHERF2 in cells with also PODXL and/or dynamin-2 knockdown (or using dynamin-2 inhibited cells with dynasore) to assess the effect of this double knockdown intervention on cell migration. If the hypothesis is true, knocking down NHERF2 will not be able to increase the migration of cells with depleted PODXL or dynamin-2 as they are the important upstream signaling molecules that sustain efficient cell migration. Secondly, we can compare the levels of dynamin-2 that are being co-immunoprecipitated with PODXL in both scramble control and NHERF2-KD cells. If NHERF2 is indeed a competitive binding inhibitor to dynamin-2, we will expect to detect higher level of dynamin-2 in the immunoprecipitate fraction of PODXL derived from NHERF2-KD cells. Thirdly, we can measure and compare the rate of microtubule growth and focal adhesion density of scramble control and NHERF2-KD cells. If the proposed mechanism is correct, we will expect a higher rate of microtubule growth and a lower focal adhesion density in NHERF-2 KD cells. However, this result will only at best be supporting the hypothesis and not proving it directly, as there

could be other factors independent of PODXL and/or dynamin2 that can alter microtubule and focal adhesion dynamics following the loss of NHERF2 (as discussed further below).

While it is true that PODXL binds to NHERF2, it is also entirely possible that there exist other distinct mechanisms by which NHERF2 promotes pancreatic cancer cell migration that is independent of PODXL. One striking difference between the scramble control and the NHERF2-KD cells is their morphology. Scramble control cells assumed a more rounded and epithelial-like morphology while NHERF2-KD cells were significantly more protrusive and mesenchymal (**Figure 5.1.A**), leading one to suspect that loss of NHERF2 may be triggering EMT. In fact, preliminary evidence from western blot and quantitative polymerase chain reaction (QPCR) indicate that EMT is indeed induced by knocking down NHERF2. Specifically, NHERF2-KD cells demonstrated significantly lower mRNA expression of epithelial marker such as E-cadherin, and higher levels of mesenchymal markers like N-cadherin, vimentin, TWIST, fibronectin, α smooth muscle actin and α1-integrin (**Figure 5.1.B**). Western blot further verified that NHERF2 KD cells expressed lower amount of epithelial markers such as E-cadherin and ZO-1, and higher amount of mesenchymal markers including N-cadherin, vimentin, ZEB1, SNAIL, SLUG (**Figure 5.1.C**). Aside from the apparent differences in cellular morphology induced by EMT, there is also preliminary evidence revealing that other oncogenic pathways may have also been altered. NHERF2-KD cells showed significantly higher rate of proliferation (**Figure 5.1.E**), suggesting that signaling pathways that are crucial for cell proliferation and survival such as PI3K/Akt/mTOR, NF-κB and Ras/Raf/MAPK may be activated. This hypothesis can be tested by performing western blots using antibodies specific for phosphorylation of key proteins involved in the signaling pathways of interest using cell lysates

derived from scramble control versus NHERF2-KD cells. The effects of knocking down NHERF2 on the other hallmarks of cancer, such as immune evasion, energy metabolism, MMP-dependent invasion and drug resistance, also deserve to be further characterized.

While it has become evident that the loss of NHERF2 in pancreatic cancer cells enhances cell migration and proliferation (and potentially also other relevant hallmarks of cancer), there is still the important question as to why it occurs. The first natural suspect is PODXL. PODXL has been reported to be needed for TGF-β induced EMT in lung carninoma (150). Even though knocking down PODXL alone did not induce EMT (**Figure 5.1.D**), it may be possible that this is due to the inhibitory role of NHERF2 binding to PODXL. In the absence of NHERF2, more PODXL may become available to induce EMT. While the exact mechanism by which PODXL may be inducing EMT is still not convincingly proven or established, it will be interesting to ascertain if PODXL is required for EMT caused by the loss of NHERF2. This can be achieved by accessing EMT induction in PODXL-KD cells with concurrent NHERF2-KD. In the literature, NHERF2 has been reported to be primarily a scaffolding protein that connects the actin cytoskeleton to the plasma membrane with limited signaling function. Yet, we have observed a multitude of oncogenic changes as a result of knocking down NHERF2. It is therefore possible that loss of NHERF2 may cause some disturbances in linkages between the plasma membrane and the actin cytoskeleton, which could potentially result in changes in cellular and/or membrane tension. Changes in cell membrane tension have been reported to alter YAP/TAZ signaling and trigger EMT via a mechanosensitive channel-dependent manner (212,213). As such, changes in the other biophysical properties of NHERF2-KD cells which have the potential to affect global transcriptional gene changes deserves further examination.

Finally, in order to provide some clinical perspective to the role of NHERF2 in pancreatic cancer progression, a preliminary Kaplan-Meier curve analysis was generated using data from mRNA expression levels of NHERF2 among patients with pancreatic ductal adenocarcinoma obtained from the open source online KM-Plotter software. The data revealed a significantly better prognosis and longer median survival in patients with higher expression of NHERF2 (**Figure 5.1.F**). To further substantiate its clinical relevance, pancreatic cancer tissue microarray can be immunostained for NHERF2 to compare the expression of NHERF2 between normal healthy pancreatic tissues and pancreatic tumors of varying grades. The immunohistochemistriy staining experiment will reveal if NHERF2 expression is decreased during the transformation of healthy tissues to pancreatic cancers. A western blot panel can also be performed to compare the endogenous levels of NHERF2 in normal pancreatic epithelial cells such as HPNE and HPDE to that of pancreatic ductal adenocarcinoma cell lines like SW1990 and Pa03c. Lastly, the *in vivo* significance of NHERF2-KD on pancreatic cancer metastasis can also be investigated via the same hemispleen mice model as used in the PODXL project.

**5.2 Assessing the roles of giant obscurin on pancreatic cancer metastasis**

Aside from PODXL and NHERF2, another protein that our lab has previously shown to affect pancreatic cancer cell migration is obscurin. Obscurins are giant cytoskeletal proteins with structural and regulatory roles that are encoded by the OBSCN gene (214,215). Mutations to the OBSCN gene have been associated with pancreatic ductal carcinoma and the loss of obscurin from breast cancer has resulted in increased tumorigenicity and cell migration (216-220). Previously, we established that obscurin expression is depleted in pancreatic ductal

adenocarcinoma tissue and metastatic cell lines, but remains unaltered in normal pancreatic tissue and non-tumorigenic human pancreatic ductal epithelial cells (HPDE). Stable clones of HPDE cells lacking obscurins resulted in the modification of two key signaling pathways, RhoA and PI3K/AKT, which in turn leads to major cytoskeletal alterations including increased actin and microtubule dynamics and decreased focal adhesion density, ultimately resulting in faster cell migration (**Figure 5.2**). However, we have yet to establish the *in vivo* functional significance of obscurin loss in promoting pancreatic cancer metastasis. Previous attempts at generating tumors *in vivo* with HPDE, either via subcutaneous injection or hemispleen models, have failed as HPDE cells are non-tumorigenic *in vivo*, despite even using a modified variant HPDE with activating KRAS mutation. To circumvent this issue, we knocked down obscurins in another pancreatic ductal adenocarcinoma cell lines, Panc5.04. We verified that obscurin loss in Panc5.04 resulted in the same mechanobiological phenotype as obscurin-depleted HPDE cells, namely Panc5.04 Obscurin-KD cells display downregulation of RhoA activity, activation of PI3K/Akt pathway, increased actin and microtubule dynamics, decreased focal adhesion density and enhanced cell migration. We plan to next investigate the ability for these obscurin-depleted Panc5.04 cells to facilitate metastasis *in vivo* with the hemispleen mice model.

### 5.3 Validating the prognostic capability of MIND for personalized medicine

In Chapter 4, we described the development of a novel *in vitro* testing platform, MIND, which can be used to assess the migratory and proliferative potentials of patient-derived GBM cells to predict patient survival. We achieved high sensitivity, specificity and accuracy in correctly classifying patients into either low or high survivals using a retrospective dataset consisting of 22 patients. We further validated the prognostic ability of MIND with a small number of 4

prospective patients, where we successfully predicted the survival outcome of all 4 patients. We plan to recruit more patients prospectively and test these new and fresh GBM specimens in MIND to increase the sample size of the prospective patient cohort to validate the prognosis power of MIND for actual clinical usage.

Aside from improving and substantiating the performance of MIND as a survival prediction tool, we also plan to extend MIND for testing various therapeutic agents against cells isolated from individual patients to predict responses to therapy. Since the migratory and proliferative abilities (as assessed simultaneously via composite MIND score) of GBMs correlate with patient survival, if a drug is able to decrease the composite MIND score to below the low versus high survival threshold, it would then suggest that there is a high probability that the drug has the potential to prolong patient survival. We can further validate the prediction using *in vivo* mice models to see if that particular drug is also able to improve outcome and extend survival in mice. As a proof of concept, we have tested an EGFR inhibitor, erlotinib that has investigated clinically in patients with recurrent malignant gliomas, on the migration of patient-derived primary GBM cells in MIND and observed a consistent inhibitory effect (**Figure 5.3.A**). The ultimate goal is to develop MIND as a companion tool by which clinician can rapidly obtain useful prognostic information, as well as to use it as a drug-testing platform to optimize therapeutic strategies for individual patients to hopefully extend their survival.

Lastly, we plan to extend MIND beyond GBMs to other solid cancer cell types for precision medicine. The versatility of MIND to other cancer cell types has already been demonstrated previously in breast cancer where the migratory and proliferative potentials of these cells

correlate with metastatic potential (**Figure 5.3.B**). Using a similar approach, we plan to expand the utility of MIND to pancreatic cancer. We will first test a panel of pancreatic cancer cell lines and correlate with their ability to metastasize, either as accessed from literature search or empirically with hemispleen mice model. Already we have tested the migratory behaviors of several pancreatic cancer cell lines *in vitro* with MIND (**Figure 5.3.C**). Furthermore, we also propose to collaborate with surgeons who have accessed to pancreatic cancer specimen to see if MIND can also be used to correlate with actual clinical outcomes in pancreatic cancer patients.

## 5.4 Figures

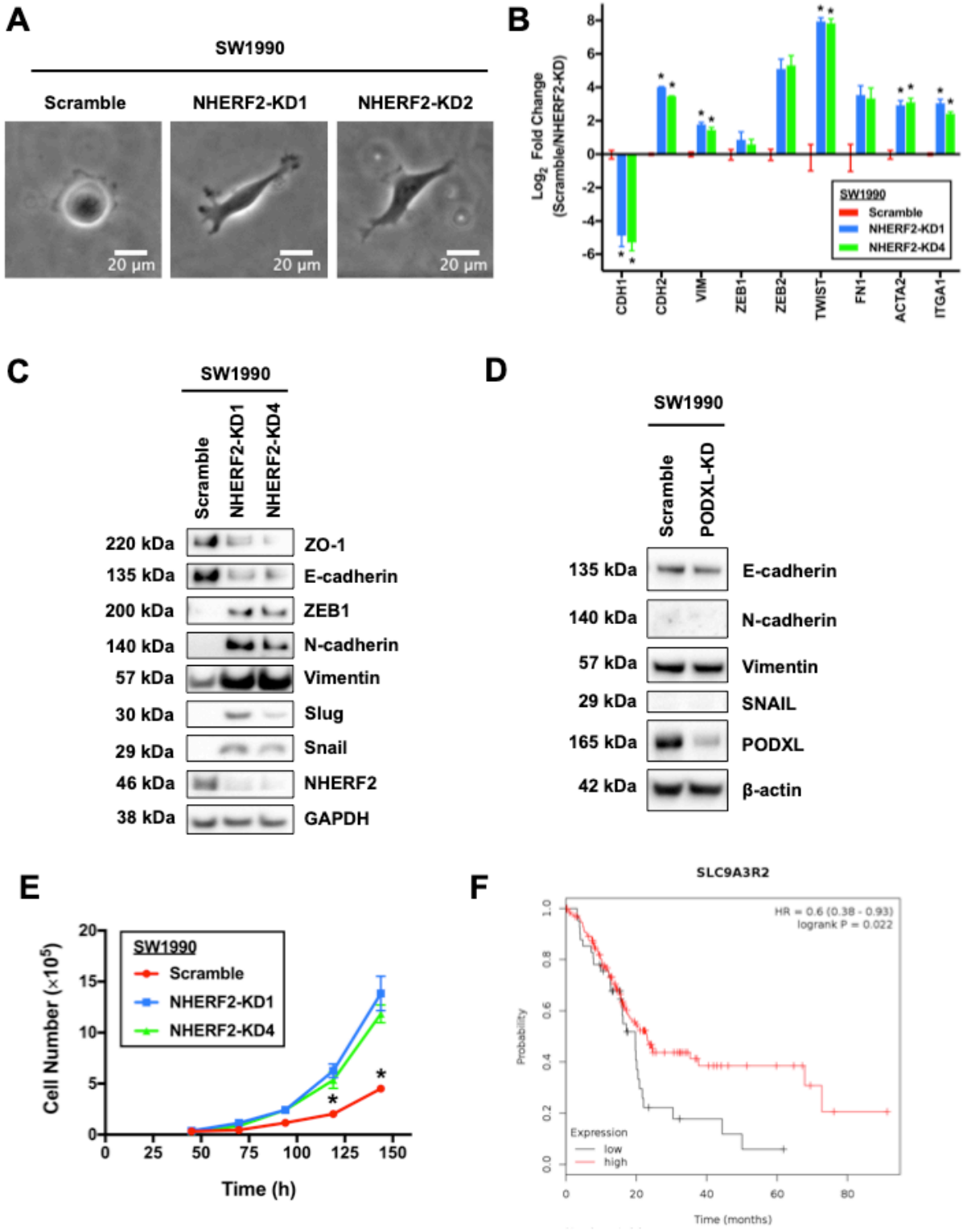
A
SW1990
Scramble
NHERF2-KD1
NHERF2-KD2
20 μm
20 μm
20 μm
B
Log2 Fold Change (Scramble/NHERF2-KD)
SW1990
Scramble
NHERF2-KD1
NHERF2-KD4
CDH1
CDH2
VIM
ZEB1
ZEB2
TWIST
FN1
ACTA2
ITGA1
C
SW1990
Scramble
NHERF2-KD1
NHERF2-KD4
220 kDa ZO-1
135 kDa E-cadherin
200 kDa ZEB1
140 kDa N-cadherin
57 kDa Vimentin
30 kDa Slug
29 kDa Snail
46 kDa NHERF2
38 kDa GAPDH
D
SW1990
Scramble
PODXL-KD
135 kDa E-cadherin
140 kDa N-cadherin
57 kDa Vimentin
29 kDa SNAIL
165 kDa PODXL
42 kDa β-actin
E
Cell Number (×10^5)
SW1990
Scramble
NHERF2-KD1
NHERF2-KD4
Time (h)
F
SLC9A3R2
HR = 0.6 (0.38 - 0.93)
logrank P = 0.022
Probability
Expression
low
high
Time (months)

**Figure 5.1 NHERF2 downregulation promotes EMT and proliferation in pancreatic cancer cells, and is associated with poorer patient survival**

**(A)** Morphology of scramble control, NHERF2-KD1 and NHERF2-KD4 SW1990 pancreatic cancer cells on 2D collagen I-coated glass coverslips. NHERF2-KD cells displayed more elongated and protrusive phenotypes as compared to scramble control cells. **(B)** QPCR results showing mRNA downregulation of epithelial marker (CDH1/E-cadherin) and upregulation of mesenchymal marker (CDH2/N-cadherin, vimentin, Zeb1, Zeb2, TWIST1, fibronectin, α smooth muscle actin, α1 integrin) in NHERF2-KD cells. Data represent the mean±S.E.M. from 3 independent experiments. * represents $p<0.05$ between scramble control and NHERF2-KD1 or NHERF2-KD4. **(C)** Western blot results showing protein downregulation of epithelial marker (ZO-1, E-cadherin) and upregulation of mesenchymal marker (Zeb1, N-cadherin, Vimentin, SNAIL, SLUG) in NHERF2-KD cells. GAPDH was blotted as the loading control. **(D)** Western blot showing no changes in epithelial (E-cadherin) or mesenchymal markers (N-cadherin, Vimentin, SNAIL) in PODXL-KD cells. β-actin was blotted as the loading control. **(E)** *in vitro* growth rate of scramble control, NHERF2-KD1 and NHERF2-KD4 SW1990 cells. Data represent the mean±S.E.M. from 3 independent experiments. * represents $p<0.05$ between scramble control and NHERF2-KD1 or NHERF2-KD4. **(F)** Kaplan-Meier survival curve comparison of patients with low versus high expression of NHERF2 (also known as SLC9A3R2). Data obtained from KM-Plotter.

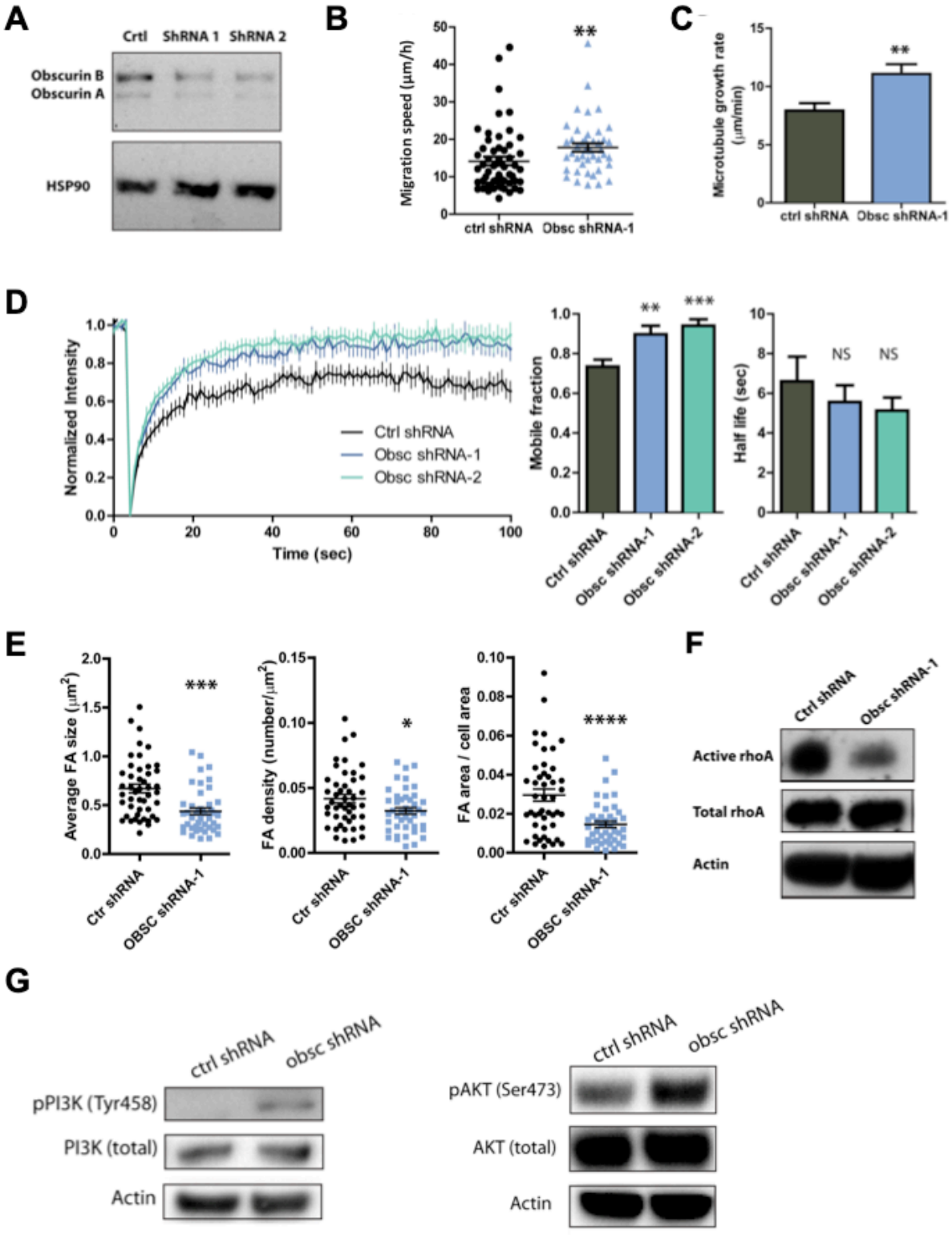
A
Crtl
ShRNA 1
ShRNA 2
Obscurin B
Obscurin A
HSP90
B
Migration speed (µm/h)
**
ctrl shRNA
Obsc shRNA-1
C
Microtubule growth rate (µm/min)
**
ctrl shRNA
Obsc shRNA-1
D
Normalized Intensity
Time (sec)
Ctrl shRNA
Obsc shRNA-1
Obsc shRNA-2
Mobile fraction
**
***
Half life (sec)
NS
NS
E
Average FA size (µm²)
***
FA density (number/µm²)
*
FA area / cell area
****
Ctr shRNA
OBSC shRNA-1
F
Ctrl shRNA
Obsc shRNA-1
Active rhoA
Total rhoA
Actin
G
ctrl shRNA
obsc shRNA
pPI3K (Tyr458)
PI3K (total)
Actin
pAKT (Ser473)
AKT (total)
Actin

**Figure 5.2 Downregulation of obscurin in HPDE cells enhances migration by regulating microtubule, actin and focal adhesion dynamics, and modulating RhoA and PI3K signaling**

**(A)** Western blot showing successful knockdown of giant obscurin in HPDE cells. HSP90 was blotted as the loading control **(B)** Obsc shRNA-1 cells migrate faster than the scramble control cells in microchannels of 10 μm in height and width and 200 μm in length. **(C)** Microtubule growth rate as assessed by EB1-GFP of scramble control versus Obsc shRNA-1 cells. **(D)** FRAP curves showing the fraction of LifeAct-GFP recovery overtime for scramble control, Obsc shRNA-1 and Obsc shRNA-2 HPDE cells (left panel). Average of the mobile fraction (middle panel) and the half-life of LifeAct-GFP recovery (right panel) are shown. **(E)** Average focal adhesion size per cell (left panel), the average focal adhesion density per cell (middle panel) and the average focal adhesion area per cell area (right panel) for scramble control and Obsc shRNA-1 HPDE cells. **(F)** Active RhoA is decreased in Obsc shRNA-1 HPDE cells. **(G)** Levels of pPI3K (Tyr458, left panel) and the downstream effector pAKT (Ser473, right panel) were increased in in Obsc shRNA-1 HPDE cells. * represents $p< 0.05$, ** represents $p<0.01$, *** represents $p<0.001$, **** represents $p<0.0001$.

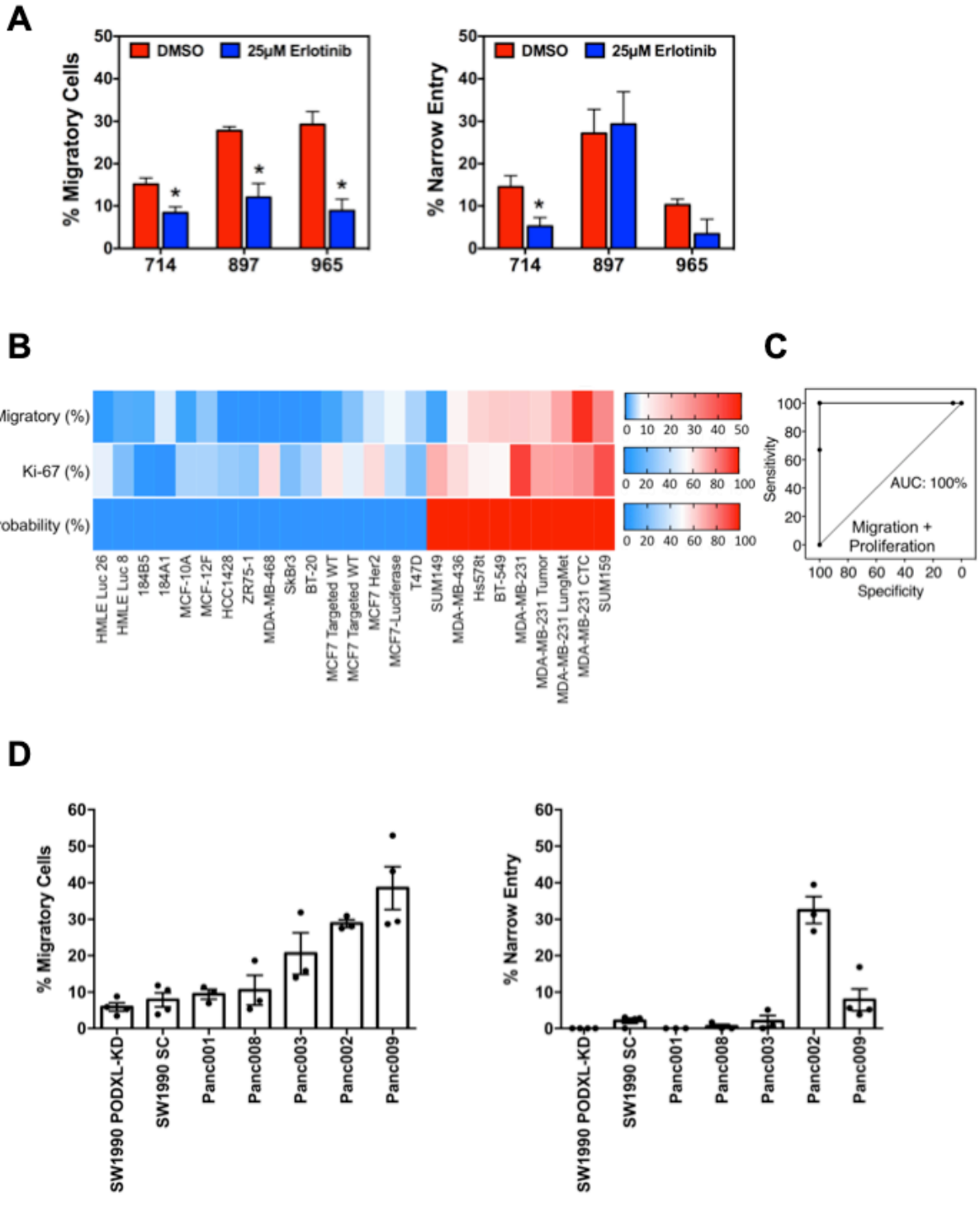
A
% Migratory Cells
DMSO
25μM Erlotinib
714
897
965
% Narrow Entry
B
Migratory (%)
Ki-67 (%)
Probability (%)
HMLE Luc 26
HMLE Luc 8
184B5
184A1
MCF-10A
MCF-12F
HCC1428
ZR75-1
MDA-MB-468
SkBr3
BT-20
MCF7 Targeted WT
MCF7 Targeted WT
MCF7 Her2
MCF7-Luciferase
T47D
SUM149
MDA-MB-436
Hs578t
BT-549
MDA-MB-231
MDA-MB-231 Tumor
MDA-MB-231 LungMet
MDA-MB-231 CTC
SUM159
C
Sensitivity
Specificity
AUC: 100%
Migration +
Proliferation
D
% Migratory Cells
% Narrow Entry
SW1990 PODXL-KD
SW1990 SC
Panc001
Panc008
Panc003
Panc002
Panc009

**Figure 5.3 MIND is amendable for drug testing and prognosis of other solid cancer cell types**

**(A)** An EGFR inhibitor, erlotinib, decreases the migratory potential of patient-derived primary GBM cells in MIND. Data represent the mean±S.E.M. from n≥3 independent experiments. * represents $p < 0.05$ between vehicle control and 25 μM erlotinib **(B-C)** MIND predicts the metastatic potential of breast cancer cell lines with 100% accuracy. **(D)** MIND is adaptable for the measurement of migratory potential of pancreatic cancer cell lines.

# Chapter 6 Conclusion

Cell motility is one of the key determinants of the spread and eventually lethality of cancer. This is especially pertinent for pancreatic cancer and GBM, which are notorious for their poor clinical outcomes due to aggressive local infiltration and/or widespread distant metastasis that impede complete and effective tumor eradication by currently available treatment options. A more in depth understanding of the molecular basis of cancer cell migration thus allows for identification of new oncogenic and/or tumor suppressor genes, and their associated downstream signaling pathways, that could potentially serve as novel diagnostic and therapeutic targets for these aggressive cancers. In the case of pancreatic cancer for instance, we have characterized and delineated the roles and mechanisms by which PODXL regulates cancer cell motility and metastasis, in which one could subsequently target to suppress migration and aggressiveness of pancreatic cancers. Besides examining cell migration at the biochemical and cellular levels, one can also adopt a more global and systematic approach to utilize the migratory phenotypes of cancer cells for actual clinical applications. By measuring and comparing the differences in the migratory and proliferative potentials of patient-derived primary GBM cells, we demonstrated that MIND can accurately predict patient survival and time to recurrence, illustrating promising potential to guide personalized medicine and improve the quality of life of GBM patients. Overall, by studying cell migration in a multidisciplinary approach, we are able to both attain a deeper understanding on the factors underlying cancer aggressiveness and translate this knowledge into prospective tangible clinical benefits.

# Bibliography


1. Hanahan D, Weinberg RA. Hallmarks of cancer: the next generation. Cell **2011**;144:646-74
2. Siegel RL, Miller KD, Jemal A. Cancer statistics, 2018. CA Cancer J Clin **2018**;68:7-30
3. Kamisawa T, Wood LD, Itoi T, Takaori K. Pancreatic cancer. Lancet **2016**;388:73-85
4. Bray F, Ferlay J, Soerjomataram I, Siegel RL, Torre LA, Jemal A. Global cancer statistics 2018: GLOBOCAN estimates of incidence and mortality worldwide for 36 cancers in 185 countries. CA Cancer J Clin **2018**;68:394-424
5. Rahib L, Smith BD, Aizenberg R, Rosenzweig AB, Fleshman JM, Matrisian LM. Projecting cancer incidence and deaths to 2030: the unexpected burden of thyroid, liver, and pancreas cancers in the United States. Cancer Res **2014**;74:2913-21
6. Kleeff J, Korc M, Apte M, La Vecchia C, Johnson CD, Biankin AV*, et al.* Pancreatic cancer. Nat Rev Dis Primers **2016**;2:16022
7. Jenkinson C, Earl J, Ghaneh P, Halloran C, Carrato A, Greenhalf W*, et al.* Biomarkers for early diagnosis of pancreatic cancer. Expert Rev Gastroenterol Hepatol **2015**;9:305-15
8. Del Chiaro M, Segersvard R, Lohr M, Verbeke C. Early detection and prevention of pancreatic cancer: is it really possible today? World J Gastroenterol **2014**;20:12118-31
9. Hruban RH, Maitra A, Goggins M. Update on pancreatic intraepithelial neoplasia. Int J Clin Exp Pathol **2008**;1:306-16
10. Hidalgo M. New insights into pancreatic cancer biology. Ann Oncol **2012**;23 Suppl 10:x135-8

11. Abramson MA, Jazag A, van der Zee JA, Whang EE. The molecular biology of pancreatic cancer. Gastrointest Cancer Res **2007**;1:S7-S12

12. Wood LD, Hruban RH. Pathology and molecular genetics of pancreatic neoplasms. Cancer J **2012**;18:492-501

13. Kanda M, Matthaei H, Wu J, Hong SM, Yu J, Borges M*, et al.* Presence of somatic mutations in most early-stage pancreatic intraepithelial neoplasia. Gastroenterology **2012**;142:730-3 e9

14. Preis M, Korc M. Signaling pathways in pancreatic cancer. Crit Rev Eukaryot Gene Expr **2011**;21:115-29

15. McKenna S, Eatock M. The medical management of pancreatic cancer: a review. Oncologist **2003**;8:149-60

16. Neoptolemos JP, Kleeff J, Michl P, Costello E, Greenhalf W, Palmer DH. Therapeutic developments in pancreatic cancer: current and future perspectives. Nat Rev Gastroenterol Hepatol **2018**;15:333-48

17. Omuro A, DeAngelis LM. Glioblastoma and other malignant gliomas: a clinical review. JAMA **2013**;310:1842-50

18. Cronin KA, Ries LA, Edwards BK. The Surveillance, Epidemiology, and End Results (SEER) Program of the National Cancer Institute. Cancer **2014**;120 Suppl 23:3755-7

19. Ostrom QT, Gittleman H, Truitt G, Boscia A, Kruchko C, Barnholtz-Sloan JS. CBTRUS Statistical Report: Primary Brain and Other Central Nervous System Tumors Diagnosed in the United States in 2011-2015. Neuro Oncol **2018**;20:iv1-iv86

20. Porter KR, McCarthy BJ, Freels S, Kim Y, Davis FG. Prevalence estimates for primary brain tumors in the United States by age, gender, behavior, and histology. Neuro Oncol **2010**;12:520-7

21. Dolecek TA, Propp JM, Stroup NE, Kruchko C. CBTRUS statistical report: primary brain and central nervous system tumors diagnosed in the United States in 2005-2009. Neuro Oncol **2012**;14 Suppl 5:v1-49

22. Schwartzbaum JA, Fisher JL, Aldape KD, Wrensch M. Epidemiology and molecular pathology of glioma. Nat Clin Pract Neurol **2006**;2:494-503; quiz 1 p following 16

23. Chaichana KL, Jusue-Torres I, Navarro-Ramirez R, Raza SM, Pascual-Gallego M, Ibrahim A*, et al.* Establishing percent resection and residual volume thresholds affecting survival and recurrence for patients with newly diagnosed intracranial glioblastoma. Neuro Oncol **2014**;16:113-22

24. Chaichana KL, Cabrera-Aldana EE, Jusue-Torres I, Wijesekera O, Olivi A, Rahman M*, et al.* When gross total resection of a glioblastoma is possible, how much resection should be achieved? World Neurosurg **2014**;82:e257-65

25. Stupp R, Mason WP, van den Bent MJ, Weller M, Fisher B, Taphoorn MJ*, et al.* Radiotherapy plus concomitant and adjuvant temozolomide for glioblastoma. N Engl J Med **2005**;352:987-96

26. Chaichana KL, Zadnik P, Weingart JD, Olivi A, Gallia GL, Blakeley J*, et al.* Multiple resections for patients with glioblastoma: prolonging survival. J Neurosurg **2013**;118:812-20

27. Chen R, Nishimura MC, Bumbaca SM, Kharbanda S, Forrest WF, Kasman IM*, et al.* A hierarchy of self-renewing tumor-initiating cell types in glioblastoma. Cancer Cell **2010**;17:362-75

28. Heywood RM, Marcus HJ, Ryan DJ, Piccirillo SG, Al-Mayhani TM, Watts C. A review of the role of stem cells in the development and treatment of glioma. Acta Neurochir (Wien) **2012**;154:951-69; discussion 69

29. Cancer Genome Atlas Research N. Comprehensive genomic characterization defines human glioblastoma genes and core pathways. Nature **2008**;455:1061-8

30. Verhaak RG, Hoadley KA, Purdom E, Wang V, Qi Y, Wilkerson MD*, et al.* Integrated genomic analysis identifies clinically relevant subtypes of glioblastoma characterized by abnormalities in PDGFRA, IDH1, EGFR, and NF1. Cancer Cell **2010**;17:98-110

31. Seystahl K, Wick W, Weller M. Therapeutic options in recurrent glioblastoma--An update. Crit Rev Oncol Hematol **2016**;99:389-408

32. Chinot OL, Wick W, Saran F, Mason WP, Henriksson R, Nishikawa R*, et al.* AVAglio: A phase III trial of bevacizumab added to standard radiotherapy and temozolomide in patients with newly diagnosed glioblastoma. J Clin Oncol **2011**;29

33. Gilbert MR, Dignam J, Won M, Blumenthal DT, Vogelbaum MA, Aldape KD*, et al.* RTOG 0825: Phase III double-blind placebo-controlled trial evaluating bevacizumab (Bev) in patients (Pts) with newly diagnosed glioblastoma (GBM). J Clin Oncol **2013**;31

34. Weller M, Yung WK. Angiogenesis inhibition for glioblastoma at the edge: beyond AVAGlio and RTOG 0825. Neuro Oncol **2013**;15:971

35. Westphal M, Hilt DC, Bortey E, Delavault P, Olivares R, Warnke PC*, et al.* A phase 3 trial of local chemotherapy with biodegradable carmustine (BCNU) wafers (Gliadel wafers) in patients with primary malignant glioma. Neuro Oncol **2003**;5:79-88

36. Hottinger AF, Pacheco P, Stupp R. Tumor treating fields: a novel treatment modality and its use in brain tumors. Neuro Oncol **2016**;18:1338-49

37. Haas-Kogan DA, Prados MD, Tihan T, Eberhard DA, Jelluma N, Arvold ND*, et al.* Epidermal growth factor receptor, protein kinase B/Akt, and glioma response to erlotinib. J Natl Cancer Inst **2005**;97:880-7

38. Tan AC, Heimberger AB, Khasraw M. Immune Checkpoint Inhibitors in Gliomas. Curr Oncol Rep **2017**;19

39. Sengupta S, Mao G, Gokaslan ZS, Sampath P. Chimeric antigen receptors for treatment of glioblastoma: a practical review of challenges and ways to overcome them. Cancer Gene Ther **2017**;24:121-9

40. Walid MS. Prognostic factors for long-term survival after glioblastoma. Perm J **2008**;12:45-8

41. Phillips HS, Kharbanda S, Chen R, Forrest WF, Soriano RH, Wu TD*, et al.* Molecular subclasses of high-grade glioma predict prognosis, delineate a pattern of disease progression, and resemble stages in neurogenesis. Cancer Cell **2006**;9:157-73

42. Colman H, Aldape K. Molecular predictors in glioblastoma: toward personalized therapy. Arch Neurol **2008**;65:877-83

43. Hegi ME, Diserens AC, Gorlia T, Hamou MF, de Tribolet N, Weller M*, et al.* MGMT gene silencing and benefit from temozolomide in glioblastoma. N Engl J Med **2005**;352:997-1003

44. Hamilton MG, Roldan G, Magliocco A, McIntyre JB, Parney I, Easaw JC. Determination of the methylation status of MGMT in different regions within glioblastoma multiforme. J Neuro-Oncol **2011**;102:255-60

45. Costa BM, Caeiro C, Guimaraes I, Martinho O, Jaraquemada T, Augusto I*, et al.* Prognostic value of MGMT promoter methylation in glioblastoma patients treated with temozolomide-based chemoradiation: a Portuguese multicentre study. Oncol Rep **2010**;23:1655-62

46. Yan H, Parsons DW, Jin G, McLendon R, Rasheed BA, Yuan W*, et al.* IDH1 and IDH2 mutations in gliomas. N Engl J Med **2009**;360:765-73

47. Koshland DE, Jr., Walsh K, LaPorte DC. Sensitivity of metabolic fluxes to covalent control. Curr Top Cell Regul **1985**;27:13-22

48. Dang L, White DW, Gross S, Bennett BD, Bittinger MA, Driggers EM*, et al.* Cancer-associated IDH1 mutations produce 2-hydroxyglutarate. Nature **2010**;465:966

49. Zhao S, Lin Y, Xu W, Jiang W, Zha Z, Wang P*, et al.* Glioma-derived mutations in IDH1 dominantly inhibit IDH1 catalytic activity and induce HIF-1alpha. Science **2009**;324:261-5

50. Ichimura K, Pearson DM, Kocialkowski S, Backlund LM, Chan R, Jones DT*, et al.* IDH1 mutations are present in the majority of common adult gliomas but rare in primary glioblastomas. Neuro Oncol **2009**;11:341-7

51. Steeg PS. Targeting metastasis. Nat Rev Cancer **2016**;16:201-18

52. Lambert AW, Pattabiraman DR, Weinberg RA. Emerging Biological Principles of Metastasis. Cell **2017**;168:670-91

53. Trepat X, Chen Z, Jacobson K. Cell migration. Compr Physiol **2012**;2:2369-92

54. Friedl P, Alexander S. Cancer invasion and the microenvironment: plasticity and reciprocity. Cell **2011**;147:992-1009

55. Paluch EK, Aspalter IM, Sixt M. Focal Adhesion-Independent Cell Migration. Annu Rev Cell Dev Biol **2016**;32:469-90

56. Wirtz D, Konstantopoulos K, Searson PC. The physics of cancer: the role of physical interactions and mechanical forces in metastasis. Nat Rev Cancer **2011**;11:512-22

57. Wolf K, Alexander S, Schacht V, Coussens LM, von Andrian UH, van Rheenen J*, et al.* Collagen-based cell migration models in vitro and in vivo. Seminars in cell & developmental biology **2009**;20:931-41

58. Wolf K, Te Lindert M, Krause M, Alexander S, Te Riet J, Willis AL*, et al.* Physical limits of cell migration: control by ECM space and nuclear deformation and tuning by proteolysis and traction force. The Journal of cell biology **2013**;201:1069-84

59. Wolf K, Mazo I, Leung H, Engelke K, von Andrian UH, Deryugina EI*, et al.* Compensation mechanism in tumor cell migration: mesenchymal-amoeboid transition after blocking of pericellular proteolysis. The Journal of cell biology **2003**;160:267-77

60. Petrie RJ, Harlin HM, Korsak LI, Yamada KM. Activating the nuclear piston mechanism of 3D migration in tumor cells. The Journal of cell biology **2017**;216:93-100

61. Sahai E, Marshall CJ. Differing modes of tumour cell invasion have distinct requirements for Rho/ROCK signalling and extracellular proteolysis. Nat Cell Biol **2003**;5:711-9

62. Gritsenko PG, Ilina O, Friedl P. Interstitial guidance of cancer invasion. J Pathol **2012**;226:185-99

63. Lugassy C, Zadran S, Bentolila LA, Wadehra M, Prakash R, Carmichael ST*, et al.* Angiotropism, pericytic mimicry and extravascular migratory metastasis in melanoma: an alternative to intravascular cancer dissemination. Cancer Microenviron **2014**;7:139-52

64. Bentolila LA, Prakash R, Mihic-Probst D, Wadehra M, Kleinman HK, Carmichael TS*, et al.* Imaging of Angiotropism/Vascular Co-Option in a Murine Model of Brain Melanoma: Implications for Melanoma Progression along Extravascular Pathways. Sci Rep **2016**;6:23834

65. Alexander S, Koehl GE, Hirschberg M, Geissler EK, Friedl P. Dynamic imaging of cancer growth and invasion: a modified skin-fold chamber model. Histochem Cell Biol **2008**;130:1147-54

66. Cuddapah VA, Robel S, Watkins S, Sontheimer H. A neurocentric perspective on glioma invasion. Nat Rev Neurosci **2014**;15:455-65

67. Shieh AC, Rozansky HA, Hinz B, Swartz MA. Tumor cell invasion is promoted by interstitial flow-induced matrix priming by stromal fibroblasts. Cancer Res **2011**;71:790-800

68. Gaggioli C, Hooper S, Hidalgo-Carcedo C, Grosse R, Marshall JF, Harrington K*, et al.* Fibroblast-led collective invasion of carcinoma cells with differing roles for RhoGTPases in leading and following cells. Nat Cell Biol **2007**;9:1392-400

69. Paul CD, Mistriotis P, Konstantopoulos K. Cancer cell motility: lessons from migration in confined spaces. Nat Rev Cancer **2017**;17:131-40

70. Paul CD, Hung WC, Wirtz D, Konstantopoulos K. Engineered Models of Confined Cell Migration. Annu Rev Biomed Eng **2016**;18:159-80

71. Abercrombie M, Heaysman JE, Pegrum SM. The locomotion of fibroblasts in culture. I. Movements of the leading edge. Exp Cell Res **1970**;59:393-8

72. Ridley AJ, Schwartz MA, Burridge K, Firtel RA, Ginsberg MH, Borisy G*, et al.* Cell migration: integrating signals from front to back. Science **2003**;302:1704-9

73. Ananthakrishnan R, Ehrlicher A. The forces behind cell movement. Int J Biol Sci **2007**;3:303-17

74. Reig G, Pulgar E, Concha ML. Cell migration: from tissue culture to embryos. Development **2014**;141:1999-2013

75. Tschumperlin DJ. Fibroblasts and the ground they walk on. Physiology (Bethesda) **2013**;28:380-90

76. Maretzky T, Evers A, Zhou W, Swendeman SL, Wong PM, Rafii S*, et al.* Migration of growth factor-stimulated epithelial and endothelial cells depends on EGFR transactivation by ADAM17. Nat Commun **2011**;2:229

77. Tong Z, Balzer EM, Dallas MR, Hung WC, Stebe KJ, Konstantopoulos K. Chemotaxis of cell populations through confined spaces at single-cell resolution. PLoS One **2012**;7:e29211

78. Sanz-Moreno V, Gaggioli C, Yeo M, Albrengues J, Wallberg F, Viros A*, et al.* ROCK and JAK1 signaling cooperate to control actomyosin contractility in tumor cells and stroma. Cancer Cell **2011**;20:229-45

79. Pathak A, Kumar S. Independent regulation of tumor cell migration by matrix stiffness and confinement. Proc Natl Acad Sci U S A **2012**;109:10334-9

80. Brown MJ, Loew LM. Electric field-directed fibroblast locomotion involves cell surface molecular reorganization and is calcium independent. The Journal of cell biology **1994**;127:117-28

81. Schmoranzer J, Kreitzer G, Simon SM. Migrating fibroblasts perform polarized, microtubule-dependent exocytosis towards the leading edge. J Cell Sci **2003**;116:4513-9

82. Weiger MC, Wang CC, Krajcovic M, Melvin AT, Rhoden JJ, Haugh JM. Spontaneous phosphoinositide 3-kinase signaling dynamics drive spreading and random migration of fibroblasts. J Cell Sci **2009**;122:313-23

83. Kraynov VS, Chamberlain C, Bokoch GM, Schwartz MA, Slabaugh S, Hahn KM. Localized Rac activation dynamics visualized in living cells. Science **2000**;290:333-7

84. Nalbant P, Hodgson L, Kraynov V, Toutchkine A, Hahn KM. Activation of endogenous Cdc42 visualized in living cells. Science **2004**;305:1615-9

85. Wu C, Asokan SB, Berginski ME, Haynes EM, Sharpless NE, Griffith JD*, et al.* Arp2/3 is critical for lamellipodia and response to extracellular matrix cues but is dispensable for chemotaxis. Cell **2012**;148:973-87

86. Lawson C, Lim ST, Uryu S, Chen XL, Calderwood DA, Schlaepfer DD. FAK promotes recruitment of talin to nascent adhesions to control cell motility. The Journal of cell biology **2012**;196:223-32

87. Watanabe N, Kato T, Fujita A, Ishizaki T, Narumiya S. Cooperation between mDia1 and ROCK in Rho-induced actin reorganization. Nat Cell Biol **1999**;1:136-43

88. Gupton SL, Eisenmann K, Alberts AS, Waterman-Storer CM. mDia2 regulates actin and focal adhesion dynamics and organization in the lamella for efficient epithelial cell migration. J Cell Sci **2007**;120:3475-87

89. Chrzanowska-Wodnicka M, Burridge K. Rho-stimulated contractility drives the formation of stress fibers and focal adhesions. The Journal of cell biology **1996**;133:1403-15

90. Parsons JT, Horwitz AR, Schwartz MA. Cell adhesion: integrating cytoskeletal dynamics and cellular tension. Nature reviews Molecular cell biology **2010**;11:633-43

91. Tsujioka M, Yumura S, Inouye K, Patel H, Ueda M, Yonemura S. Talin couples the actomyosin cortex to the plasma membrane during rear retraction and cytokinesis. Proc Natl Acad Sci U S A **2012**;109:12992-7

92. Gomes ER, Jani S, Gundersen GG. Nuclear movement regulated by Cdc42, MRCK, myosin, and actin flow establishes MTOC polarization in migrating cells. Cell **2005**;121:451-63

93. Petrie RJ, Gavara N, Chadwick RS, Yamada KM. Nonpolarized signaling reveals two distinct modes of 3D cell migration. The Journal of cell biology **2012**;197:439-55

94. Doyle AD, Wang FW, Matsumoto K, Yamada KM. One-dimensional topography underlies three-dimensional fibrillar cell migration. The Journal of cell biology **2009**;184:481-90

95. Kraning-Rush CM, Carey SP, Lampi MC, Reinhart-King CA. Microfabricated collagen tracks facilitate single cell metastatic invasion in 3D. Integr Biol (Camb) **2013**;5:606-16

96. Carey SP, Rahman A, Kraning-Rush CM, Romero B, Somasegar S, Torre OM*, et al.* Comparative mechanisms of cancer cell migration through 3D matrix and physiological microtracks. Am J Physiol Cell Physiol **2015**;308:C436-47

97. Balzer EM, Tong Z, Paul CD, Hung WC, Stroka KM, Boggs AE*, et al.* Physical confinement alters tumor cell adhesion and migration phenotypes. FASEB J **2012**;26:4045-56

98. Hung WC, Chen SH, Paul CD, Stroka KM, Lo YC, Yang JT*, et al.* Distinct signaling mechanisms regulate migration in unconfined versus confined spaces. J Cell Biol **2013**;202:807-24

99. Paul CD, Shea DJ, Mahoney MR, Chai A, Laney V, Hung WC*, et al.* Interplay of the physical microenvironment, contact guidance, and intracellular signaling in cell decision making. FASEB J **2016**;30:2161-70

100. Maiuri P, Terriac E, Paul-Gilloteaux P, Vignaud T, McNally K, Onuffer J*, et al.* The first World Cell Race. Curr Biol **2012**;22:R673-5

101. Petrie RJ, Yamada KM. Fibroblasts Lead the Way: A Unified View of 3D Cell Motility. Trends Cell Biol **2015**;25:666-74

102. Chang SS, Guo WH, Kim Y, Wang YL. Guidance of cell migration by substrate dimension. Biophys J **2013**;104:313-21

103. Wilson K, Lewalle A, Fritzsche M, Thorogate R, Duke T, Charras G. Mechanisms of leading edge protrusion in interstitial migration. Nat Commun **2013**;4:2896

104. Stroka KM, Jiang H, Chen SH, Tong Z, Wirtz D, Sun SX*, et al.* Water permeation drives tumor cell migration in confined microenvironments. Cell **2014**;157:611-23

105. Hung WC, Yang JR, Yankaskas CL, Wong BS, Wu PH, Pardo-Pastor C*, et al.* Confinement Sensing and Signal Optimization via Piezo1/PKA and Myosin II Pathways. Cell Rep **2016**;15:1430-41

106. Raman PS, Paul CD, Stroka KM, Konstantopoulos K. Probing cell traction forces in confined microenvironments. Lab Chip **2013**;13:4599-607

107. Provenzano PP, Inman DR, Eliceiri KW, Trier SM, Keely PJ. Contact guidance mediated three-dimensional cell migration is regulated by Rho/ROCK-dependent matrix reorganization. Biophys J **2008**;95:5374-84

108. Even-Ram S, Doyle AD, Conti MA, Matsumoto K, Adelstein RS, Yamada KM. Myosin IIA regulates cell motility and actomyosin-microtubule crosstalk. Nat Cell Biol **2007**;9:299-309

109. Zhang J, Wang YL. Centrosome defines the rear of cells during mesenchymal migration. Mol Biol Cell **2017**

110. Tozluoglu M, Tournier AL, Jenkins RP, Hooper S, Bates PA, Sahai E. Matrix geometry determines optimal cancer cell migration strategy and modulates response to interventions. Nat Cell Biol **2013**;15:751-62

111. Bergert M, Chandradoss SD, Desai RA, Paluch E. Cell mechanics control rapid transitions between blebs and lamellipodia during migration. Proc Natl Acad Sci U S A **2012**;109:14434-9

112. Bergert M, Erzberger A, Desai RA, Aspalter IM, Oates AC, Charras G*, et al.* Force transmission during adhesion-independent migration. Nat Cell Biol **2015**;17:524-9

113. Carragher NO, Walker SM, Scott Carragher LA, Harris F, Sawyer TK, Brunton VG*, et al.* Calpain 2 and Src dependence distinguishes mesenchymal and amoeboid modes of tumour cell invasion: a link to integrin function. Oncogene **2006**;25:5726-40

114. Orgaz JL, Pandya P, Dalmeida R, Karagiannis P, Sanchez-Laorden B, Viros A*, et al.* Diverse matrix metalloproteinase functions regulate cancer amoeboid migration. Nat Commun **2014**;5:4255

115. Vandenbroucke RE, Libert C. Is there new hope for therapeutic matrix metalloproteinase inhibition? Nat Rev Drug Discov **2014**;13:904-27

116. Fingleton B. MMPs as therapeutic targets--still a viable option? Seminars in cell & developmental biology **2008**;19:61-8

117. Liu YJ, Le Berre M, Lautenschlaeger F, Maiuri P, Callan-Jones A, Heuze M*, et al.* Confinement and low adhesion induce fast amoeboid migration of slow mesenchymal cells. Cell **2015**;160:659-72

118. Ruprecht V, Wieser S, Callan-Jones A, Smutny M, Morita H, Sako K*, et al.* Cortical contractility triggers a stochastic switch to fast amoeboid cell motility. Cell **2015**;160:673-85

119. Madsen CD, Hooper S, Tozluoglu M, Bruckbauer A, Fletcher G, Erler JT*, et al.* STRIPAK components determine mode of cancer cell migration and metastasis. Nat Cell Biol **2015**;17:68-80

120. Coste B, Mathur J, Schmidt M, Earley TJ, Ranade S, Petrus MJ*, et al.* Piezo1 and Piezo2 are essential components of distinct mechanically activated cation channels. Science **2010**;330:55-60

121. Dupont S, Morsut L, Aragona M, Enzo E, Giulitti S, Cordenonsi M*, et al.* Role of YAP/TAZ in mechanotransduction. Nature **2011**;474:179-83

122. Roca-Cusachs P, Iskratsch T, Sheetz MP. Finding the weakest link: exploring integrin-mediated mechanical molecular pathways. J Cell Sci **2012**;125:3025-38

123. Fernandez-Gonzalez R, Simoes Sde M, Roper JC, Eaton S, Zallen JA. Myosin II dynamics are regulated by tension in intercalating cells. Dev Cell **2009**;17:736-43

124. Ren Y, Effler JC, Norstrom M, Luo T, Firtel RA, Iglesias PA*, et al.* Mechanosensing through cooperative interactions between myosin II and the actin crosslinker cortexillin I. Curr Biol **2009**;19:1421-8

125. Frey MT, Tsai IY, Russell TP, Hanks SK, Wang YL. Cellular responses to substrate topography: role of myosin II and focal adhesion kinase. Biophys J **2006**;90:3774-82

126. Minton K. Cell migration: Putting pressure on the lead. Nature reviews Molecular cell biology **2014**;15:631

127. Petrie RJ, Koo H, Yamada KM. Generation of compartmentalized pressure by a nuclear piston governs cell motility in a 3D matrix. Science **2014**;345:1062-5

128. Tominaga T, Ishizaki T, Narumiya S, Barber DL. p160ROCK mediates RhoA activation of Na-H exchange. EMBO J **1998**;17:4712-22

129. Chae YK, Woo J, Kim MJ, Kang SK, Kim MS, Lee J*, et al.* Expression of aquaporin 5 (AQP5) promotes tumor invasion in human non small cell lung cancer. PLoS One **2008**;3:e2162

130. Jung HJ, Park JY, Jeon HS, Kwon TH. Aquaporin-5: a marker protein for proliferation and migration of human breast cancer cells. PLoS One **2011**;6:e28492

131. Martial S. Involvement of ion channels and transporters in carcinoma angiogenesis and metastasis. Am J Physiol Cell Physiol **2016**;310:C710-27

132. Prentice-Mott HV, Chang CH, Mahadevan L, Mitchison TJ, Irimia D, Shah JV. Biased migration of confined neutrophil-like cells in asymmetric hydraulic environments. Proc Natl Acad Sci U S A **2013**;110:21006-11

133. Kerjaschki D, Sharkey DJ, Farquhar MG. Identification and characterization of podocalyxin--the major sialoprotein of the renal glomerular epithelial cell. J Cell Biol **1984**;98:1591-6

134. Kerosuo L, Juvonen E, Alitalo R, Gylling M, Kerjaschki D, Miettinen A. Podocalyxin in human haematopoietic cells. Br J Haematol **2004**;124:809-18

135. Sassetti C, Tangemann K, Singer MS, Kershaw DB, Rosen SD. Identification of podocalyxin-like protein as a high endothelial venule ligand for L-selectin: parallels to CD34. J Exp Med **1998**;187:1965-75

136. Kusumoto H, Shintani Y, Kanzaki R, Kawamura T, Funaki S, Minami M*, et al.* Podocalyxin influences malignant potential by controlling epithelial-mesenchymal transition in lung adenocarcinoma. Cancer Sci **2017**;108:528-35

137. Somasiri A, Nielsen JS, Makretsov N, McCoy ML, Prentice L, Gilks CB*, et al.* Overexpression of the anti-adhesin podocalyxin is an independent predictor of breast cancer progression. Cancer Res **2004**;64:5068-73

138. Cipollone JA, Graves ML, Kobel M, Kalloger SE, Poon T, Gilks CB*, et al.* The anti-adhesive mucin podocalyxin may help initiate the transperitoneal metastasis of high grade serous ovarian carcinoma. Clin Exp Metastasis **2012**;29:239-52

139. Boman K, Larsson AH, Segersten U, Kuteeva E, Johannesson H, Nodin B*, et al.* Membranous expression of podocalyxin-like protein is an independent factor of poor prognosis in urothelial bladder cancer. Br J Cancer **2013**;108:2321-8

140. Hsu YH, Lin WL, Hou YT, Pu YS, Shun CT, Chen CL*, et al.* Podocalyxin EBP50 ezrin molecular complex enhances the metastatic potential of renal cell carcinoma through

recruiting Rac1 guanine nucleotide exchange factor ARHGEF7. Am J Pathol **2010**;176:3050-61

141. Larsson A, Johansson ME, Wangefjord S, Gaber A, Nodin B, Kucharzewska P*, et al.* Overexpression of podocalyxin-like protein is an independent factor of poor prognosis in colorectal cancer. Br J Cancer **2011**;105:666-72

142. Heby M, Elebro J, Nodin B, Jirstrom K, Eberhard J. Prognostic and predictive significance of podocalyxin-like protein expression in pancreatic and periampullary adenocarcinoma. BMC Clin Pathol **2015**;15:10

143. Thomas SN, Schnaar RL, Konstantopoulos K. Podocalyxin-like protein is an E-/L-selectin ligand on colon carcinoma cells: comparative biochemical properties of selectin ligands in host and tumor cells. Am J Physiol Cell Physiol **2009**;296:C505-13

144. Dallas MR, Chen SH, Streppel MM, Sharma S, Maitra A, Konstantopoulos K. Sialofucosylated podocalyxin is a functional E- and L-selectin ligand expressed by metastatic pancreatic cancer cells. Am J Physiol Cell Physiol **2012**;303:C616-24

145. Nielsen JS, McNagny KM. The role of podocalyxin in health and disease. J Am Soc Nephrol **2009**;20:1669-76

146. Orlando RA, Takeda T, Zak B, Schmieder S, Benoit VM, McQuistan T*, et al.* The glomerular epithelial cell anti-adhesin podocalyxin associates with the actin cytoskeleton through interactions with ezrin. J Am Soc Nephrol **2001**;12:1589-98

147. Schmieder S, Nagai M, Orlando RA, Takeda T, Farquhar MG. Podocalyxin activates RhoA and induces actin reorganization through NHERF1 and Ezrin in MDCK cells. J Am Soc Nephrol **2004**;15:2289-98

148. Takeda T, McQuistan T, Orlando RA, Farquhar MG. Loss of glomerular foot processes is associated with uncoupling of podocalyxin from the actin cytoskeleton. J Clin Invest **2001**;108:289-301

149. Sizemore S, Cicek M, Sizemore N, Ng KP, Casey G. Podocalyxin increases the aggressive phenotype of breast and prostate cancer cells in vitro through its interaction with ezrin. Cancer Res **2007**;67:6183-91

150. Meng X, Ezzati P, Wilkins JA. Requirement of podocalyxin in TGF-beta induced epithelial mesenchymal transition. PLoS One **2011**;6:e18715

151. Fernandez D, Horrillo A, Alquezar C, Gonzalez-Manchon C, Parrilla R, Ayuso MS. Control of cell adhesion and migration by podocalyxin. Implication of Rac1 and Cdc42. Biochem Biophys Res Commun **2013**;432:302-7

152. Lin CW, Sun MS, Liao MY, Chung CH, Chi YH, Chiou LT*, et al.* Podocalyxin-like 1 promotes invadopodia formation and metastasis through activation of Rac1/Cdc42/cortactin signaling in breast cancer cells. Carcinogenesis **2014**;35:2425-35

153. Ney JT, Zhou H, Sipos B, Buttner R, Chen X, Kloppel G*, et al.* Podocalyxin-like protein 1 expression is useful to differentiate pancreatic ductal adenocarcinomas from adenocarcinomas of the biliary and gastrointestinal tracts. Hum Pathol **2007**;38:359-64

154. Taniuchi K, Furihata M, Naganuma S, Dabanaka K, Hanazaki K, Saibara T. Podocalyxin-like protein, linked to poor prognosis of pancreatic cancers, promotes cell invasion by binding to gelsolin. Cancer Sci **2016**;107:1430-42

155. Saukkonen K, Hagstrom J, Mustonen H, Juuti A, Nordling S, Fermer C*, et al.* Podocalyxin Is a Marker of Poor Prognosis in Pancreatic Ductal Adenocarcinoma. PLoS One **2015**;10:e0129012

156. Chijiiwa Y, Moriyama T, Ohuchida K, Nabae T, Ohtsuka T, Miyasaka Y*, et al.* Overexpression of microRNA-5100 decreases the aggressive phenotype of pancreatic cancer cells by targeting PODXL. Int J Oncol **2016**;48:1688-700

157. Soares KC, Foley K, Olino K, Leubner A, Mayo SC, Jain A*, et al.* A preclinical murine model of hepatic metastases. J Vis Exp **2014**:51677

158. Jones S, Zhang X, Parsons DW, Lin JC, Leary RJ, Angenendt P*, et al.* Core signaling pathways in human pancreatic cancers revealed by global genomic analyses. Science **2008**;321:1801-6

159. Chen SH, Hung WC, Wang P, Paul C, Konstantopoulos K. Mesothelin binding to CA125/MUC16 promotes pancreatic cancer cell motility and invasion via MMP-7 activation. Sci Rep **2013**;3:1870

160. Stroka KM, Wong BS, Shriver M, Phillip JM, Wirtz D, Kontrogianni-Konstantopoulos A*, et al.* Loss of giant obscurins alters breast epithelial cell mechanosensing of matrix stiffness. Oncotarget **2017**;8:54004-20

161. Shriver M, Stroka KM, Vitolo MI, Martin S, Huso DL, Konstantopoulos K*, et al.* Loss of giant obscurins from breast epithelium promotes epithelial-to-mesenchymal transition, tumorigenicity and metastasis. Oncogene **2015**;34:4248-59

162. Wang Y, Cao H, Chen J, McNiven MA. A direct interaction between the large GTPase dynamin-2 and FAK regulates focal adhesion dynamics in response to active Src. Mol Biol Cell **2011**;22:1529-38

163. Etienne-Manneville S. Actin and microtubules in cell motility: which one is in control? Traffic **2004**;5:470-7

164. Tanabe K, Takei K. Dynamic instability of microtubules requires dynamin 2 and is impaired in a Charcot-Marie-Tooth mutant. J Cell Biol **2009**;185:939-48

165. Eppinga RD, Krueger EW, Weller SG, Zhang L, Cao H, McNiven MA. Increased expression of the large GTPase dynamin 2 potentiates metastatic migration and invasion of pancreatic ductal carcinoma. Oncogene **2012**;31:1228-41

166. Francis SS, Sfakianos J, Lo B, Mellman I. A hierarchy of signals regulates entry of membrane proteins into the ciliary membrane domain in epithelial cells. J Cell Biol **2011**;193:219-33

167. Doyonnas R, Nielsen JS, Chelliah S, Drew E, Hara T, Miyajima A*, et al.* Podocalyxin is a CD34-related marker of murine hematopoietic stem cells and embryonic erythroid cells. Blood **2005**;105:4170-8

168. Mrozowska PS, Fukuda M. Regulation of podocalyxin trafficking by Rab small GTPases in 2D and 3D epithelial cell cultures. J Cell Biol **2016**;213:355-69

169. Richards M, Hetheridge C, Mellor H. The Formin FMNL3 Controls Early Apical Specification in Endothelial Cells by Regulating the Polarized Trafficking of Podocalyxin. Curr Biol **2015**;25:2325-31

170. Strilic B, Eglinger J, Krieg M, Zeeb M, Axnick J, Babal P*, et al.* Electrostatic cell-surface repulsion initiates lumen formation in developing blood vessels. Curr Biol **2010**;20:2003-9

171. Strilic B, Kucera T, Eglinger J, Hughes MR, McNagny KM, Tsukita S*, et al.* The molecular basis of vascular lumen formation in the developing mouse aorta. Dev Cell **2009**;17:505-15

172. Nielsen JS, Graves ML, Chelliah S, Vogl AW, Roskelley CD, McNagny KM. The CD34-related molecule podocalyxin is a potent inducer of microvillus formation. PLoS One **2007**;2:e237

173. Stehbens S, Wittmann T. Targeting and transport: how microtubules control focal adhesion dynamics. J Cell Biol **2012**;198:481-9

174. Mitrugno A, Tormoen GW, Kuhn P, McCarty OJ. The prothrombotic activity of cancer cells in the circulation. Blood Rev **2016**;30:11-9

175. Berny-Lang MA, Aslan JE, Tormoen GW, Patel IA, Bock PE, Gruber A*, et al.* Promotion of experimental thrombus formation by the procoagulant activity of breast cancer cells. Phys Biol **2011**;8:015014

176. Palou J, Algaba F, Vera I, Rodriguez O, Villavicencio H, Sanchez-Carbayo M. Protein expression patterns of ezrin are predictors of progression in T1G3 bladder tumours treated with nonmaintenance bacillus Calmette-Guerin. Eur Urol **2009**;56:829-36

177. Snyder KA, Hughes MR, Hedberg B, Brandon J, Hernaez DC, Bergqvist P*, et al.* Podocalyxin enhances breast tumor growth and metastasis and is a target for monoclonal antibody therapy. Breast Cancer Res **2015**;17:46

178. Zeitouni D, Pylayeva-Gupta Y, Der CJ, Bryant KL. KRAS Mutant Pancreatic Cancer: No Lone Path to an Effective Treatment. Cancers (Basel) **2016**;8

179. Scholz A, Heinze S, Detjen KM, Peters M, Welzel M, Hauff P*, et al.* Activated signal transducer and activator of transcription 3 (STAT3) supports the malignant phenotype of human pancreatic cancer. Gastroenterology **2003**;125:891-905

180. Thissen JA, Gross JM, Subramanian K, Meyer T, Casey PJ. Prenylation-dependent association of Ki-Ras with microtubules. Evidence for a role in subcellular trafficking. J Biol Chem **1997**;272:30362-70

181. Yan B, Xie S, Liu Z, Luo Y, Zhou J, Li D*, et al.* STAT3 association with microtubules and its activation are independent of HDAC6 activity. DNA Cell Biol **2015**;34:290-5

182. Kelber JA, Reno T, Kaushal S, Metildi C, Wright T, Stoletov K*, et al.* KRas induces a Src/PEAK1/ErbB2 kinase amplification loop that drives metastatic growth and therapy resistance in pancreatic cancer. Cancer Res **2012**;72:2554-64

183. Chaichana K, Parker S, Olivi A, Quinones-Hinojosa A. A proposed classification system that projects outcomes based on preoperative variables for adult patients with glioblastoma multiforme. J Neurosurg **2010**;112:997-1004

184. Chaichana KL, Pendleton C, Chambless L, Camara-Quintana J, Nathan JK, Hassam-Malani L*, et al.* Multi-institutional validation of a preoperative scoring system which predicts survival for patients with glioblastoma. J Clin Neurosci **2013**;20:1422-6

185. Wei S, Wang J, Oyinlade O, Ma D, Wang S, Kratz L*, et al.* Heterozygous IDH1(R132H/WT) created by "single base editing" inhibits human astroglial cell growth by downregulating YAP. Oncogene **2018**;37:5160-74

186. Grossman R, Burger P, Soudry E, Tyler B, Chaichana KL, Weingart J*, et al.* MGMT inactivation and clinical response in newly diagnosed GBM patients treated with Gliadel. J Clin Neurosci **2015**;22:1938-42

187. Parsons DW, Jones S, Zhang X, Lin JC, Leary RJ, Angenendt P*, et al.* An integrated genomic analysis of human glioblastoma multiforme. Science **2008**;321:1807-12

188. Brennan CW, Verhaak RG, McKenna A, Campos B, Noushmehr H, Salama SR*, et al.* The somatic genomic landscape of glioblastoma. Cell **2013**;155:462-77

189. Noushmehr H, Weisenberger DJ, Diefes K, Phillips HS, Pujara K, Berman BP*, et al.* Identification of a CpG island methylator phenotype that defines a distinct subgroup of glioma. Cancer Cell **2010**;17:510-22

190. Jaeckle KA, Eyre HJ, Townsend JJ, Schulman S, Knudson HM, Belanich M*, et al.* Correlation of tumor O6 methylguanine-DNA methyltransferase levels with survival of malignant astrocytoma patients treated with bis-chloroethylnitrosourea: a Southwest Oncology Group study. J Clin Oncol **1998**;16:3310-5

191. Hegi ME, Diserens AC, Godard S, Dietrich PY, Regli L, Ostermann S*, et al.* Clinical trial substantiates the predictive value of O-6-methylguanine-DNA methyltransferase promoter methylation in glioblastoma patients treated with temozolomide. Clin Cancer Res **2004**;10:1871-4

192. Shah SR Q-HA, Xia S. Advances in Brain Cancer: Creating Monoallelic Single Point Mutation in IDH1 by Single Base Editing. Journal of Oncology Research and Therapy **2018**;05:1-3

193. Preusser M, Charles Janzer R, Felsberg J, Reifenberger G, Hamou MF, Diserens AC*, et al.* Anti-O6-methylguanine-methyltransferase (MGMT) immunohistochemistry in glioblastoma multiforme: observer variability and lack of association with patient survival impede its use as clinical biomarker. Brain Pathol **2008**;18:520-32

194. Grasbon-Frodl EM, Kreth FW, Ruiter M, Schnell O, Bise K, Felsberg J*, et al.* Intratumoral homogeneity of MGMT promoter hypermethylation as demonstrated in

serial stereotactic specimens from anaplastic astrocytomas and glioblastomas. Int J Cancer **2007**;121:2458-64

195. Hartmann C, Meyer J, Balss J, Capper D, Mueller W, Christians A*, et al.* Type and frequency of IDH1 and IDH2 mutations are related to astrocytic and oligodendroglial differentiation and age: a study of 1,010 diffuse gliomas. Acta Neuropathol **2009**;118:469-74

196. Joo KM, Kim J, Jin J, Kim M, Seol HJ, Muradov J*, et al.* Patient-specific orthotopic glioblastoma xenograft models recapitulate the histopathology and biology of human glioblastomas in situ. Cell Rep **2013**;3:260-73

197. Specht H, Slavov N. Transformative Opportunities for Single-Cell Proteomics. J Proteome Res **2018**;17:2565-71

198. Wills QF, Mead AJ. Application of single-cell genomics in cancer: promise and challenges. Hum Mol Genet **2015**;24:R74-84

199. Chandler Y, Schechter CB, Jayasekera J, Near A, O'Neill SC, Isaacs C*, et al.* Cost Effectiveness of Gene Expression Profile Testing in Community Practice. J Clin Oncol **2018**;36:554-62

200. Lippman M, Osborne CK. Circulating tumor DNA--ready for prime time? N Engl J Med **2013**;368:1249-50

201. Smith CL, Chaichana KL, Lee YM, Lin B, Stanko KM, O'Donnell T*, et al.* Pre-exposure of human adipose mesenchymal stem cells to soluble factors enhances their homing to brain cancer. Stem Cells Transl Med **2015**;4:239-51

202. Smith CL, Kilic O, Schiapparelli P, Guerrero-Cazares H, Kim DH, Sedora-Roman NI*, et al.* Migration Phenotype of Brain-Cancer Cells Predicts Patient Outcomes. Cell Rep **2016**;15:2616-24

203. Shah SR, David JM, Tippens ND, Mohyeldin A, Martinez-Gutierrez JC, Ganaha S*, et al.* Brachyury-YAP Regulatory Axis Drives Stemness and Growth in Cancer. Cell Rep **2017**;21:495-507

204. Xie Q, Mittal S, Berens ME. Targeting adaptive glioblastoma: an overview of proliferation and invasion. Neuro Oncol **2014**;16:1575-84

205. Inwald EC, Klinkhammer-Schalke M, Hofstadter F, Zeman F, Koller M, Gerstenhauer M*, et al.* Ki-67 is a prognostic parameter in breast cancer patients: results of a large population-based cohort of a cancer registry. Breast Cancer Res Tr **2013**;139:539-52

206. Wong E, Nahar N, Hau E, Varikatt W, Gebski V, Ng T*, et al.* Cut-point for Ki-67 proliferation index as a prognostic marker for glioblastoma. Asia-Pac J Clin Onco **2019**;15:5-9

207. Liu JC, Zacksenhouse M, Eisen A, Nofech-Mozes S, Zacksenhaus E. Identification of cell proliferation, immune response and cell migration as critical pathways in a prognostic signature for HER2+:ERalpha- breast cancer. PLoS One **2017**;12:e0179223

208. Armento A, Ehlers J, Schotterl S, Naumann U. Molecular Mechanisms of Glioma Cell Motility. In: De Vleeschouwer S, editor. Glioblastoma. Brisbane (AU)2017.

209. Gritsenko P, Leenders W, Friedl P. Recapitulating in vivo-like plasticity of glioma cell invasion along blood vessels and in astrocyte-rich stroma. Histochem Cell Biol **2017**;148:395-406

210. Friedlander DR, Zagzag D, Shiff B, Cohen H, Allen JC, Kelly PJ*, et al.* Migration of brain tumor cells on extracellular matrix proteins in vitro correlates with tumor type and grade and involves alphaV and beta1 integrins. Cancer Res **1996**;56:1939-47

211. Abubakar M, Orr N, Daley F, Coulson P, Ali HR, Blows F*, et al.* Prognostic value of automated KI67 scoring in breast cancer: a centralised evaluation of 8088 patients from 10 study groups. Breast Cancer Res **2016**;18

212. Perez Gonzalez N, Tao J, Rochman ND, Vig D, Chiu E, Wirtz D*, et al.* Cell tension and mechanical regulation of cell volume. Mol Biol Cell **2018**;29:0

213. Kuipers AJ, Middelbeek J, Vrenken K, Perez-Gonzalez C, Poelmans G, Klarenbeek J*, et al.* TRPM7 controls mesenchymal features of breast cancer cells by tensional regulation of SOX4. Biochim Biophys Acta Mol Basis Dis **2018**;1864:2409-19

214. Russell MW, Raeker MO, Korytkowski KA, Sonneman KJ. Identification, tissue expression and chromosomal localization of human Obscurin-MLCK, a member of the titin and Dbl families of myosin light chain kinases. Gene **2002**;282:237-46

215. Fukuzawa A, Idowu S, Gautel M. Complete human gene structure of obscurin: implications for isoform generation by differential splicing. Journal of Muscle Research & Cell Motility **2005**;26:427-34

216. Shriver M, Stroka K, Vitolo M, Martin S, Huso DL, Konstantopoulos K*, et al.* Loss of giant obscurins from breast epithelium promotes epithelial-to-mesenchymal transition, tumorigenicity and metastasis. Oncogene **2015**;34:4248-59

217. Perry NA, Vitolo MI, Martin SS, Kontrogianni-Konstantopoulos A. Loss of the obscurin-RhoGEF downregulates RhoA signaling and increases microtentacle formation and attachment of breast epithelial cells. Oncotarget **2014**;5:8558

218. Hocker JR, Postier RG, Li M, Lerner MR, Lightfoot SA, Peyton MD*, et al.* Discriminating patients with early-stage pancreatic cancer or chronic pancreatitis using serum electrospray mass profiling. Cancer letters **2015**;359:314-24

219. Murphy SJ, Hart SN, Lima JF, Kipp BR, Klebig M, Winters JL*, et al.* Genetic alterations associated with progression from pancreatic intraepithelial neoplasia to invasive pancreatic tumor. Gastroenterology **2013**;145:1098-109. e1

220. Perry NA, Shriver M, Mameza MG, Grabias B, Balzer E, Kontrogianni-Konstantopoulos A. Loss of giant obscurins promotes breast epithelial cell survival through apoptotic resistance. The FASEB Journal **2012**;26:2764-75

# Curriculum Vitae


## Bin Sheng WONG, Ph.D.

*Johns Hopkins University, Baltimore, Maryland, USA*
*Department of Chemical and Biomolecular Engineering • Institute for NanoBioTechnology*
*Email: bswong@jhu.edu • Phone: 443-301-9009*
*Google Scholar: h-index = 7, total citations = 511*


## EDUCATION & QUALIFICATION

**Johns Hopkins University (JHU)** *Ph.D., Chemical and Biomolecular Engineering (2013-2019)*

- Grade point average: 4.00/4.00
- Thesis: Understanding and predicting cancer cell aggressiveness from their migratory phenotypes
- Advisor: Konstantinos Konstantopoulos

**National University of Singapore (NUS)** *Bachelor of Science (Pharmacy) Honors (2009-2013)*

- Cumulative average point: 4.96/5.00 (First Class Honors)
- Thesis: Delivery of platinum-based drugs via mitochondrial targeting carbon nanotubes
- Advisor: Giorgia Pastorin

## AWARDS & SCHOLARSHIPS

**Predoctoral Fellowships**

- William H. Schwarz Instructorship, Whiting School of Engineering Scholar (2013-2019)
- Cancer Nanotechnology Training Center Fellowship (2013-2017)
- Certificate of Advanced Study in NanoBioTechnology (2013-2017)

**Undergraduate Scholarships**

- Association of Southeast Asian Nations (ASEAN) Undergraduate Scholarship (2009-2013)

**Undergraduate Awards and Honors**

- Lee Kuan Yew Gold Medal, best graduate throughout the course of study (2013)
- Robert Lin Memorial Medal, best student in pharmacology modules (2013)
- Pharmaceutical Society of Singapore Prize for Pharmaceutics, best overall performance in pharmaceutics modules (2013)
- T.H Elliot Book Prize, best overall performance in pharmaceutical chemistry modules (2013)
- T.H Elliot Gold Medal, best overall performance in pharmacy modules (2013)
- Baxter Academic Excellence Prize, top year 3 pharmacy student (2012)
- Seven times recipient of Dean's List Awards (2009-2013)

## RESEARCH EXPERIENCES

**Konstantopoulos Lab, JHU.** *Ph.D. student of Professor Konstantinos Konstantopoulos (2013-2019)*

- The roles of podocalyxin (PODXL) in pancreatic cancer cell migration and metastasis

- Discovered the migratory potentiation effects of PODXL in pancreatic cancer cells
- Characterized the roles of PODXL on cytoskeleton and adhesion dynamics
- Identified dynamin-2 as a novel cytoplasmic binding partner to PODXL
- Validated the *in vivo* significance of PODXL in promoting metastasis with preclinical murine models

- Microfluidic Invasion Network Device (MIND) for glioblastoma prognosis and response to therapy
  - Led a multi-institution collaborative project with Mayo Clinic
  - Created a microfluidic device capable of correlating the migratory and proliferative potentials of patient-derived primary glioblastoma cell lines to patient clinical outcomes
  - Employed MIND as a drug testing platform for precision care
  - This work was awarded with the prestigious MPI-R01 grant from NCI and was submitted for a provisional patent application

**BioNanoTechnology Research Group, NUS.** *Researcher Assistant for Professor Giorgia Pastorin (2013)*

- Developed a novel carbon nanotube drug delivery system for specific delivery of platinum-based drugs into the mitochondria of cancer cells
- Prepared an invited review *for Advanced Drug Delivery Reviews* (IF: 15.6) on delivery of chemotherapeutics with carbon nanotubes
- Mentored undergraduate and exchange master students on techniques of chemical surface functionalization of carbon nanotubes

**Kang Lab, NUS.** *Undergraduate Research Assistant for Dr. Kang Lifeng (2011-2012)*

- Spearheaded the conceptualization of a new research project on transdermal nucleic acids delivery with polymeric microneedles
- Optimized and evaluated the use of propylene glycol organogels for transdermal drug delivery

## PUBLICATIONS

**Published or Accepted**

1. **Wong, B. S.**, Shea, D. J., Tuntithavornwat, S., Law, R. A., Bieber, J. M., Zheng, L., Konstantopoulos, K. (2018) "A direct Podocalyxin-Dynamin-2 interaction regulates cytoskeletal dynamics to promote migration and metastasis in pancreatic cancer cells". *Cancer Research* (In press) (IF: 9.1)
2. **Wong, B. S.,** Mistriotis, P., Konstantopoulos, K. (2018). "Exposing cell-itary confinement: Understanding the mechanisms of confined single cell migration". *Biomechanics in Oncology. Springer, Cham. 139-157* (Book Chapter)
3. Stroka, K. M., **Wong, B. S.**, Shriver, M., Phillip, J. M., Wirtz, D., Kontrogianni-Konstantopoulos, A., & Konstantopoulos, K. (2016). "Loss of giant obscurins alters breast epithelial cell mechanosensing of matrix stiffness". *Oncotarget*, 8 (33), 54004 (IF: 5.2)
4. Curreli, S., **Wong, B. S.**, Latinovic, O., Konstantopoulos, K., & Stamatos, N. M. (2016). "Class 3 semaphorins induce F-actin reorganization in human dendritic cells: Role in cell migration". *Journal of Leukocyte Biology*, 100(6), 1323-1334. (IF: 4.3)
5. Hung, W. C., Yang, J. R., Yankaskas, C. L., **Wong, B. S.**, Wu, P. H., Pardo-Pastor, C., Serra, S. A., Chiang, M., Gu, Z., Wirtz, D., Valverde, M. A., Yang, J. T., Zhang, J., Konstantopoulos, K. (2016). "Confinement sensing and signal optimization via Piezo1/PKA and Myosin II pathways". *Cell Reports*, 15(7), 1430-1441. (IF: 8.3)
6. He, L., Chen, W., Wu, P. H., Jimenez, A., **Wong, B. S.**, San, A., Konstantopoulos, K., Wirtz, D. (2016). "Local 3D matrix confinement determines division axis through cell shape". *Oncotarget*,

7(6), 6994. (IF: 5.2)

7. Nguyen, D. V., Li, F., Li, H., **Wong, B. S.**, Low, C. Y., Liu, X. Y., & Kang, L. (2014). "Drug permeation through skin is inversely correlated with carrier gel rigidity". *Molecular Pharmaceutics*, 12(2), 444-452. (IF: 4.4)
8. Yoong, S. L., **Wong, B. S.**, Zhou, Q. L., Chin, C. F., Li, J., Venkatesan, T., Ho, H. K., Yu, V., Ang, W. H., Pastorin, G. (2014). "Enhanced cytotoxicity to cancer cells by mitochondria-targeting MWCNTs containing platinum(IV) prodrug of cisplatin". *Biomaterials*, 35(2), 748-759. (IF: 8.4)
9. **Wong, B. S.***, Yoong, S. L., Jagusiak, A., Panczyk, T., Ho, H. K., Ang, W. H., Pastorin, G. (2013). "Carbon nanotubes for delivery of small molecule drugs". *Advanced Drug Delivery Reviews 65(15), 1964-2015.* (* First & corresponding author) (IF: 15.6)
10. Yan, J., **Wong, B. S.***, & Kang, L. (2013). "Molecular gels for tissue engineering". *Soft fibrillar materials*, pp. 129-162 (Book Chapter. * Equal contribution)
11. **Wong, B. S.**, Teoh, S., & Kang, L. (2012). "Polycaprolactone scaffold as targeted drug delivery system and cell attachment scaffold for postsurgical care of limb salvage". *Drug Delivery and Translational Research*, 2(4), 272-283. (IF: 3.1)
12. **Wong, B. S.**, & Kang, L. (2012). "Mastery learning in the context of university education". *Journal of the NUS Teaching Academy*, 4(2), 206-222.

**Submitted or In Preparation**

13. **Wong, B. S.*,** Shah, R. S.*, Yankaskas, C. L., Chin, D., ReFaey, K., Quiñones-Hinojosa, A., Konstantopoulos, K. (2019) "Predicting progression-free survival and recurrence time of glioblastoma patients with a Microfluidic Invasion Network Device (MIND)". (In review at *Nature Biomedical Engineering*) (* Co-first author)
14. **Wong, B. S.***, Shea, D. J.*, Tuntithavornwat, S., Zheng, L., Kontrogianni-Konstantopoulos, A., & Konstantopoulos, K. (2019) "Loss of giant obscurins promotes migration, tumor formation and metastasis in pancreatic ductal epithelial cells". (Manuscript in preparation) (* Co-first author)
15. Gu, Z., Li, J., Hsu, Y. H., Tonkova, E. A., Alexander, S., **Wong, B. S.,** Han, Z., Konstantopoulos, K., Friedl, P., Hung, M. C., Zhao, J. J., Segall, J. E., Hsu, V. W., Brenner, M. B. (2018) "Triple negative breast cancer cells hijack fibroblasts for invasion by cadherin-11 and such hijacking is dispensable in a high PDGF microenvironment by cadherin-11 sequestration on the Golgi". (Manuscript in preparation)

**Poster or Conference Presentations**

1. **Wong, B. S.**, Shea, D. J., Tuntithavornwat, S., Law, R. A., Bieber, J. M., Zheng, L., Konstantopoulos, K. (2018) "A direct Podocalyxin-Dynamin-2 interaction promotes pancreatic cancer cell migration and metastasis by altering cytoskeletal dynamics", Oral Presentation, 8th International Conference on Bioengineering and Nanotechnology, Baltimore, MD, May 28-31, 2019
2. **Wong, B. S.,** Shah, R. S., Yankasas, C. L., Chin, D., ReFaey, K., Quiñones-Hinojosa, A., Konstantopoulos, K. "The use of a Microfluidic Invasion Network Device (MIND) for glioblastoma prognosis", Oral Presentation, Biomedical Engineering Society Annual Meeting, Atlanta, GA, October 17-20, 2018
3. **Wong, B. S.**, Shea, D.J., Law, R.A, Tuntithavornwat, S., Bieber, J.M., Zheng, L., Konstantopoulos, K. "Novel association between podocalyxin and dynamin2 promotes migration and invasion of pancreatic cancer cells *in vitro* and *in vivo* by altering microtubule and focal adhesion dynamics", Oral Presentation, Biomedical Engineering Society Annual Meeting, Phoenix, AZ, October 11-14, 2017
4. **Wong, B. S.**, Shea, D.J., Law, R.A., Konstantopoulos, K. "Podocalyxin Promotes Migration of Pancreatic Cancer Cells by Altering Cytoskeletal Dynamics", Invited Oral Presentation, JHU INBT

Graduate Mini Symposium, Baltimore, MD, March 10, 2017

5. **Wong, B. S.**, Shea, D.J., Law, R.A., Konstantopoulos, K. "Podocalyxin Promotes Migration of Pancreatic Cancer Cells by Altering Cytoskeletal Dynamics", Oral Presentation, Biomedical Engineering Society Annual Meeting, Minneapolis, MN, October 5-8, 2016
6. **Wong, B. S.**, Shea, D.J., Law, R.A., Konstantopoulos, K. "Podocalyxin Knockdown Impairs Migration of Pancreatic Cancer Cells By Influencing Cytoskeletal Remodeling And Surface Adhesion", Oral Presentation, American Institute of Chemical Engineers Conference, San Francisco, CA, November 12-19, 2016
7. **Wong, B. S.,** Shea, D.J., Law, R.A., Dallas, M.R., Konstantopoulos, K. "Podocalyxin promotes migration of pancreatic cancer cells by altering cytoskeletal dynamics", Poster Presentation, 10th JHU Nano-Bio Symposium: Precision Medicine, Baltimore, MD, April 29, 2016
8. Stroka, K.M., Shriver, M., **Wong, B. S.**, Konstantopoulos, K., Kontrogianni-Konstantopoulos, A. "Loss of Giant obscurins Alters Breast Epithelial Cell Mechanobiology", Oral Presentation, Biomedical Engineering Society Annual Meeting, San Antonio, TX, October 22-25, 2014
9. **Wong, B. S.**, Yoong, S. L., Chin, C. F., Ang, W. H., Pastorin, G. "Delivery Of Platinum-Based Pro-Drugs Into Cancer Cells & Evaluation Of The Mitochondrial Targeting & The Resulting Drug Efficacy**"**, Poster Presentation, *Annual Pharmacy Research Awareness Symposium 2013* (2nd prize winner for best poster in the Pharmaceutical Technology category), Singapore, 2013
10. **Wong, B. S.**, Teoh, S., Kang, L. "Porous Polycaprolactone Scaffold As Targeted Drug Delivery System & Cell Attachment Platform", Poster Presentation, *17th National Undergraduate Research Opportunities Programme Congress 2012*, Singapore, 2012

## PATENTS

1. Konstantopoulos, K., Paul, C.D., Quiñones-Hinojosa, A., Shah, R.S., Ruiz-Valls, A,. Martinez-Gutierrez, J.C., Yankaskas, C.L., **Wong, B.S.,** "Predicting brain tumor patient prognosis", (2016) Patent Cooperation Treaty, PCT/US2016/064725

## TECHNICAL SKILLS

- **Cell Biology**: *Bacterial and mammalian cell culture, transient and stable transfection, lentivirus production and transduction, cell line generation, cell sorting, cell viability assays*
- **Molecular Biology**: *Molecular cloning, plasmid generation, western blotting, QPCR, zymography*
- **Biochemistry**: *ELISA, immunoprecipitation, in vitro pulldown assays, recombinant protein purification, mass spectrometry*
- **Microscopy**: *Time lapse live cell imaging, epifluorescence and confocal microscopy, total internal reflectance fluorescence microscopy, immunofluorescence staining and imaging, FRAP, FRET*
- **Analytical Techniques**: *Flow cytometry, HPLC, spectrophotometry, bioluminesecence*
- **Microfabrication**: *Microfluidic device design, photolithography, replica molding, microcontact printing, polyacrylamide hydrogel preparation*
- **Nanomaterials:** carbon nanotube surface functionalization, Kaiser test, TEM, SEM
- **Animal Work**: *Subcutaneous injection, orthotopic implantation into pancreas, hemispleen hepatic metastasis model, microsurgery, autopsy, immunohistochemistry, skin permeation assays*
- **Technical Software**: *PRISM, ImageJ, MatLAB, Nikon NIS elements, Zeiss ZEN, AutoCAD, SPSS*
- **Languages:** *English, Chinese Mandarin, Chinese Cantonese, Malay*

## WORK EXPERIENCE

**Hospital Pharmacy Preceptorship,** Parkway Hospital, Singapore, (Jun 2012-Aug 2012)

- Dispensed & counseled patients on appropriate drug use in a hospital setting
- Assisted in setting up the new Mouth Elizabeth (Novena) Hospital Pharmacy & consolidated the drug-allergy alert database

**Retail Pharmacy Preceptorship,** Guardian Health & Beauty, Singapore, (Jun 2011-Aug 2011)

- Recommended & counseled patients on use of over-the-counter medications
- Engaged in the operations & management of retail pharmacy, such as stocktaking & shelving merchandizes

## TEACHING & MENTORING EXPERIENCES

**Research Mentor**, Konstantopoulos Lab, JHU (2014-2019)

- Train junior graduate (4), undergraduate (4) and high school (1) students in project design, experimental techniques, data analysis and scientific presentations
- 2 of the undergraduate mentees had started prestigious Chemical or Biomedical Engineering Ph.D. programs at University of California, Berkeley and University of Southern California

**Teaching Assistant**, Transport Phenomena I, JHU (Spring 2015, Spring 2016)

- Conduct course lectures, led weekly homework recitation sessions, designed homework and exam questions, grade midterms and exams

## LEADERSHIP & COMMUNITY EXPERIENCES

**Finance Manager,** Konstantopoulos Lab, JHU (2014-2019)

- In charged of placing orders for common lab supplies
- Consolidated and performed detailed accounting for lab spending on a monthly basis
- Worked closely to coordinate with departmental administrative staff to resolve occasionally issues with purchasing and spending chargers discrepancy

**Chair**, Institute for NanoBioTechnology Mini Spring Symposium, JHU (2015)

- Coordinated and developed program of graduate student, postdoctoral fellow, and professor research presentations
- Served as master of ceremony for the symposium and facilitate question and answer session between the attendees and the presenters

**Member**, of the following professional societies (2015-Present)

- American Institute of Chemical Engineers
- Biomedical Engineering Society

**Volunteer,** STEM science outreach program, JHU (2014)

- Designed, prepared and led hands-on science demonstrations and lessons for middle school students at the Roosevelt Recreation Center in Baltimore

**Member,** Graduate Student Liaison Committee, JHU (2013-2019)

- Attended committee board meetings to serve as graduate student liaison with faculty of the Chemical and Biomolecular engineering department
- Assisted annually for the departmental recruitment events for prospective Ph.D. students as student shuttler and poster presenters
- Volunteer actively and regularly for community clean up events

**Disaster Management Officer,** Red Cross Youth Chapter, NUS (2010-2012)

- Organized standard first aid courses for new recruits to impart first aid knowledge to members
- Co-ordinated first aid duties for major school events, such as marathon, inter-faculty games & career fair, to ensure participants safety

**Paramedic,** Singapore Medical Care Training and Services (2011-2012)

- Attended rigorous and intensive professional paramedic training on a weekly basis
- Standing by and cover for numerous sporting and community events as part of a group of certified paramedics